QCD studies with processes involving a J/ψ decaying into muons

Raúl Iraq Rabadán Trejo

Supervisor: Dr. H. Castilla Valdez
Dr. I. Heredia de la Cruz

Departamento de Física
CINVESTAV

This dissertation is submitted for the degree of
Doctor in Science

CINVESTAV October 2018

Abstract

This thesis reports on the measurement of the Λ_b polarization and the parity-violating asymmetry parameter in the decay channel $\Lambda_b \to J/\psi\Lambda$ from pp collisions at $\sqrt{s}$ = 7 and 8 TeV, and on the exclusive J/ψ photo-production in ultra peripheral proton-lead collisions at $\sqrt{s_{NN}} = 8.16$ TeV using data collected by the CMS experiment at the LHC. The Λ_b polarization is measured to be 0.00 ± 0.06 (stat) ± 0.06 (syst) and the parity-violating asymmetry parameter is determined to be 0.14 ± 0.14 (stat) ± 0.10 (syst); results are compared to predictions from perturbative QCD. The measured photo-production cross sections $\sigma(\gamma + p \to J/\psi + p)$ in the J/ψ rapidity intervals 2.0 < y < 2.4 and -2.4 < y < -2.0, and Bjorken-x ranges of 2×10^{-2} to 2×10^{-5}, are 62 ± 5 ± 2 nb, and 228 ± 18 ± 8 nb, respectively, the first uncertainty is statistical and the second due to luminosity determination; results are compared with measurements from ALICE and LHCb.

Table of contents

List of figures

List of tables

Introduction

Quantum chromodynamics (QCD) is the component of the standard model of particle physics that describes the strong interaction of colored quarks and gluons. However, theoretical predictive calculations can only be successfully performed in specific situations. Predictive methods include lattice QCD and perturbative QCD. Processes at hadron colliders, in particular at LHC, allow to test QCD predictions which at the same time improves our understanding of the strong interactions.

The first main topic of this thesis is the measurement of the Λ_b polarization, parity violating asymmetry parameter and $\Lambda_b \to J/\psi\Lambda$ decay amplitudes. These measurements provide tests of theoretical models based on perturbative QCD. The polarizations expected from all QCD subprocesses $qq' \to qq'$, $qg \to qg$, $gg \to q\overline{q}$, $qg \to qg$ and $q\overline{q} \to q'\overline{q}'$ depends on the quark mass at a given momentum an the heaviest quark acquires the largest polarization [1]. It is expected that after hadronization, the Λ_b inherits a fraction of the b-quark polarization. Predictions of the transverse polarization in Λ_b decays are 0.10 [2] and 0.20 [3].

The second core topic of the thesis concerns to the measurement of the exclusive J/ψ photoproduction off protons in ultra-peripheral pPb collisions. The main physical motivation to study this process is that according to leading order QCD calculations, this process allows a detailed study of the gluon distribution in the proton given that its cross section is expected to scale as the square of the gluon probability density function. It also provides a powerful tool to search for gluon saturation [4, 5], which is the most straightforward mechanism to slow down the growth of the PDF for gluons carrying a small fraction of the momentum of hadrons (Bjorken-x). A feasible approach to the study of photoproduction processes at the LHC is by means of ultra-peripheral collisions (UPCs), in which two accelerated hadrons (proton, Ion) surrounded by a cloud of quasi-real photons, interact with an impact parameter larger than the sum of their radii, excluding in this way purely hadronic interactions. The rate of processes involving the interaction with these photons is maximized in heavy-ion collisions, where the photon flux is proportional to the square of the electric charge of the accelerated particle, gaining thus a factor Z^2 with respect collisions among protons.

The content of the thesis is organized as follows. In Chapter 1 an overview of the Large Hadron Collider is given. Chapter 2 contains an overview of the CMS detector and its subsystems. In chapter 3 a desciption of the CMS Resistive Plate Chambers (RPC) subdetector is given followed by a report on the ongoing longevity studies of the present RPCs for their operation at the High Luminosity LHC and preliminary results are reported. Chapter 4 introduces the physical motivations of the measurements reported in this thesis. Chapter 5 describes the analysis of the of the Λ_b polarization, and $\Lambda_b \to J/\psi\Lambda$ angular parameters measurements. Chapter 6 presents the analysis of the exclusive J/ψ photoproduction in pPb ultra peripheral collisions at $\sqrt{s_{NN}} = 8.16$ TeV. Finally, some conclusions and remarks are given.

Chapter 1

The Large Hadron Collider

1.1 LHC overview

The Large Hadron Collider (LHC) [6] is the highest-energy particle accelerator ever built. It is a proton-proton collider with design center-of-mass energy of 14 TeV and nominal luminosity of $\mathscr{L} = 10^{34} cm^{-2} s^{-1}$. It can also collide heavy ions ($^{208}Pb^{82+}$), with beam energies of 2.76 TeV/nucleon and nominal luminosity of $\mathscr{L} = 10^{27} cm^{-2} s^{-1}$. Table 2.1 shows the LHC design parameters for proton and lead beams.

An schematic view of the LHC is shown in Fig. 1.1, the ring is divided in eight arcs (octant's). At four of them the physics experiments are built. One houses the acceleration system, one the beam dump, and the beam cleaning systems are installed at the remaining two. The curved sections are occupied by magnets and the systems to make them functional.

The number of events generated in a collider via a given process is given by:

$$N = \mathscr{L}\sigma, \tag{1.1}$$

where $\mathscr{L}$ is the machine luminosity, which depends only on the beam parameters, and σ is the cross section for the process being studied. Greater luminosity gives more possibility of an interesting process to occur. For a circular collider, the luminosity is given by:

$$\mathscr{L} = \frac{N_1 N_2 n_b f_{rev} \gamma}{4\pi \varepsilon_n \beta^*}. \tag{1.2}$$

In this formula N_1 and $N_2$are the numbers of particles per bunch in each beam (particles inside the beam are accelerated into small groups, called bunches), n_b is the number of bunches per beam, frev is the revolution frequency, n is the normalized beam emittance (a

Parameters	p-p collisions 2	Pb-Pb collision
Center-of-mass energy (TeV)	14	1148
Number of particles per bunch	$1.1x10^11$	$\sim 8x10^7$
Number of bunches	2808	608
Design Luminosity $(cm^{-2}s^{-1})$	10^{34}	$2x10^{27}$
Bunch length (mm)	53	75
Beam radius at interaction point (μm)	15	15
Time between collisions (ns)	25	$124.75x10^3$
Bunch crossing rate (MHz)	40.08	0.008
Circumference (km)	~ 27	~ 27
Dipole field (T)	8.3	8.3

Table 1.1 Parameters of the Large Hadron Collider for p-p and Pb-Pb collisions [46].

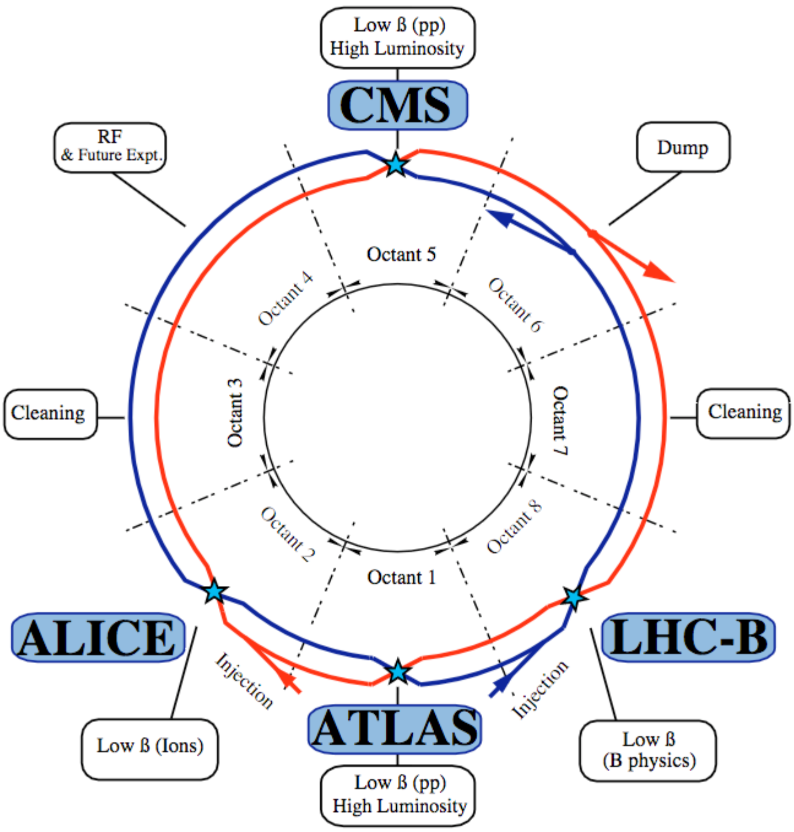

Fig. 1.1 Layout and experiments in the LHC. The LHC machine accelerates protons in two separated beams and opposite directions as shown in the blue and red lines. The ring is divided in eight sections, with pits at the middle of the octants. The two large experiments CMS and ATLAS are diametrically opposite in pits 5 and 1, respectively.

measure of how much the particles depart from the ideal trajectory), γ is the relativistic gamma factor for the particles in the beam, β^* is the beta function at the collision point (it gives the envelope for the motion of particles) and F is the luminosity reduction factor due to the crossing angle at the interaction point. In this equation, only f_{rev} and γ are determined by collider radius and particle energy, while all the other parameters may be controlled to maximize the luminosity.

1.2 CERN Accelerator Complex

The Large Hadron Collider relies on a chain of accelerators in order to reach the designed center-of-mass energy for the particles. Each machine in this chain brings the beam to a higher energy and then injects it into the next one. The LHC is the last element in the chain, where accelerating of the beam energy can go up to 7 Tev. A schematic view of the CERN accelerator complex is shown in Fig. 1.2. It all starts with a bottle of hydrogen gas. The hydrogen atoms are stripped of their electrons and the protons left after this process are accelerated by a linear accelerator, LINAC2, up to energies of 50 MeV. Next step is the Proton Synchrotron Booster (PSB) which accelerates this proton beam up to 1.4 GeV. After being accelerated in the following Proton Synchrotron (PS) the protons reach 25 GeV. The final acceleration step before injection into the LHC is provided by the Super Proton Synchrotron (SPS), where particles reach energies of 450 GeV. The LHC then starts accelerating the beams in two separate beam pipes for each direction until they reach maximum energy of 7 TeV. Then collisions start at the different experiments with center-of-mass energies of up to $\sqrt{s} = 14$ TeV. Accelerating lead ions start from a source of vaporized lead and enter LINAC3. After this they are transferred to Low Energy Ion Ring (LEIR) and then they follow the same route to maximum acceleration as protons.

1.3 LHC Experiments

Four experimental interaction regions of the LHC are built four particle detectors, Fig. 1.1. The CMS [7] and the ATLAS [8] experiments are general purpose detectors, i.e. they aim at detailed studies of the known physics and searches for new physics. ALICE [9] experiment was designed to study Heavy Ion collisions aiming to improve the understanding of the quark-gluon plasma (QGP). The LHCb [10] experiment studies bottom-quark physics and CP violation.

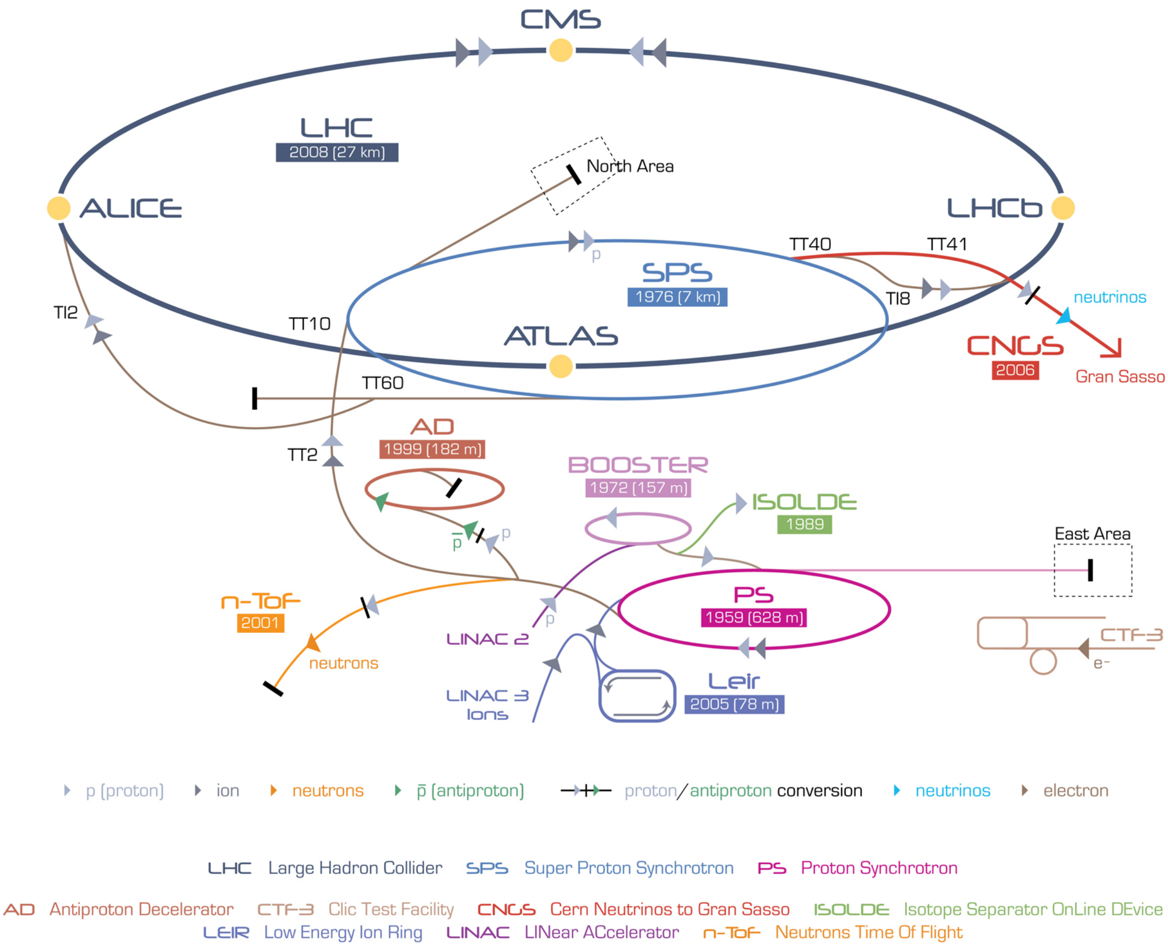

Fig. 1.2 The LHC accelerator complex at CERN.

Chapter 2

The CMS Experiment

The overall concept and the design of the detector can be found in Refs. [11, 12]. The detector is loacted at about 100 m underground at the LHC IP5. CMS is a multi-purpose apparatus used to study a wide range of phenomena produced in high-energy collision. In order to cover the requirements of the LHC physics program [13], CMS is made of different sub-detectors. It is a compact 28.7 m long cylinder with an overall diameter of 15 m and total weight of about 14 500 tones.

A layout of the detector is shown in Fig. 2.1 The inner-most subsystem is the silicon tracking detector (2.2) placed right next to the beam pipe. Calorimeters are the next subsystems, an electromagnetic one (2.3) and a hadronic one (in section 2.4). The solenoid comes after the calorimeters and the outer-most subsystem is the muon detector (2.5). The different CMS subsystems are organized in three regions, a barrel region and two endcap regions. The Barrel consists of cylindrical layers around the beam pipe, while the endcaps consist of disk layers placed on either side of the barrels. The cylindrical shape of the detector is dictated by its main feature,a super-conducting solenoid magnet (section 2.1) with a length of 12.9 m and an inner diameter of 6 m. The solenoid is installed in the barrel region and produces a magnetic field of 3.8 T. The muon system, which is placed outside the solenoid, should have a very high performance with good muon identification and momentum resolution over a wide range of momenta and angles. The tracker detector ensures good charged particle momentum resolution and reconstruction efficiency. The electromagnetic calorimeter gives good energy resolution for electrons and photons and the hadron calorimeter measures the energy of charged and neutral hadrons.

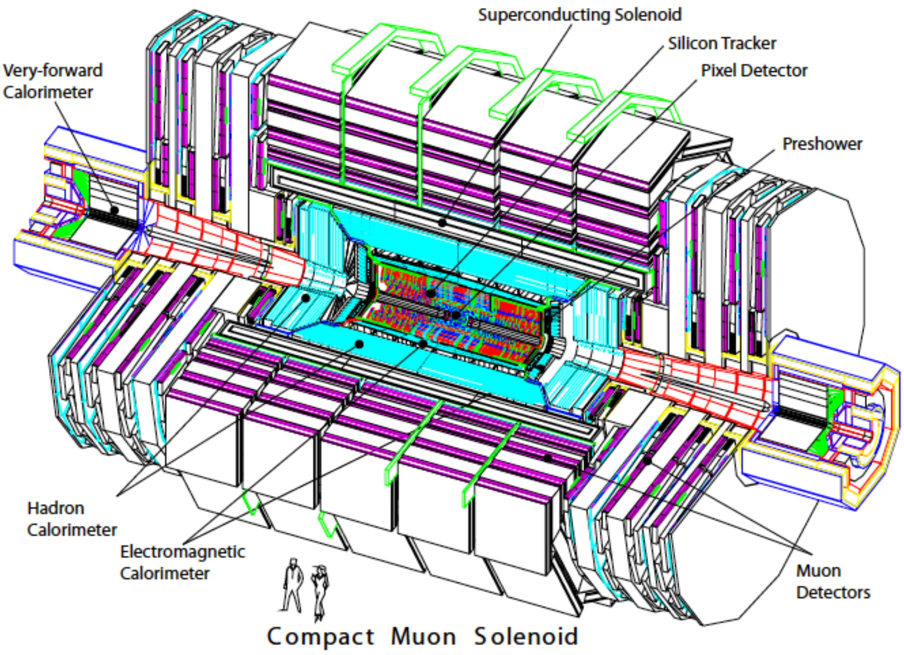

Fig. 2.1 Schematic layout of the CMS experiment

2.1 CMS Solenoid

The superconducting solenoid of the CMS experiment [14] is used to bend the charged particles crossing the detector providing a precise measurement of their transverse momentum . The CMS magnet is 12.9 m long with inner diameter of 6 m and produces a magnetic field of 3.8 T. This makes it the largest superconducting magnet ever built. It is made of a stabilized reinforced NbTi superconducting wire coils that produce a uniform magnetic field when electricity flows through them and is cooled down to -268.5 °C, which is just a degree warmer than outer space.

The CMS solenoid is enclosed with a 12 500 tones steel return yoke in which the muon detectors are placed. The inner coil radius is big enough so that the inner tracker and the calorimeters can fit inside. In Fig. 2.2a schematic view of the CMS solenoid is shown as well as the steel return yoke and muon chambers around the magnet.

2.2 Tracker system

The CMS tracker [15] occupies a cylindrical volume 5.8 m in length and 2.5 m in diameter, with its axis closely aligned to the LHC beam line. The tracker is immersed in a co-axial magnetic field of 3.8 T provided by the CMS solenoid. A schematic drawing of the CMS

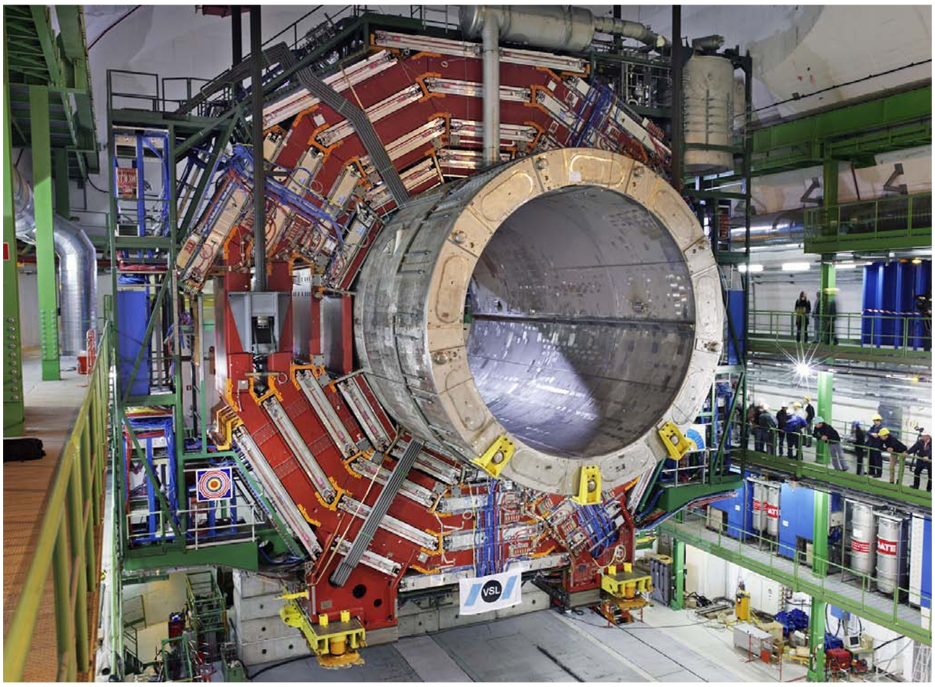

Fig. 2.2 A schematic representation of the CMS solenoid.

tracker is shown in Fig. 2.3 The tracker comprises a large silicon strip tracker with a small silicon pixel tracker inside it. In the central pseudorapidity region, the pixel tracker consists of three co-axial barrel layers at radii between 4.4 cm and 10.2 cm and the strip tracker consists of ten co-axial barrel layers extending outwards to a radius of 110 cm. Both subdetectors are completed by endcaps on either side of the barrel, each consisting of two disks in the pixel tracker, and three small plus nine large disks in the strip tracker. The endcaps extend the acceptance of the tracker up to a pseudorapidity of $\eta < 2.5$. The pixel detector consists of cylindrical barrel layers at radii of 4.4, 7.3 and 10.2 cm, and two pairs of endcap disks at z = $\pm$34.5 and $\pm$46.5 cm. It provides three-dimensional (3-D) position measurements of the hits arising from the interaction of charged particles with its sensors. The hit position resolution is approximately 10 μ m in the transverse coordinate and 20–40 μ m in he longitudinal coordinate, while the third coordinate is given by the sensor plane position. In total, its 1440 modules cover an area of about 1 m^2 and have 66 million pixels. The strip tracker has 15 148 silicon modules, which in total cover an active area of about 198 m^2 and have 9.3 million strips. It is composed of four subsystems. The Tracker Inner Barrel (TIB) and Disks (TID) cover r < 55 cm and |z| < 118 cm, and are composed of four barrel layers, supplemented by three disks at each end. These provide position measurements in rϕ with a resolution of approximately 13–38 μ m. The Tracker Outer Barrel (TOB) covers r > 55 cm and $|z| < 118$ cm and consists of six barrel layers providing position measurements in rϕ with a resolution of approximately 18–47 μ m. The Tracker EndCaps (TEC) cover the region 124 < |z| < 282 cm. Each TEC is composed of nine disks, each containing up to seven concentric rings of silicon strip modules, yielding a range of resolutions similar to that of the TOB.

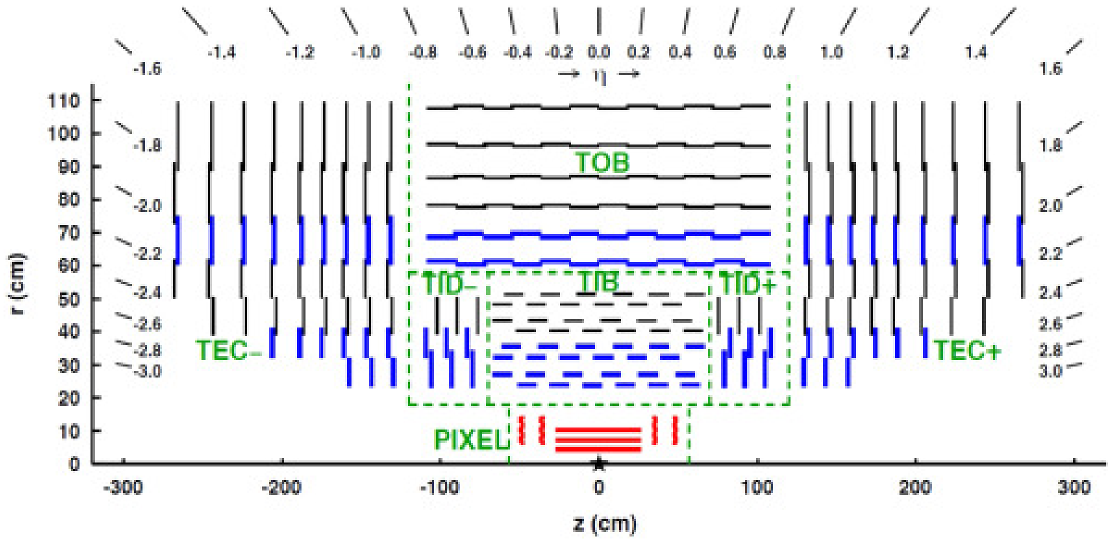

Fig. 2.3 A schematic representation of the CMS tracker.

2.3 Electromagnetic Calorimeter

The CMS ECAL [16] is a compact, hermetic, fine-grain, homogeneous calorimeter made of 75848 lead tungstate (PbWO4) scintillating crystals. The choice of PbWO4 (density = 8.28g/cm3) was primarily motivated by its radiation tolerance, its small radiation length (X0 = 0.89cm) and Moliere radius (rM = 2.19 cm), and its fast response (99%) of the light is collected in 100 ns, which is compatible with the 40MHz interaction rate of the LHC). The crystals are arranged in a quasiprojective geometry and distributed in a central barrel section (EB) covering the pseudorapidity range $|\eta| < 1.48$, and two endcaps (EE) extending the coverage up to $|\eta| = 3.0$, as shown in Fig. 2.4. The barrel crystals are 23 cm long (26 X_0) and have a front-face cross section of 2.2×2.2 cm ^{2}, while the endcap crystals are 22 cm long (25 X_0), with a front-face cross section of 2.86×2.86 cm ^{2}. The crystal transverse size is comparable to the typical shower size in $PbWO_4$, which facilitates photon identification based on shower shape criteria.

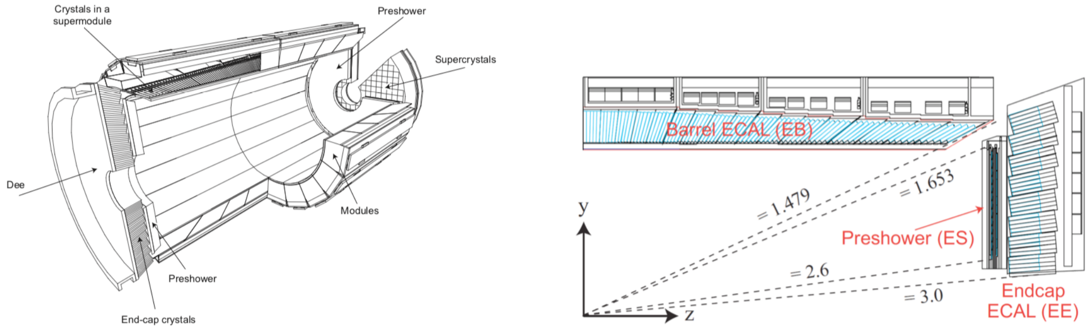

Fig. 2.4 Schematic view of the CMS ECAL structure.

2.4 Hadron Calorimeter

The HCAL barrel (HB) covers the region $\eta < 1.3$ and consists of 36 azimuthal wedges assembled into two half-barrels (HB+ and HB-). The Hadronic endcap calorimeter (HE) covers the pseudo rapidity range $1.3 < |\eta| < 3$. The hadronic forward calorimeter (HF) extends the coverage $3.0 < |\eta| < 5.0$. Additional scintillators (HO) are located outside of the solenoid and act as "tail catchers" effectively increasing the thickness of the calorimeter in the central pseudo rapidity region.

The HB is a sampling calorimeter consisting of alternating plates of brass absorber and scintillator tiles embedded with wavelength shifting (WLS) fibers. The WLS fibers are spliced to clear fibers which direct the light to an optical decoder unit (ODU). The ODU arranges the fibers into readout towers covering an area of 0.087×0.087 in η-ϕ and direct the light from each tower to separate channels of a hybrid photo diode (HPD) which can operate in a high magnetic field. Each HPD has 18 channels of readout.

The HF subdetector is a Cerenkov light detector made up of quartz fibers embedded within a 165-cm-long steel absorber. There are two types of fibers within the HF: long fibers which span the length of HF, and short fibers which begin 22 cm into the detector. Differences between signals read out from the long and short fibers can be used to distinguish between electrons or photons and hadrons. Photomultiplier tubes (PMTs) connected to the fibers via light guides convert detected light to electrical signals. Energy is reconstructed from the digitized charge measurements. In HB, HE, and HO 4 time samples are summed together. The signal in HF is very fast and has a width of about 10ns which is mostly contained within one 25ns time sample. Individual channels are combined into a projective tower structure which combines information from ECAL and HCAL. In order to save disk space, the raw digitized data is dropped from the event record and most physics objects which use calorimeter information are then derived from the CaloTower objects.

2.5 Muon System

The muon system [17] is located outside the solenoid and covers the range $|\eta| < 2.4$. It is composed of gaseous detectors sandwiched among the layers of the steel flux-return yoke that allow a traversing muon to be detected at multiple points along the track path.

Three types of gas ionization chambers were chosen to build the CMS muon system: drift tube chambers (DTs), cathode strip chambers (CSCs), and resistive plate chambers (RPCs). The DTs are segmented into drift cells; the position of the muon is determined by measuring the drift time to an anode wire of a cell with a shaped electric field. The CSCs operate as standard multi-wire proportional counters but add a finely segmented cathode strip readout, which yields an accurate measurement of the position of the bending plane $R-\phi$ coordinate at which the muon crosses the gas volume. The RPCs are double-gap chambers operated in avalanche mode and are primarily designed to provide timing information for the muon trigger. The DT and CSC chambers are located in the regions $|\eta| < 1.2$ and $0.9 < |\eta| < 2.4$, respectively, and are complemented by RPCs in the range $|\eta| < 1.9$. We distinguish three regions, naturally defined by the cylindrical geometry of CMS. Thes three regions are respectively referred to as the barrel ($|\eta| < 0.9$), overlap ($0.9 < |\eta| < 1.2$), and endcap ($1.2 < |\eta| < 2.4$) regions. The chambers are arranged to maximize the coverage and to provide some overlap where possible. In the barrel, a station is a ring of chambers assembled between two layers of the steel flux-return yoke at approximately the same value of radius R. There are four DT and four RPC stations in the barrel, labeled MB1–MB4 and RB1–RB4, respectively. Each DT chamber consists of three "superlayers", each comprising four staggered layers of parallel drift cells. The wires in each layer are oriented so that two of the superlayers measure the muon position in the bending plane $R-\phi$ and one superlayer measures the position in the longitudinal plane (R-θ). The chambers in MB4 have only the two $R-\phi$ superlayers, though. The two innermost RPC barrel stations, RB1 and RB2, are instrumented with two layers of RPCs each, facing the innermost and outermost sides of the DT. For stations 3 and 4 the RPCs have only one detection layer. The RPC readout strips are oriented parallel to the wires of the DT chambers that measure the coordinate in the bending plane. From the readout point of view, every RPC is subdivided into two or three η partitions called "rolls". Both DT and RPC barrel stations are arranged in five "wheels" along the z dimension, with 12 ϕ-sectors per wheel. In the endcap geometry, a station is a ring of chambers assembled between two disks of the steel flux- return yoke at approximately the same value of z. There are four CSC and four RPC stations in each endcap, labeled as ME1–ME4 and RE1–RE4, respectively. Between Run 1 and Run 2, additional chambers were added in ME4 and RE4 to increase redundancy, improve efficiency, and reduce misidentification rates. Each CSC chamber consists of six staggered layers, each of which measures the muon position in two coordinates. The cathode strips are oriented radially to measure the muon position in the bending plane $R - \phi$, whereas the anode wires provide a coarse measurement in R. The RPC strips are oriented parallel to the CSC strips to measure the coordinate in the bending plane, and each endcap chamber is divided into three $|\eta|$ partitions (rolls) identified by the letters A, B, and C. In the radial direction, stations are arranged in two or three "rings" of endcap RPCs and CSCs. In the inner rings of stations 2, 3, and 4, each CSC chamber subtends a ϕ angle of 20º; all other CSCs subtend an angle of 10º.

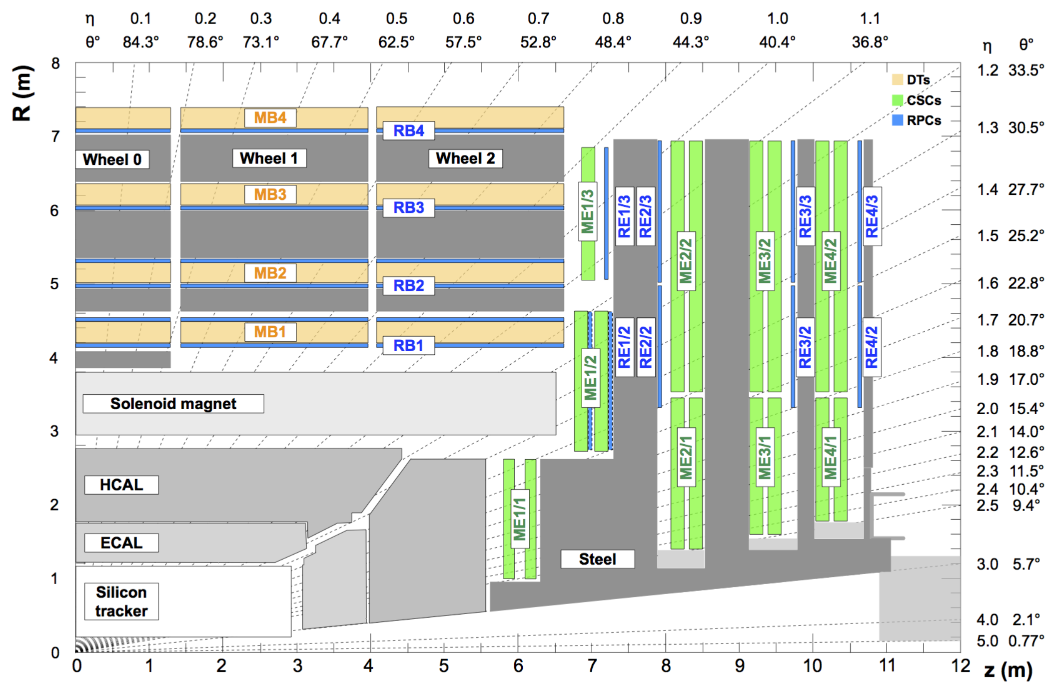

Fig. 2.5 R-z cross section of a quadrant of the CMS muon system, showing DT (yellow), CSC (green) and RPC chambers (light blue). The interaction point is at the lower left coner

2.6 Trigger and data acquisition systems

The CMS trigger system [18, 19] is comprised of an L1 hardware trigger and an HLT array of commercially available computers running high-level physics algorithms, an schematic view of the trigger data flow is shown in Fig 2.6. L1 trigger reduces the event rate from 40

MHz to less than 100 kHz. The second step HLT trigger is giving the final output data rate of about 100 Hz.

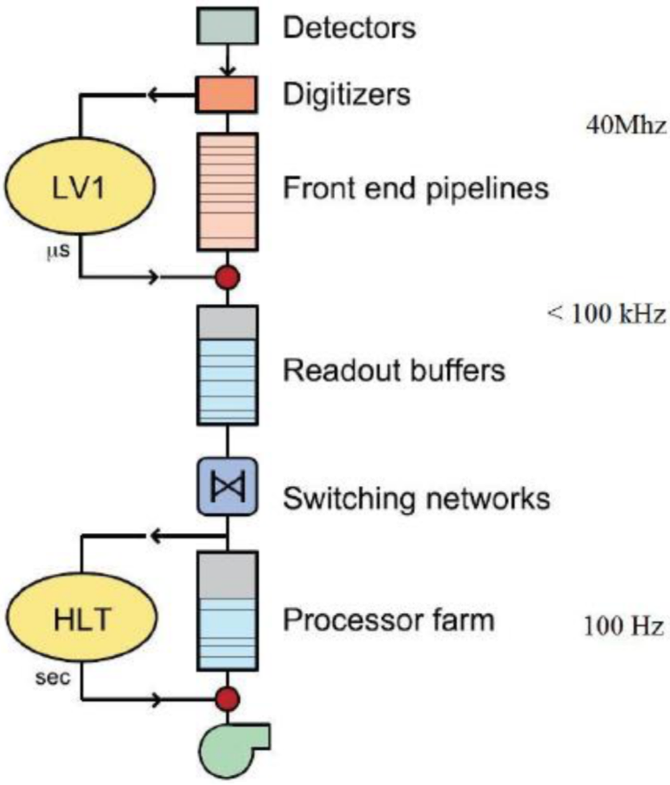

Fig. 2.6 CMS trigger schema.

The Level 1 trigger [20] selects events with interesting signatures based only on the raw the information from the calorimeters and the muon systems. The three major subsystems implemented in the L1 Trigger System are the Calorimeter Trigger, the Muon Trigger and the Global Trigger. The Calorimeter Trigger [18] preserves the local energy sums from the ECAL, HCAL and HF individual readout towers, i.e. the Trigger Primitive Generator (TPG) circuits. These sums are accompanied by a fine-grain bit for the ECAL, which indicates the transverse extent of the electromagnetic energy deposit, i.e. if a large fraction of the summed energy comes from 2 out of 5 adjacent (η) strips. The TPG information is then transferred to the Regional Calorimeter Trigger (RCT), which identifies electrons, γ_s, τ_s and hadron jets candidates. Finally these trigger primitives along with sums of transverse energy are sent to the Global Calorimeter Trigger (GCT), where the best four candidates from each category go to the Global Trigger. The Muon Trigger uses information from DT, CSC and RPC local triggers to drop events with low quality muons. The trigger information from the different muon chambers comes in different scales. The Global Muon Trigger (GMT) major task is to combine and convert the information from all three systems into the same η, ϕ and p_T scale in order to correlate the muon tracks. Finally GMT estimates only the 4 best muon objects and sends them to the L1 Global Trigger [21]. The L1 Global Trigger based on programmed logical combinations holds a time match on the information from both GCT and GMT and decides to accept or reject these events.

The second stage of the Trigger system is the High Level Trigger (HLT) [22]. All events passing the L1 trigger are transferred to a computer farm where the software based offline trigger filters further the events rate by using different reconstruction algorithms. Only events that pass at least one of the HLT criteria are kept for permanent storage and thus the event rate is reduced from 100 kHz to 100 Hz, which is the accepted rate to be stored on tape. The HLT algorithms execute complex physics selection on a farm of commercial processors in order to accept only the events with most interesting physics content. Each processor has access to the full raw L1 data and analyzes one event with a total processing time of $\sim$1 s/event. The minimal processing time is guaranteed by three basic reconstruction concepts of the HLT software. Trigger objects are reconstructed only if they are needed in the trigger decision. Fast algorithms help avoiding unnecessary calculations by rejecting events as early as possible by using several stages of virtual trigger levels for selection and reconstruction. There is no limitation on the number of employed algorithms or the number of virtual levels, the only exception being the CPU time. It is accepted that Level 2 Trigger is used for a first HLT stage based on data from the calorimeters and muon systems, while the algorithms using the tracker data are referred to as Level 3 Trigger. The HLT algorithms are used to process only parts of detector information, which contains trigger objects found in the preceding trigger levels. Reconstruction is aborted in case the result cannot be altered by any further calculations. The information coming out of the HLT constitutes primary data sets, where event have different HLT paths according to the kind of physics they may content. This information is originally stored in CERN Tier0 of the Worldwide LHC Computing Grid (WLCG) network [23] and later is distributed around the entire network for an easy access for the CMS collaboration.

The Data Acquisition (DAQ) System read the output of the L1 trigger and merges in a complete event all the event fragments from different front-end devices. After this it passes events to the Event Filter Farm where the HLT algorithms are run. The general architecture of the DAQ system is shown in figure 3.16. The Detector Front-End modules are used for storing digitized data from the front-end electronics until a L1 trigger accept signal is received. Data is held in pipelined memories. Then, based on the L1 trigger decision, data is transferred to front- end Readout Units (RU). The data flow in the RU builders is coordinated by the Event Manager. It also keeps track of the RUs memory occupancy. The readout builder network is capable of supplying 800 GB/s data flow to the filter systems. It is used to send event fragments to the builder units, where each event is defragmented before being transferred to the HLT for further processing.

2.7 CMS event data model and software overview

The overall collection of software, referred to as CMSSW [12], is built around a Framework, Event Data Model (EDM), and Services needed by simulation, calibration and alignment of the detector; reconstruction modules that process event and analysis data; and the support of a distributed computing infrastructure. The main goal of the Framework and EDM is to facilitate the development and deployment of reconstruction and analysis software. The CMS EDM is centered around the concept of an Event. An Event is a C++ object container for all raw and reconstructed data related to a particular collision. During processing, data are passed from one module to the next via the Event, and are accessed only through the Event.

The CMSSW event processing model consists of one executable, , and several plug-in modules which are managed by the Framework. All the code needed in the event processing (calibration, reconstruction algorithms, etc.) is contained in the modules (C++ classes). The same executable is used for both detector and Monte Carlo simulations.

Chapter 3

CMS Resistive Plate Chambers and their longevity studies

This chapter presents an overview of the CMS Resistive Plate Chambers (RPC) subsytem. The RPC working principle, design and configuration in the CMS experiment are also described. The chapter ends with a description and preliminary results of the present RPC longevity studies for their operation at the High Luminosity-LHC.

3.1 RPC operating principle

Resistive Plate Chambers (RPCs) are planar gaseous detectors, with combine very good time resolution of $\sim 1ns$ and good spatial resolution.

RPCs design is very simple. A gas detecting volume is enclosed by two resistive electrodes, the electrodes are generally made from Bakelite with a bulk resistivity of $10^{10} - 10^{12}$ Ωcm with conducting coating (usually graphite). Rectangular plastic frames are used for electrodes mounting, and small plastic separators (spacers) keep the constant distance between them to ensure electrical and mechanical stability. A schematic view of an RPC and its principle of operation are shown in Fig. 3.1.

RPCs operating principle is based on the gas ionization caused by a charged particle passing through the detector volume. The avalanche multiplication is caused by the cluster of electrons from ionization [24]. This leads to an electron charge developed inside the gap which drifts towards the anode. The signal of the detector is the charge induced on the pickup electrode. The HV power supply compensates the charge collected on the electrodes by moving the charges outside the gap. The effective ionization coefficient is defined as:

$$\eta = \alpha - \beta, \tag{3.1}$$

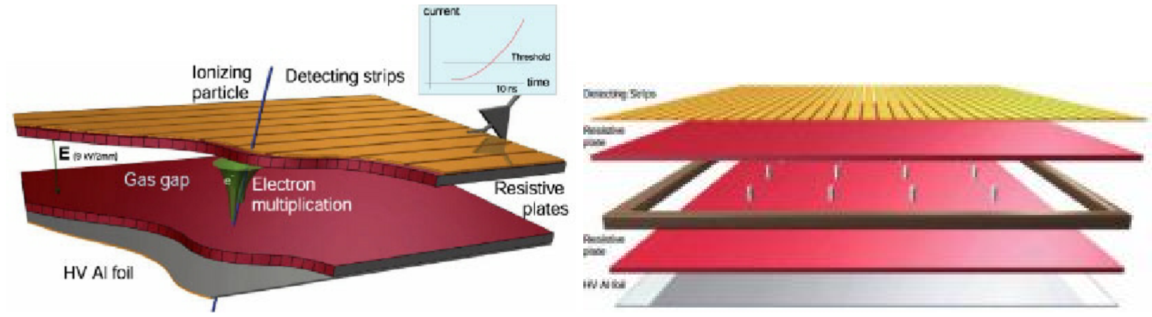

Fig. 3.1 Schematic view of a RPC chamber.

where α the Townsend coefficient describing the electron-ion pairs originally created, and β is the attachment coefficient describing the average number of electrons attached to form a negative ion [25]. For RPCs operating in avalanche mode, which is the operation mode at CMS, the average charge q_e of a single avalanche can be defined as [26]:

$$\langle q_e \rangle = \frac{k}{\eta d} \langle Q(d) \rangle = e n_0 \frac{k}{\eta d} \frac{\lambda}{\eta + \lambda} e^{\eta d} \tag{3.2}$$

where

$$k = (\varepsilon_r d/s)/(\varepsilon_r d/s + 2), \tag{3.3}$$

e the electron charge, n_0 the average size of the primary ionization cluster, λ the cluster density for the used gas mixture, ε_r the relative dielectric constant of the electrode, d the gap width, s the electrode thickness and Q_e the electron charge developed within a gap of width d.

3.2 RPC system at the CMS experiment

The CMS RPC system consists of 1056 double-gap chambers operating in avalanche mode [12]. Each RPC detector is made of two High Pressure Laminate (HPL) Bakelite gaps with 2 mm gas space between the plates. The HPL electrodes bulk resistivity is of the order of 1-6 $\times 10^{10}$ Ω·cm. The plates in each gap are separated by a $10 \times 10 cm^2$ plastic spacers to avoid contact due to the electrical attraction between them. The inside surface of the gaps is coated with a 35 to 45 μm linseed oil [27] to smooth the surface and quench the Ultraviolet (UV) photons [28]. The outer surfaces of the gaps are coated with conductive graphite paint, thus forming the High Voltage and ground electrodes. The two gaps are placed one on top of another with a common readout made of copper strips placed in between and isolated from the graphite by mylar sheets. Schematic view of the RPC double-gap design is shown in 3.2.

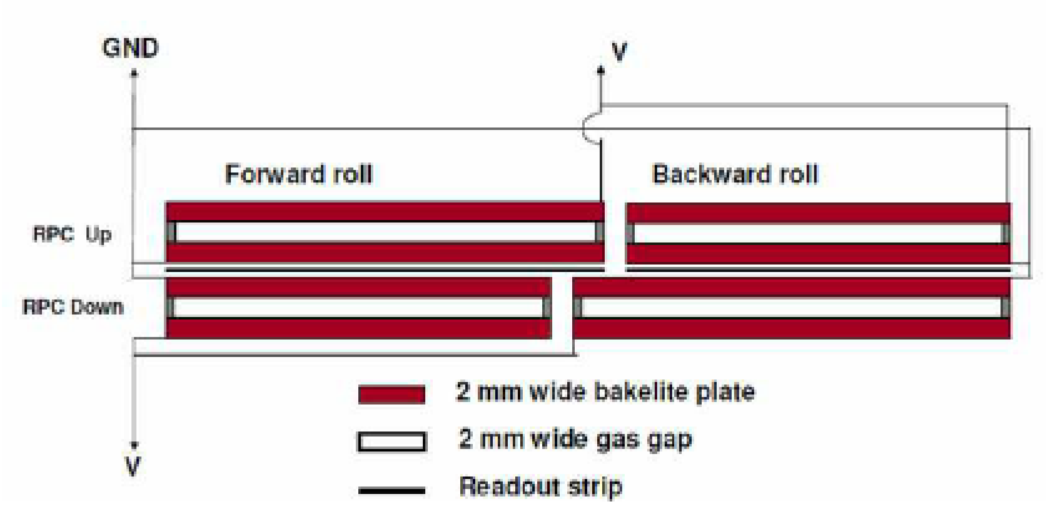

Fig. 3.2 Illustration of a double-gap CMS RPC barrel.

The standard RPC gas mixture consists of three components: $\mathbf{95.2\%}$ $\mathbf{C_2H_2F_4}$, acting as the charge carrier gas [29]; $\mathbf{4.5\%}$ $\mathbf{iC_4H_10}$, acting as a quencher gas to absorb UV photons from molecule de-excitation; $\mathbf{0.3\%}$ $\mathbf{SF_6}$, controlling the excess electrons through its high electron affinity [30].

The RPC system is divided in two regions, Barrel and Endcaps. The 1056 RPC chambers cover a pseudorapidity range of $|\eta| < 1.2$ in the Barrel and $0.9 < |\eta| < 1.9$ in the Endcap. There are more than 110 000 electronic channels and spans a sensitive area of $3500m^2$.

Barrel RPCs

The Barrel RPC system consists of 480 RPCs, arranged in 5 wheels along Z: Wheel 0, Wheel ±1, Wheel ±2. Each wheel consists of 4 stations (RB1, RB2, RB3 and RB4) with increasing radius R, which are interleaved with the steel return yoke. The inner-most stations, RB1 and RB2, are instrumented with layers of RPCs with a DT layer in between whereas the two outer stations consist of one layer of RPCs. Wheels are divided into 12 sectors (S01-S12) over the azimuthal angle. Due to mechanical reasons, RB3 and RB4 are further divided into + and – chamber along ϕ in all sectors but S04, S09 and S11 in RB4. RB4/S09 and RB4/S11 consist of only a single RPC chamber while RB4/S04 is divided in 4 chambers: ++, +, – and – –. A schematic view of the RPC Barrel geometry is shown in Fig. 3.3. The chambers are also divided in two pseudorapidity segments: forward and backward rolls. The RB2in

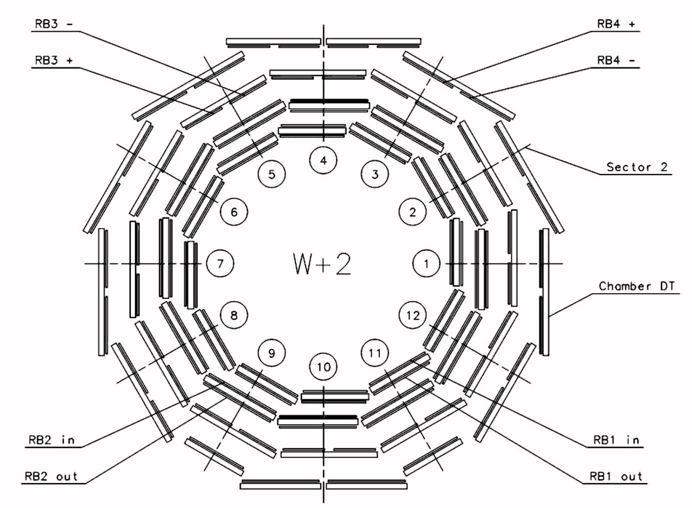

Fig. 3.3 Illustration of a RPC barrel wheel with the numbered sectors.

chambers in Wheels -1, 0, +1 and RB2out in Wheels -2, +2 are divided in 3 rolls: forward, middle and backward, as shown in figure Fig. 3.4.

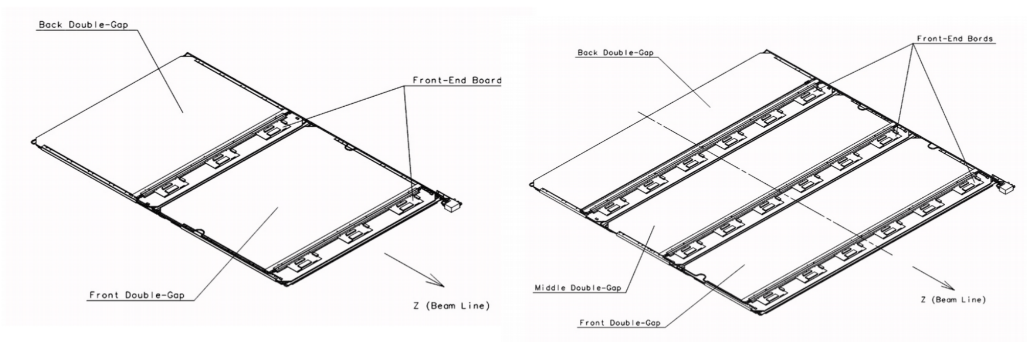

Fig. 3.4 Illustration of the RPC Barrel η partitions.

Endcap RPCs

The Endcap RPC system consists of 576 RPC chambers installed in 8 disks denoted as RE ±1, RE ±2, RE ±3 and RE $\pm4 - 4$ for both endcaps (positive and negative). Each disk is divided in 36 sectors along ϕ, and is made of two concentric rings, ring 2 (R2) and ring 3 (R3). There are 36 10° trapezoidal RPC chambers in each ring, which are further segmented in three rolls, labeled A, B and C with increasing η. Chamber are labeled from CH01 through CH36 within a ring. CH01 lays on the positive X-axis direction and the numbering goes anti-clockwise with respect to the interaction point. A schematic view of the RPC Endcap geometry is given in Fig. 3.5.

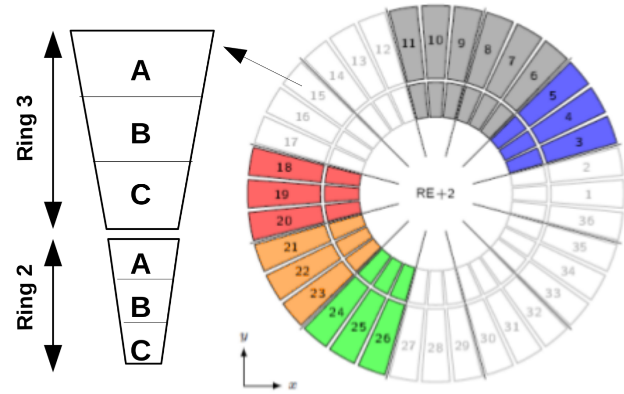

Fig. 3.5 Schematic layout of the RPC Endcap disks

3.3 CMS RPC Longevity studies

The existing RPC system has operated since 2009 and will now be expected to operate throughout the data-taking period of the HL-LHC [31, 32], in which it is intended to collect about 3000 fb^{-1} of pp collisions over 10 years of operation. However, these RPCs were originally built and validated for only ten years of LHC operation totaling 500 fb^{-1}. During the early years of LHC operation the RPC group performed a variety of measurements, which are reported in [33, 34], to estimate the aging effects during the LHC luminosity of 500 fb^{-1}.

Now that the expected luminosity and lifetime have increased it is essential to validate these RPC chambers for the new environment at the HL-LHC. Aging effects are complex, but typically the performance of the chambers is expected to deteriorate with the increase of the integrated charge deposited in the chambers, which is measured in millicoulomb/cm^2 ($mC\cdot cm^{-2}$). The severity of aging increases with the radiation exposure and is correlated to many factors, such as the electrode materials, operational gas gain, gas mixture, impurities in the gas itself, gas floaw rate, etc. Signatures of possible aging effects include a rise in spurious signal rates, increase in leakage currents, and a reduction in chamber efficiency. Because of the more difficult conditions at the HL-LHC it is important to experimentally verify the performance of the RPCs in those conditions, and to estimate the performance of the RPC system during the period of HL-LHC operations.

For these reasons the RPC group has begun a series of dedicated tests at the Gamma Irradiation Facility (GIF++) [35] at CERN using 4 existing RPC chambers; two of them will be irradiated with the goal of reaching the maximum amount of integrated charge expected during HL-LHC running (about 840 mC·cm^{-2}), whereas the remaining two will be used as a reference and will not be irradiated. During this accelerated aging tests the efficiency and cluster sizes of the chambers will be measured as a function of the background irradiation rate and the integrated charge. Furthermore, hit rates, operating high voltage, and current are measured at different integrated charges and compared to the reference values from the non irradiated chambers. Although the role that the gas system and the gas mixture play is important in aging studies, this issue is not addressed in this paper. We understand that studies in relation to the gas system and mixture are important concerns which are being studied by the RPC community. An early estimate of the longevity is presented

3.3.1 Background in the muon system

Background radiation in the CMS muon system is an important factor in the performance and longevity of the detectors. A clear understanding of the background plays a crucial role not only on the performance of the existing muon system [36], but also in the design and preparation for the upgraded detector for the HL-LHC [37].

We use the raw RPC hit rate per strip to measure existing background rates during pp collisions at 7, 8 and 13 TeV [38, 39]. A linear dependence of the RPC hit rate on the LHC instantaneous luminosity is observed up to luminosities of 1.2×10^{34} cm^{-2}·s^{-1}. This linear behavior is true, not only at chamber level, but also for larger parts of the system, such as barrel wheels and endcap disks, as shown in Fig. 3.6.

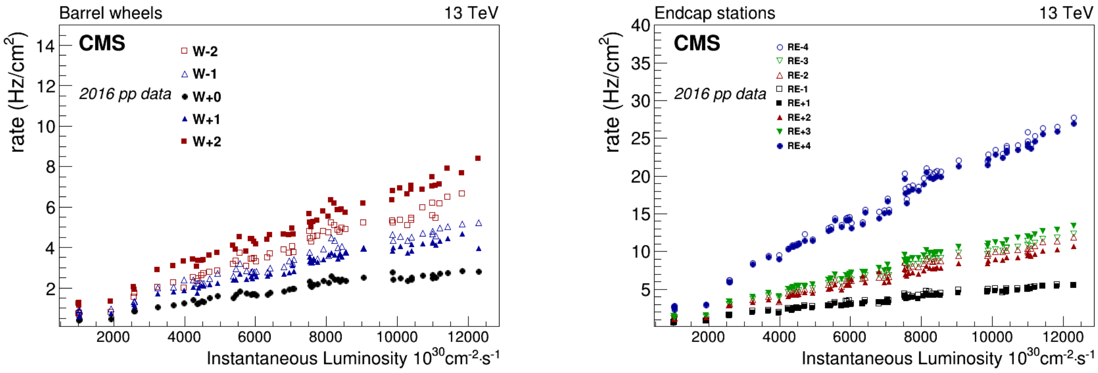

Fig. 3.6 RPC wheels hit rate vs instantaneous luminosity (left). RPC disks hit rate vs instantaneous luminosity (right).

Based on the linear relations between rates and instantaneous luminosity, the RPC hit rates can be extrapolated to an instantaneous luminosity of 5×10^{34} cm^{-2}·s^{-1} to estimate the expected rate at the HL-LHC and also the maximum expected integrated charge on the RPC chambers by the end of the HL-LHC.

Assuming the same linear relationship holds at a luminosity of about one order of magnitude higher, the expected rates at HL-LHC conditions are shown in Fig. 3.7 for all barrel and endcap chambers. A maximum rate about 200 Hz·cm^{-2} is expected. If we apply a safety factor of three, the performance of the detector must be acceptable at a rate of 600 Hz·cm^{-2}.

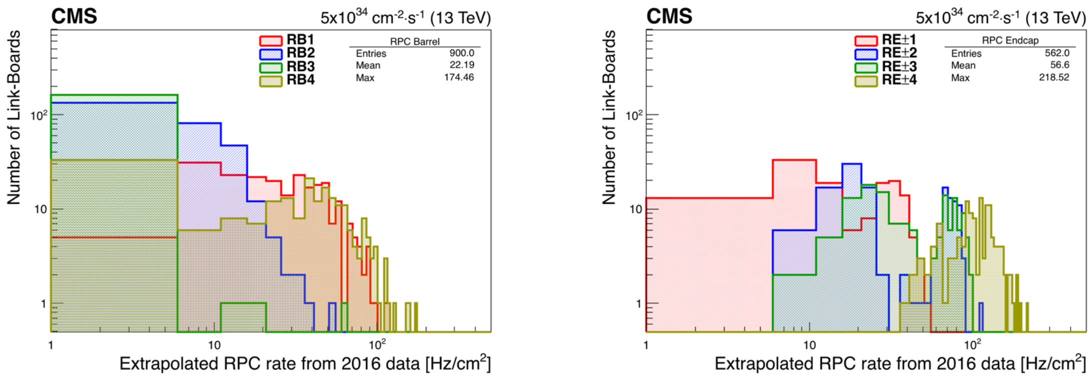

Fig. 3.7 Expected rate extrapolated from 2016 data of single hit rate per unit area to HL-LHC conditions, in the barrel (left) and endcap (right) regions, for the present RPC system.

The maximum expected integrated charge on the RPC chambers can be evaluated on the basis of the expected integrated luminosity at the HL-LHC, which sets an upper limit for the validation of the RPC performance. The maximum integrated charge that any chamber has received in pp collisions by the end of 2016 is about 4.2 mC·cm^{-2}, which corresponds to a luminosity of 45 fb^{-1}. By extrapolating to the expected 3000 fb^{-1} the total integrated charge by the end of the HL-LHC will be 280 mC·cm^{-2} as shown in Fig. 3.8. Including a safety factor of three, the RPCs need to be certified at GIF++ up to 840 mC·cm^{-2}.

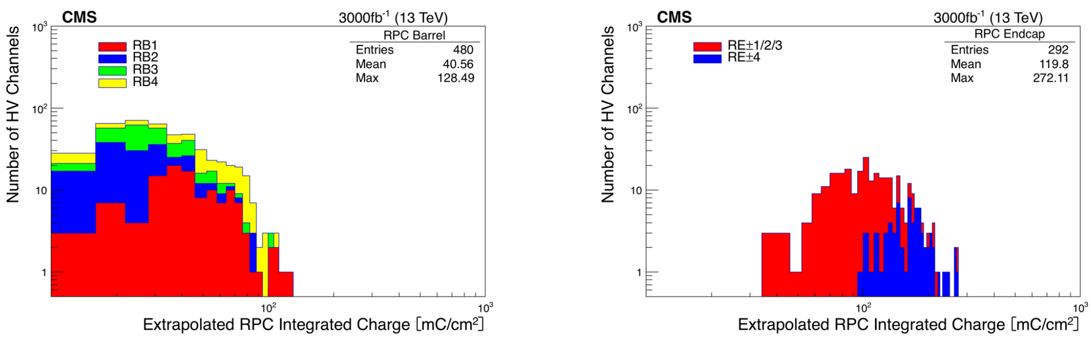

Fig. 3.8 Expected integrated charge during the HL-LHC running (3000 fb^{-1}) in the barrel (left) and endcap (right) regions, for the present RPC system.

3.3.2 GIF++ radiation facility

In order to study the longevity of RPCs in the context of the expected HL-LHC radiation doses, the GIF++ (Gamma Irradiation Facility) [35] test zone started its operation at CERN in 2015. GIF++ features an intense ^{137}Cs source of 662 KeV photons with a set of filters of various attenuation factors. As of March 2016, the intensity of the Cesium source was about 13.5 TBq. The GIF++ photons have an energy fairly representative of the energy of the LHC/HL-LHC photons seen by the muon detectors, between 0.1 MeV and 10 MeV. The source provides continuous irradiation over large areas and has sufficient room for testing several full-size muon detectors at the same time, which makes it an excellent facility for accelerated aging tests of large-size detectors.

3.3.3 Description of the GIF++ tests

Tests have been performed, or are in progress, in order to certify the present RPC system up to the expected HL-LHC conditions: integrated charge of 840 mC·cm^{-2} and background hit rates of 600 Hz·cm^{-2}.

The maximum background rate is expected in the endcap regions, so in July 2016 an irradiation test was started at GIF++ using four spare endcap chambers: two RE2/2 detectors and two RE4/2 chambers. Two different types of chambers have been used for this tests because the endcap RPC production was performed in two periods: in 2005 for all RPCs in the RE1, RE2 and RE3 disks and in 2013 for the RE4/2 and RE4/3 chambers, which were installed during 2015.

To estimate the longevity of the RPCs, one RE2/2 chamber and one RE4/2 chamber are continuously operated under gamma irradiation, while the other two remaining chambers are operated only sporadically and are used as reference. The main detector parameters such as current and counting rates in several background conditions are always monitored and periodically compared with those of the reference chambers. Furthermore, when the muon beam at GIF++ is available, the detector performance, in terms of efficiency and cluster size, is measured with and without background. All measurements are performed under controlled environmental and gas conditions. The detectors are operating with the standard gas mixture (95.2% freon, 4.5% isobutane, and 0.3% SF_6), with two fresh gas volume changes per hour for the irradiated chambers and one for the reference chambers. The relative gas humidity is 40%.

A plot of the integrated charge versus time is shown in Fig. 3.9 for the RE2/2 and RE4/2 chambers. By the end of 2017, about 290 mC·cm^{-2} and 110 mC·cm^{-2} have been integrated in the RE2/2 and RE4/2 detectors, respectively. The charge integrated so far on RE2/2 is about one-third of the total integrated charge target.

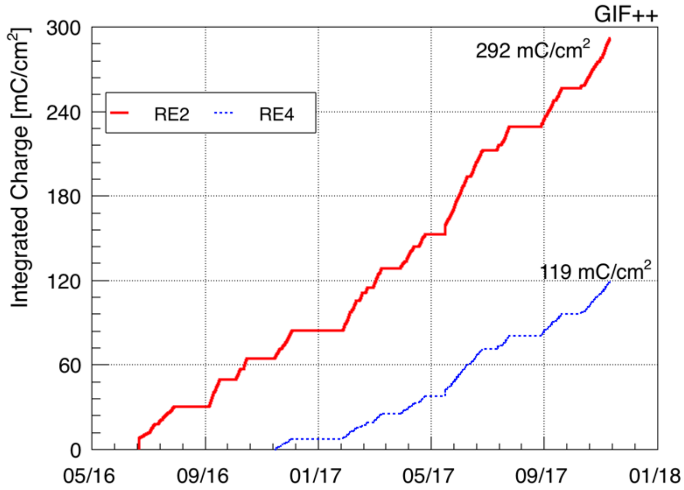

Fig. 3.9 Integrated charge versus time collected during the GIF++ studies for the RE2/2 and RE4/2 chambers.

Since July 2016, several measurements with tests beams have been performed. The efficiency and the cluster size of all four RPCs has been measured in several background conditions, using the removable filters in front of the ^{137}Cs gamma source that allow us to vary the background intensity from 0 to several kHz·cm^{-2}.

In Fig. 3.10, the hit efficiency of the RE2/2 chamber as a function of the effective HV (voltage normalized at the standard temperature and pressure) is reported for various periods of radiation at GIF++ with no irradiation (left) and with a gamma background rate of 600 Hz·cm^{-2} (right). The method for the data analysis is described in Ref. [40]. No signs of aging have been observed so far. The working point, defined as the voltage at which 95% of the maximum efficiency is reached, is unchanged after different periods of irradiation, both under 600 Hz·cm^{-2} and without gamma background rate. The measurements show no reduction in the hit efficiency and the working points are unchanged after different values of integrated charge.

The hit efficiency and the cluster size for both irradiated and the nonirradiated RE2/2 chambers at the working point as a function of the background rate are shown in Fig. 3.11. For all detectors the efficiency is stable in time with a small decrease (2%) of the efficiency at the highest expected background rate of 600 Hz·cm^{-2}. The measurement was repeated after different periods of irradiation corresponding to 18% (153 mC·cm^{-2}) and 31% (260 mC·cm^{-2}) of the total integrated charge target.

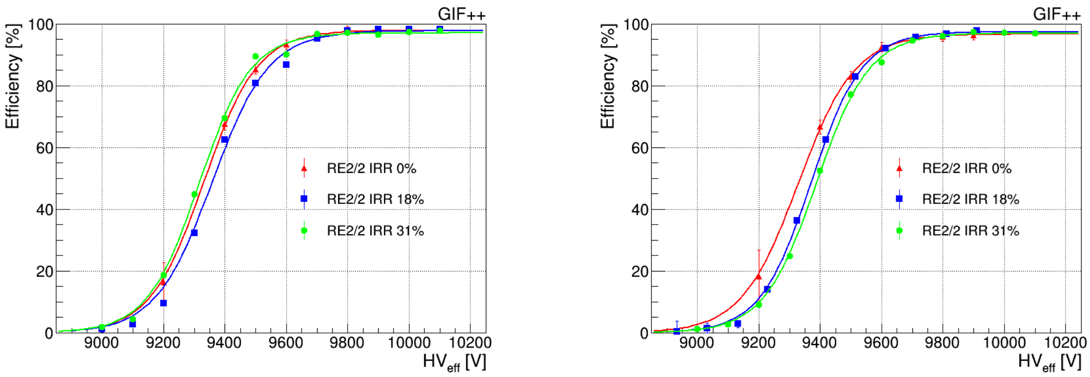

Fig. 3.10 RE2/2 hit efficiency as a function of the effective HV taken with no irradiation (left) and under gamma background rate of about 600 Hz·cm^{-2} (right). No significant variations have been observed in the detector performance.

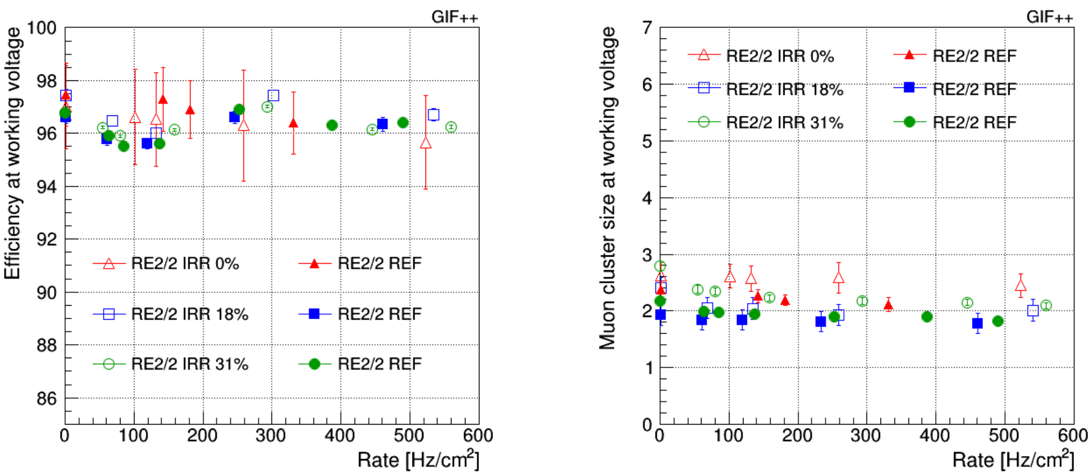

Fig. 3.11 Measurement of the hit efficiency (left) and cluster size (right) at the working point for RE2/2 chambers as a function of the γ rate per unit area. Both irradiated and reference chambers are shown. The measurements have been repeated after different periods of irradiation corresponding to 18% and 31% of the total integrated charge expected by the end of HL-LHC.

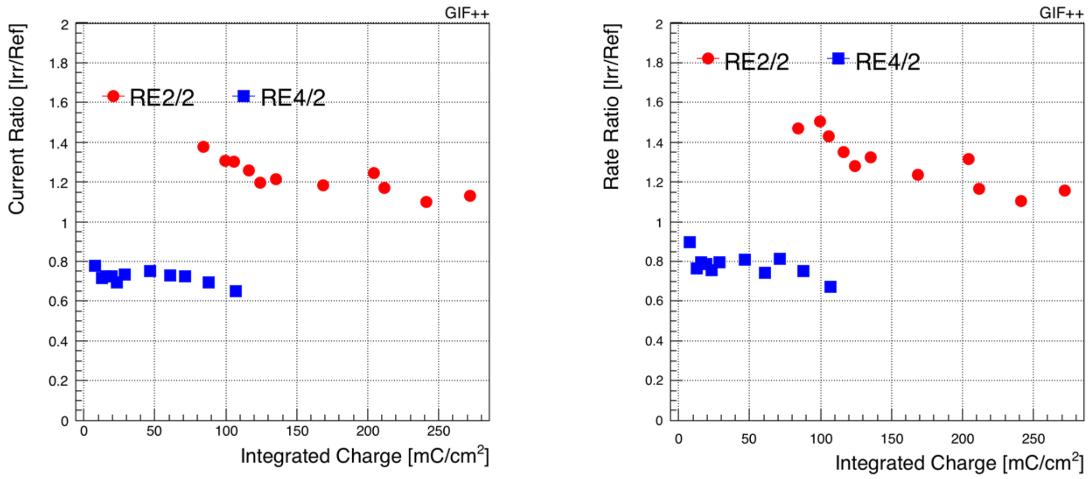

Fig. 3.12 Current (left) and rate (right) ratio between irradiated and nonirradiated reference chambers as a function of the integrated charge. Circles correspond to RE2/2 chambers, squares to RE4/2.

The stability of the system is studied by monitoring the rate and the RPC current, for both irradiated and nonirradiated reference chambers. To cancel out the dependence on the environmental conditions, the ratio of irradiated and reference chambers is measured as a function of the integrated charge as shown in Fig. 3.12. The difference in the ratio between the two chambers is due to the different relative position of RE2/2 and RE4/2 chambers with respect to the reference chambers inside the GIF++ test zone. The measurements show a stable performance of the detectors with a decrease at the beginning of the irradiation period. This decrease can be explained as an electrode resistivity increase due to the low levels of gas flow rate and humidity [41] with respect to the background rate conditions of 1 kHz·cm^{-2}.

3.3.4 Summary

Two CMS RPC double-gap endcap chambers were irradiated with the goal of accumulating an integrated charge of 840 mC·cm^{-2}. The performance and the stability of the detectors were measured as a function of HL-LHC background rates and for various fractions up to one-third of the total integrated charge expected at the end of the HL-LHC. At this point, we observe no sign of performance degradation at the expected high background rates and no aging was observed. Further measurements are needed to achieve the final integrated charge requirements proposed for the longevity study of the present CMS RPC system.

The presented results were published at JINST [42]

Chapter 4

Theoretical motivation and Concepts

4.1 Expectations on the polarization and asymmetry parameter of the Λ_b baryon.

In QCD massless quarks conserves helicity and no single-quark polarization can occur. Once the mass parameter is non zero. the helicity conservation can be violated allowing for helicity flip and thus single-flip helicity amplitudes requires imaginary parts of the amplitudes which are only generated in loop corrections.

The polarizations expected from all QCD subprocesses $qq' \to qq'$, $qg \to qg$, $gg \to q\overline{q}$, $qg \to qg$ and $q\overline{q} \to q'\overline{q}'$ are calculated and summarized in Ref. [1]. The polarization should depend on the quark mass at a given momentum and the heaviest quark acquires the largest polarization. The maximum occurs at $m_q/p_q \simeq 0.3$, where m_q and p_q are the quark mass and momentum, respectively, and the b quark polarization is predicted to be greater an order of magnitude than the s quark. A direct measurement of the polarization of a quark is not possible (except for the top-quark), but it can be deduced from the polarization of the resultant hadrons.

For Λ_b baryons originating from energetic b quark, heavy-quark effective theory (HQET) predicts a large fraction of the transverse b quark polarization to be retained after hadronization [43, 44], while longitudinal polarization should vanish due to parity conservation in strong interactions. Theoretical predictions of the transverse polarization in Λ_b decays are 0.10 [2] and 0.20 [3]. The SM predicts that b quarks from Z^0 have large longitudinal polarization retained by the resultant baryon [43, 45]. The longitudinal Λ_b polarization have been measured at LEP in $e^-e^+ \to Z^0 \to b\overline{b}$, the reported polarizations spread in the range $(-0.79, +0.01)$ [46–48], while the only measurement of the transverse Λ_b polarization in pp collisions was reported by LHCb [49], excluding a polarization of 0.20 at the level of 2.7 standard deviations.

Λ_b baryons can also be produced as decay products of heavier states by strong decays of $\Sigma_b^{*\pm} \to \Lambda_b \pi^{\pm}$[50–53], where the polarization is partially diluted [2, 54]. These strong decays are experimentally difficult to distinguish from Λ_b that hadronize directly from pp collisions, therefore contribute to the measurement presented in this work.

The parity violating asymmetry parameter of the $\Lambda_b \to J/\psi \Lambda$ decay is of particular interest since provide a test for various quark models such pQCD and factorization models. Calculations of this parameter are predicted in many publications. The expectations vary within a wide range, generally between -0.14 and 0.78. Table 4.1 shows the expectations values. A measurement of this parameter is of high interest to point the quark models with realistic predictions.

Table 4.1 Asymmetry parameter predictions in $\Lambda_b \to J/\psi \Lambda$ decays.

Method	Value	Reference
Factorization	-0.1	[55]
Factorization	-0.18	[56]
Covariant oscillator quark model	-0.208	[57]
Perturbative QCD	-0.17 to -0.14	[58]
Factorization (HQET)	0.777	[3]
Light front quark model	-0.204	[59]
Covariant confined quark model	-0.07	[60]

4.2 Parton distribution function.

A precise knowledge of the Parton Distribution Functions (PDFs) of the proton is necessary to have cross section predictions for Standard Model and beyond the Standard Model processes at hadron colliders. The parton density function, $x \cdot g(x, Q^2)$, gives the probability of finding in the proton a parton carrying a fraction x of the proton momentum with Q being the energy scale of the hard interaction. The term parton is used to denote either a gluon, a quark, or an antiquark (valence or from the sea) or . Bjorken-x is the fraction of the proton's momentum carried by a single parton. QCD does not predict the parton content of the proton. The distribution of the PDFs are determined analyzing the experimental data using the DGLAP evolution equations [61–63].

The best knowledge we have for the parton distribution inside the proton comes from deep inelastic scattering (DIS) experiments in *ep* collisions performed at HERA (some recent reviews [64–66]). Fig. 4.1 shows the parton distributions for the valence quarks, sea quarks and gluons measured by HERA combining H1 and ZEUS analysis. The data from HERA has imposed the tightest constrains on the existing PDFs. However, the behaviour at small-x values is still not well established. Different predictions for the gluon distributions are obtained by the groups [67–71] that perform the global analysis of the existing experimental data. For this reason, additional measurements are crucial to improve the understanding of the gluon distribution function. Some proposals are the analysis of experimental results on the heavy quark production at forward rapidities in pp collisions at LHC [72–74] and also the measurement of the vector meson photoproduction cross sections at the LHC [75, 76].

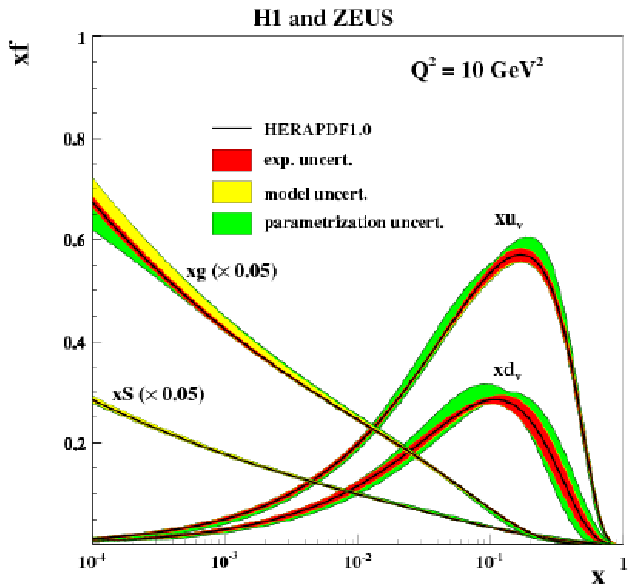

Fig. 4.1 The parton distribution functions xu_v, xd_v, $xS = 2x(\overline{U}+\overline{D})$ and xg at $Q^2 = 10$ GeV, as measured at HERA (combined H1 and ZEUS). The experimental, model and parametrization uncertainties are shown.

4.3 Exclusive photoproduction of vector meson to probe the gluon density of the proton.

Measurements of the exclusive vector meson (VM) photoproduction in photon-hadron and hadron-hadron collisions offer a unique opportunity to explore the behaviour of the gluon density of the proton at small-x values. In the leading logarithmic approximation its cross section is proportional to the gluon density squared [14, 15]:

Experimental results from photon-induced interactions in hadronic colliders have been recently reported by RHIC [77, 78], Tevatron [79], and LHC [80–88]. The idea behind is that in photon-induced processes an ultra relativistic charged hadron (proton or nuclei) give rise to strong electromagnetic fields, so that the photon from the electromagnetic field of one of the two colliding hadrons can interact with one photon of the other hadron (photon-photon process) or can interact directly with the other hadron (photon-hadron process). In photon-hadron processes the total cross section can be factorized in terms of the equivalent flux of photons from the hadron projectile and the photon-hadron production cross section.

4.3.1 Ultra-pheripheral heavy-ions collisions at LHC

Ultra-pheriperal hadron-hadron collisions occurs at large impact parameteres, typically larger than the sum of radii of the interacting particles, and are mediated by the exchange of virtual photons between the incoming particles. An schematic view of an ultra-pheriperal collision is shown in Fig. 4.2

The electromagnetic fields of a fast moving charged particle can be described with an equivalent flux of photons. This idea was first introduced by Enrico Fermi in 1924 [89] and ten years later extended to treat relativistic charged particles by Weizsacker and Williams [90, 91]. The relativistic charged particle (nucleus, proton) generates a flux of virtual photons n(ω) with ω the energy of an individual photon. In ultra-peripheral collisions, there are two kinds of interactions. The first case is a photon-photon interaction, $\gamma\gamma$, in which the radiated photon of the projectile interacts with a photon from the target. The second case, occurs when a photon from the projectile particle hits the target particle.

The beam energies at the LHC are high enough to make the LHC the most energetic photon source ever built. In Pb-Pb collisions the LHC can reach $W_{\gamma\mathrm{Pb}}$ energies up to 500 GeV, while in p–Pb collisions it can reach $W_{\gamma\mathrm{p}}$ up to 1500 GeV in γp interactions.

4.3.2 Exclusive photoproduction of vector mesons.

The cross section for vector meson photoproduction is given by:

$$\sigma_V = \int d\omega \frac{n(\omega)}{k} \sigma^{\gamma H \to VH}(\omega) \qquad (4.1)$$

where ω is the photon energy, $n(\omega)$ the number of photons with energy ω, and $\sigma^{\gamma H \to VH}$ is the photonuclear cross section. The total vector meson cross section in $H+H$ interactions can be calculated from eq. 4.1 by differentiating and changing variable from ω to y, the

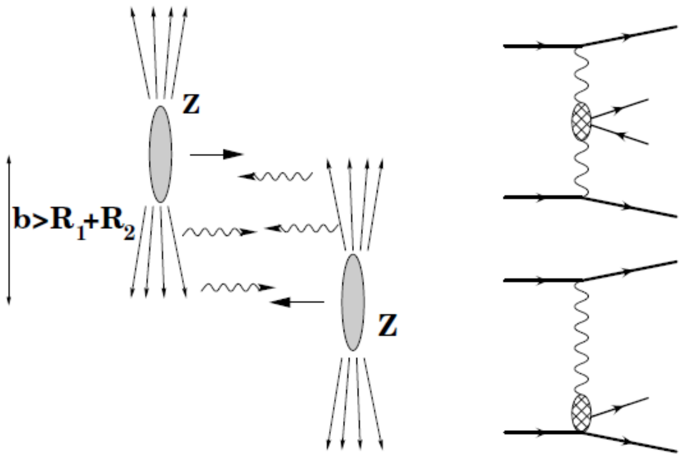

Fig. 4.2 Schematic view of an ultra-peripheral collisions of relativistic nuclei. Ultra pheriperal collisions occur at an impact parameter, b, larger than the sum of the radii, R_1 and R_2 of the interacting particles.

rapidity of the produced VM:

$$\frac{d\sigma\,(H+H\rightarrow H+H+V)}{dy}=n\,(\omega)\,\sigma_{\gamma H\rightarrow VH}\,(\omega)\,. \tag{4.2}$$

Herre the photon energy, ω and y are related as $k=(M_V/2)\exp\{y\}$, and M_V is the mass of the VM. The differential cross section $\frac{d\sigma}{dy}$ gives a direct measure of the VM photoproduction cross section for a given photon energy if the photon flux is known.

The bulk of the photon-hadron cross section can be explained by the photon first fluctuating to a $q\overline{q}$ pair, which interacts strongly with the target. Since the photon has quantum numbers $J^{PC}=1^{--}$, it preferentially fluctuates into a VM. The lifetime of the fluctuation is determined by the uncertainty principle. For a low virtuality photon fluctuating to a state of mass M_V the lifetime is of the order of:

$$\Delta t\approx\frac{1}{M_V}. \tag{4.3}$$

The photon wave function is written as a Fock decompositions:

$$|\gamma>=C_{bare}|\gamma_{bare}>+C_{\rho}|\rho>+C_{\omega}|\omega>+C_{\phi}|\phi>+...+C_q|q\overline{q}>, \tag{4.4}$$

In the above expression, $C_{bare} \approx 1$ and $C_V \sim \sqrt{\alpha_{em}}(V = \rho, \omega, \phi ...)$. The C_V coefficients are related to the photon-vector meson coupling f_V, according to

$$C_V = \frac{\sqrt{4\pi\alpha_{em}}}{f_V}, \tag{4.5}$$

and the numerical values of the couplings are determined from the vector meson leptonic decay widths $\Gamma(V \rightarrow e^+e^-)$

According to the Generalized Vector Meson Dominance Model (GVDM) [92, 93], the scattering amplitudes for the proceses $\gamma + H \rightarrow B$ is the sum over the corresponding vector meson scattering amplitudes,

$$\mathscr{A}_{\gamma+H\rightarrow B}(t) = \sum_V C_V \mathscr{A}_{V+H\rightarrow B}(t) \tag{4.6}$$

In elastic scattering, $\gamma + H \rightarrow V + H$, the cross-terms, e.g $V' + H \rightarrow V + H$ are neglected. Then the cross section is

$$\frac{d\sigma(\gamma + H \rightarrow V + H)}{dt} = C_V^2 \frac{d\sigma(V + H \rightarrow V + H)}{dt} \tag{4.7}$$

where t is the momentum transfer from the target nucleus squared and $d\sigma/dt = |\mathscr{A}|$ is used.

The momentum transfer of the elastic scattering is determined by a hadronic form factor, $F(t)$; thus

$$\frac{d\sigma}{dt} = \left.\frac{d\sigma}{dt}\right|_{t=0} |F(t)|^2. \tag{4.8}$$

For protons, the form factor is well represented by an exponential function, $exp(-b|t|)$ with the parameter slope $b \approx 10$ GeV^{-2} for light vector mesons and $b \approx 4$ GeV^{-2} for the J/ψ, measured from data. The dynamical information is contained in the forward scattering amplitude, $d\sigma/dt(t = 0)$.

At leading order QCD via two-gluon exchange, Fig. 4.3, the forward scattering amplitude is

$$\left.\frac{d\sigma}{dt}(\gamma p \rightarrow V p)\right|_{t=0} = \frac{\alpha_s^2 \Gamma_{ee}}{3\alpha M_v^5 c^6} 16\pi^3 \left[xg\left(x, M_v^2/4\right)\right]^2. \tag{4.9}$$

Here, x is the fraction of the proton momentum carried by the gluons and the gluon distribution $g(x, Q^2)$, is evaluated at a momentum transfer $Q^2 = (Mv/2)^2$. It is clear then that the exclusive vector meson production is sensitive to probe the gluon distribution in protons.

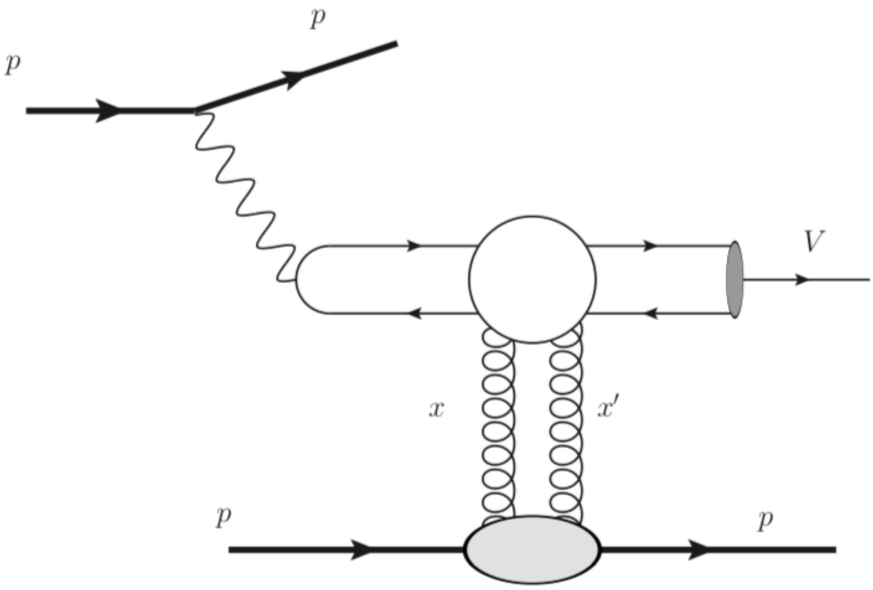

Fig. 4.3 Exclusive vector mesons production in pp collisions.

4.3.3 Exclusive J/ψ photoproduction off protons.

Exclusive J/ψ photoproduction measurements in electron-proton collisions at HERA were performed by H1 and ZEUS. The dependence of the differential cross section on the momentum transfer |t|, and the photoproduction cross section behaviour as function of the center of mass energy of the γp system, $W_{\gamma p}$, were studied. The differential cross section $d\sigma/dt$ was measured by H1 in the range 40 < $W_{\gamma p}$ < 305 GeV and |t| < 1.2 GeV. Their data was parametrized using an exponential form $d\sigma/dt \propto e^{b|t|}$ in different bins of $W_{\gamma p}$. The dependence of the slope parameter on the energy was parametrized as

$$b\left(W_{\gamma p}\right) = b_0 + 4\alpha' ln\left(W_{\gamma p}/W_0\right), \tag{4.10}$$

with the parameters $b_0 = 4.63$ GeV^{-1} and $\alpha' = 0.164$ GeV^{-1} obtained from the fit to their data, and W_0 arbitrarily set to 90 GeV. The energy dependence of the photoproduction cross section was parametrized with a power law:

$$\sigma^{\gamma p \to J/\psi p} = N\left(\frac{W_{\gamma p}}{W_0}\right)^{\delta}, \tag{4.11}$$

where the results from their fit gives $\delta = 0.67 \pm 0.03$. With these results, the gluon density was parametrized as

$$xg\left(x, Q^2\right) = N \cdot x^{-\lambda} \quad (4.12)$$

at the scale $Q^2 = M^2_{J/\psi}/4$ and $\lambda \approx \delta/4$, where $x = \left(M_{J/\psi}/W_{\gamma\text{p}}\right)^2$ and $W^2_{\gamma\text{p}} = 2E_p M_{J/\psi} \exp(-y)$.

Extrapolations of eq. 4.12 to lower-x values demands an increase of the number of gluons with a smaller momentum fraction. The emerge of gluon saturation [4, 5], which is the most straightforward mechanism to slow down the growth of the PDF for gluons carrying a small fraction of the momentum, may become visible by showing a deviation from the power-law parametrization of the photoproduction cross sections tending to lower down the value of the δ parameter obtained using low $W_{\gamma\text{p}}$ energy measurements.

At LHC, J/ψ photoproduction cross sections have been measured by ALICE up to $W_{\gamma\text{p}}$ energies of 700 GeV ($x \approx 2 \times 10^{-5}$) using pPb collisions at 5.02 TeV. ALICE results are consistent with HERA data. Recently, using data from pp collisions at 13 TeV [94], LHCb published their results on the J/ψ photoproduction cross section extending the energy dependence in the range from 600 up to 2000 GeV ($x \approx 3 \times 10^{-5}$ to 2×10^{-6}). They report a deviation from a pure power-law extrapolation of lower energy data from HERA.

At CMS, analyzing data from pPb collisions at 8.16 TeV will allow us to explore the energy dependence of the J/ψ photoproduction in the range of 500 to 700 GeV ($x \approx 4 \times 10^{-5}$ to 2×10^{-5}) which overlap with the energy ranges in ALICE and LHCb measurements, complementing their observations and providing confirmation of the deviation reported by LHCb.

Chapter 5

Measurement of the Λ_b polarization and angular parameters in decays $\Lambda_b \to J/\psi(\mu^+\mu^-)\Lambda(p\pi)$.

A detailed description of the analysis performed to extract the Λ_b polarization and the angular parameters in the decay $\Lambda_b \to J/\psi(\mu^+\mu^-)\Lambda(p\pi)$ is given in this chapter.

5.1 Angular distribution of the decay

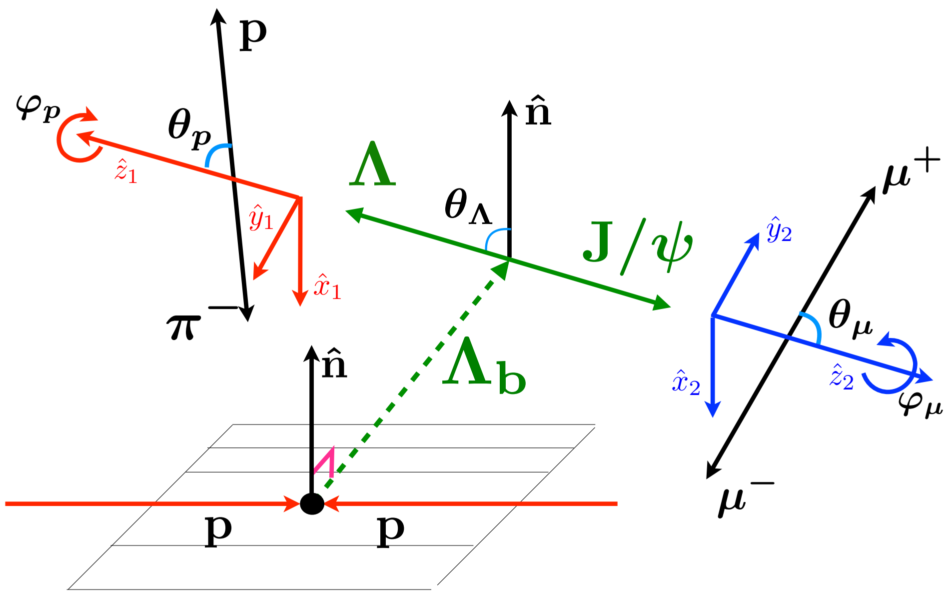

Fig. 5.1 Definition of the angles used to describe the $\Lambda_b \to J/\psi\Lambda$ decay into $\mu^+\mu^-$ $p\pi^-$

The $\Lambda_b \to J/\psi \Lambda$ decay into the $\mu^+\mu^-$ $p\pi^-$ final state, illustrated in Fig. 5.1, can be described in terms of the helicity formalism [95–97]. In pp collisions, the transverse polarization of the Λ_b is defined as the mean value of the Λ_b spin along the unit vector:

$$\hat{n} = \frac{\vec{p}_{\text{beam}} \times \vec{p}_{\Lambda_b}}{\left|\vec{p}_{\text{beam}} \times \vec{p}_{\Lambda_b}\right|}, \tag{5.1}$$

normal to its production plane in the rest frame of Λ_b, where $\vec{p}_{\text{beam}}$ is in the direction of the counterclockwise proton beam direction [11], and $\vec{p}_{\Lambda_b}$ is the Λ_b momentum. In the rest frame of Λ_b the quantization axis z is chosen parallel to $\hat{n}$. The decay is described by four complex helicity amplitudes $T_{\lambda_1\lambda_2}$, with $\lambda_1 = \pm$ 1/2 and $\lambda_2 = \pm$ 1,0 referring to the helicities of the λ and J/ψ particles, respectively. The angular distribution is a function of five decay angles $\left(\theta_\lambda, \theta_p, \theta_\mu, \phi_p, \phi_\mu\right)$ and has the form:

$$\frac{d^5\Gamma}{d\cos\theta_\Lambda d\Omega_p d\Omega_\mu}\left(\theta_\Lambda, \theta_p, \theta_\mu, \varphi_p, \varphi_\mu\right) = \frac{1}{(4\pi)^3}\sum_{i=1}^{20} u_i(T_{\lambda_1\lambda_2})\, v_i(P, \alpha_\Lambda)\, w_i(\theta_\Lambda, \theta_p, \theta_\mu, \varphi_p, \varphi_\mu). \tag{5.2}$$

In expression 5.2, w_i are trigonometric functions, v_i stands for 1, P, α_Λ, or $P\alpha_\Lambda$; P is the Λ_b polarization and α_Λ is the asymmetry parameter in the decay $\Lambda \to p\pi^-$. u_i are bilinear combinations of the helicity amplitudes $T_{\lambda_1\lambda_2}$ [98]. The angle θ_Λ is the polar angle of the Λ momentum measured relative to $\hat{n}$ in the Λ_b rest frame; θ_p and $\phi_p$are the polar and azimuthal angles of the proton, respectively, defined with respect to the axes $\hat{z}_1 = \vec{p_\Lambda}/|p_{\Lambda|}$ and $\hat{y}_1 = (\vec{n} \times \vec{p_\Lambda})/|\vec{n} \times \vec{p_\Lambda}|$ in the rest frame of the Λ; and the angles θ_μ and ϕ_μ are the polar and azimuthal angles, respectively, of the positively charged muon, defined with respect to the axes $\hat{z}_2 = p_{\vec{J}/\psi}/|p_{J/\psi|}$ and $\hat{y}_2 = (\vec{n} \times p_{\vec{J}/\psi})/|\vec{n} \times p_{\vec{J}/\psi}|$ in the J/ψ rest frame. Here, $\vec{p_\Lambda}$ and $p_{\vec{J}/\psi}$ are the momenta of the Λ and J/ψ respectively,and $d\Omega_p = d(\cos\theta_p)d\phi_\mu$ are differential solid angles. Assuming uniform detector acceptance over the azimuthal angles φ_p and φ_μ, the angular distribution can be simplified through an integration over these two angles yielding:

$$\begin{aligned}\frac{d^3\Gamma}{d\cos\theta_\Lambda\, d\cos\theta_p\, d\cos\theta_\mu}(\theta_\Lambda, \theta_p, \theta_\mu) &= \int_{-\pi}^{\pi}\int_{-\pi}^{\pi} \frac{d^5\Gamma}{d\cos\theta_\Lambda\, d\Omega_p\, d\Omega_\mu}(\theta_\Lambda, \theta_p, \theta_\mu, \varphi_p, \varphi_\mu) d\varphi_p\, d\varphi_\mu \\ &\sim \sum_{i=1}^{8} u_i\left(\left|T_{\lambda_1\lambda_2}\right|^2\right) v_i(P, \alpha_\Lambda) w_i(\theta_\Lambda, \theta_p, \theta_\mu).\end{aligned} \tag{5.3}$$

The eight u_i factors are written in terms of only three angular decay parameters α_1, α_2, and γ_0 as proposed in Ref. [98], and the constant 1, which themselves can be written in terms of the $T_{\lambda_1\lambda_2}$ amplitudes as

$$\begin{aligned} 1 &= |T_{++}|^2 + |T_{+0}|^2 + |T_{-0}|^2 + |T_{--}|^2, \\ \alpha_1 &= |T_{++}|^2 - |T_{+0}|^2 + |T_{-0}|^2 - |T_{--}|^2, \\ \alpha_2 &= |T_{++}|^2 + |T_{+0}|^2 - |T_{-0}|^2 - |T_{--}|^2, \\ \gamma_0 &= |T_{++}|^2 - 2|T_{+0}|^2 - 2|T_{-0}|^2 + |T_{--}|^2, \end{aligned} \tag{5.4}$$

where α_1 is the asymmetry parameter for the decay $\Lambda_b \to J/\psi\,\Lambda$, α_2 represents the longitudinal polarization of the Λ, and γ_0 is a parameter that depends on the longitudinal and transverse polarizations of the J/ψ[60]. From the normalization condition and the definitions above the allowed range for α_1 and α_2 is $[-1,+1]$ and for γ_0 is $[-2,+1]$. Moreover, the angular decay parameters are related to the four helicity amplitudes through the following expressions:

$$\begin{aligned} |\,T_{+0}\,|^2 &= \frac{-3(\alpha_1-\alpha_2)+2(1-\gamma_0)}{12}, \qquad & |\,T_{-0}\,|^2 &= \frac{3(\alpha_1-\alpha_2)+2(1-\gamma_0)}{12}, \\ |\,T_{++}\,|^2 &= \frac{3(\alpha_1+\alpha_2)+2(2+\gamma_0)}{12}, \qquad & |\,T_{--}\,|^2 &= \frac{-3(\alpha_1+\alpha_2)+2(2+\gamma_0)}{12} \end{aligned} \tag{5.5}$$

so that, α_1, α_2 and γ_0 are required to satisfy the four additional constraints imposed by the positiveness of $|T_{\lambda_1\lambda_2}|$ and Eq. 5.5:

$$\begin{aligned} 0 &\le -3(\alpha_1-\alpha_2)+2(1-\gamma_0), \\ 0 &\le 3(\alpha_1-\alpha_2)+2(1-\gamma_0), \\ 0 &\le -3(\alpha_1+\alpha_2)+2(2+\gamma_0), \\ 0 &\le 3(\alpha_1+\alpha_2)+2(2+\gamma_0). \end{aligned} \tag{5.6}$$

The CP invariance of Eq. 5.3 implies that the parameters for Λ_b and $\overline{\Lambda}_b$ are related as follows:

$$\begin{aligned} \overline{P} &= -P, \\ \overline{\alpha}_1 &= -\alpha_1, \\ \overline{\alpha}_2 &= -\alpha_2, \\ \overline{\gamma}_0 &= \gamma_0. \end{aligned} \tag{5.7}$$

In addition the CP conservation in $\Lambda \to p\pi^-$ decays implies that $\overline{\alpha}_\Lambda = -\alpha_\Lambda$ [99]. In this analysis, the four parameters $(P, \alpha_1, \alpha_2, \gamma_0)$ are extracted using the angular distribution given in Eq. (5.3), where α_Λ is fixed to its world-average value of 0.642 ± 0.013 [99].

5.2 Event selection

The analysis uses data collected by CMS detector during the LHC Run I (2011 and 2012), from proton-proton collisions at a center-of-mass energy of $\sqrt{s} = 7$ (2011) and 8 TeV (2012), corresponding to an integrated luminosity of 5.28 fb^{-1} (2011) and 19.7 fb^{-1} (2012). The data sets and their integrated luminosities are listed in Table 5.1.

The data were collected with a L1 and HLT trigger designed for events containing a pair of muons that form a vertex. Figure 5.2 shows the dimuon mass distribution from events collected by dedicated dimuon triggers in 2011 data taking.

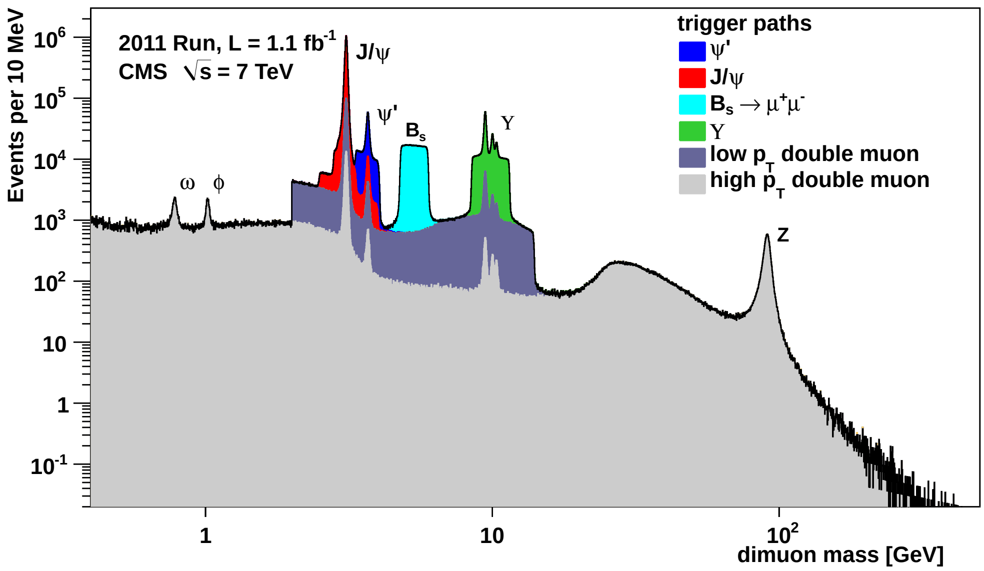

Fig. 5.2 Dimuon mass distribution collected with various dimuon triggers, during the first 1.1 fb^{-1} of data taking in 2011. The colored paths correspond to dimuon triggers with low p_T thresholds collected in a narrow mass window, while the light gray continuous distribution represents events collected with a dimuon trigger with high p_T thresholds. The dark gray band was a "quarkonium" dimuon trigger collected during the first 220 pb^{-1} only [100].

Λ_b reconstruction relies on HLT triggers that require a pair muons coming from a J/ψ with a displace decay vertex from the beam spot BS, The dimuon J/ψ trigger parameter configuration were changed according to the data taking at different center-of-mass energies, with increasingly stringent requirements to maintain an acceptable trigger rate as the instanta-

Table 5.1 Data sample used in this analysis.

Dataset	Integrated luminosity fb^{-1}	
	2011	2012
/MuOnia/Run2011A-May10ReReco-v1/AOD	0.233	–
/MuOnia/Run2011A-PromptReco-v4/AOD	0.984	–
/MuOnia/Run2011A-05Aug2011-v1/AOD	0.476	–
/MuOnia/Run2011A-PromptReco-v6/AOD	0.722	–
/MuOnia/Run2011B-PromptReco-v1/AOD	2.863	–
/MuOnia/Run2012A-22Jan2013-v1/AOD	–	0.876
/MuOnia/Run2012B-22Jan2013-v1/AOD	–	4.412
/MuOnia/Run2012C-22Jan2013-v1/AOD	–	7.054
/MuOnia/Run2012D-22Jan2013-v1/AOD	–	7.363
Total integrated luminosity	5.278	19.705

neous luminosity increased over the time. The requirements of the different trigger versions are summarized below:

- Muon acceptance in the pseudorapidity range$|\eta(\mu)| < 2.2$ and $p_{\mathrm{T}}^{\mu} > 3.5$ or 4 GeV, depending on the version.
- The muons DCA wrt the common vertex in the transverse plane is required to be less than 0.5 cm.
- The dimuon $p_{\mathrm{T}}^{\mu\mu} > 6.5$ or 6.9 GeV depending on the version.
- The χ^2 probability of the fit of the two muons to a common vertex must exceed 0.05, 0.10, or 0.15 from the the earliest to the latest version.
- The distance from the PV and the dimuon vertex in the transverse plane ($L_{xy}(J/\psi)$) must have a value that is at least a factor of three larger than its uncertainty (standard deviation or SD).
- The "pointing" angle (β) between the reconstructed momentum vector $p^{\mu\mu}$ of the dimuon system and the vector pointing from the BS position to the dimuon vertex must have a value of $\cos\beta > 0.9$.
- J/ψ candidates are selected in the invariant mass window 2.5–4.0 GeV and 2.9–3.3 GeV depending on the versions.

Table 5.2 lists the triggers which are fired by events that pass the selection requirements in 2011 and 2012.

Table 5.2 Triggers fired by events in 2011 and 2012.

Trigger path	2011	2012
$HLT\_DoubleMu4\_Jpsi\_Displaced\_v1$	X	
$HLT\_DoubleMu3p5\_Jpsi\_Displaced\_v2$	X	
$HLT\_Dimuon7\_Jpsi\_Displaced\_v1$	X	
$HLT\_DoubleMu4\_Jpsi\_Displaced\_v4$	X	
$HLT\_Dimuon7\_LowMass\_Displaced\_v4$	X	
$HLT\_Dimuon6p5\_LowMass\_Displaced\_v1$	X	
$HLT\_DoubleMu4\_Jpsi\_Displaced\_v5$	X	
$HLT\_Dimuon7\_LowMass\_Displaced\_v3$	X	
$HLT\_DoubleMu3p5\_LowMass\_Displaced\_v6$	X	
$HLT\_DoubleMu4\_Jpsi\_Displaced\_v9$		X
$HLT\_DoubleMu4\_Jpsi\_Displaced\_v10$		X
$HLT\_DoubleMu4\_Jpsi\_Displaced\_v11$		X

5.3 Offline selection

5.3.1 J/ψ selection

The offline selection requires a pair of oppositely charged muons originating from a common displaced vertex to form a J/ψ candidate.

Offline selection is required to be more restrictive than the most-stringent trigger:

- Muons are required to have $p_{\mathrm{T}}^{\mu} > 4\,\mathrm{GeV}$ with the dimuon transverse momentum $p_{\mathrm{T}}^{\mu\mu} > 8\,\mathrm{GeV}$.
- Dimuon invariant mass lying within $\pm 150\,\mathrm{MeV}$ of the world-average J/ψ mass [99].
- Additional requirements are applied as in the trigger selection except for the condition on the colinearity which for the offline selection is set to $\cos\beta > 0.99$. Though this cut reduces the signal events (S) it reduces the background (B), resulting in an increase of significance $S/\sqrt{S+B}$.

The dimuon invariant distribution in J/ψ mass window is shown in Figure 5.3 after the offline selection cuts are applied. Distributions are shown for both 7 and 8 $\sqrt{s} = 8\,\mathrm{TeV}$ data. The J/ψ signal is modeled with the sum of three Gaussian functions with a common mean; a first-order polynomial is used to describe the background.

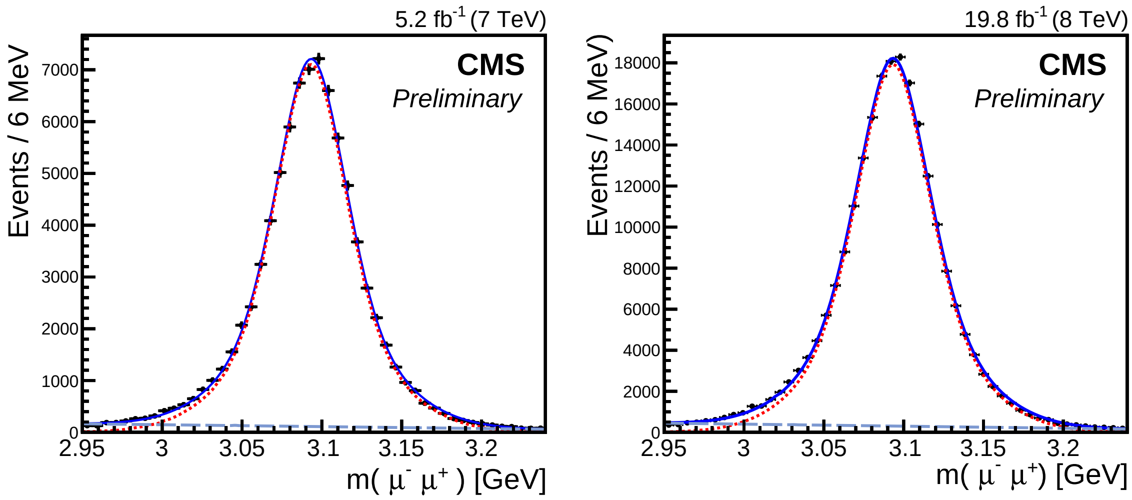

Fig. 5.3 The reconstructed mass distribution of $J/\psi \to \mu^+\mu^-$ candidates in data at center-of-mass of 7 (left) and $\sqrt{s} = 8\,\mathrm{TeV}$ (right). The solid blue line represents the simultaneous fit to 7 and $\sqrt{s} = 8\,\mathrm{TeV}$ data, and the dotted and dashed line represent the signal and background components, respectively.

5.3.2 Λ selection

Λ candidates are reconstructed from their decay into proton and pion (conjugate states are implied) $\Lambda \to p\pi^-$. The Λ decays are constructed from oppositely charged tracks forming a good vertex. The kinematics of $\Lambda \to p\pi^-$ decay requires that $p^{\mathrm{p}} > p^{\pi}$ for all particles, which allows to assign the leading and trailing track to the proton and pion, respectively. The selection of the Λ candidates is detailed in Ref. [101] and has been adopted as the standard selection criteria for long-lived particles in CMS. The selection requirements on the Λ candidates are listed:

- A pair of oppositely charged high purity tracks are fitted to a common vertex with a χ^2(per degree of freedom)< 7, and a vertex probability greater than 2%.
- The d_{xy} of the tracks with respect to the BS is required to be greater than 3 standard deviation SD, where SD represents the square root of the beam spot and vertex uncertainties added in quadrature.
- The world-average proton and pion masses [99] are assigned to the high and low momwntum tracks, respectively.
- The transverse distance of the vertex to the BS, $L_{xy}(\Lambda)$ is required to be greater than 15 SD, where SD represents the square root of the beam spot and vertex uncertainties added in quadrature.

Energy loss (dE/dx) [102] studies performed with the silicon tracker detector [103] show that a large concentration of pions are observed from 0.3 GeV and protons from 1 GeV, Fig. 5.4. It can also be seen that the highest momentum tracks are generally closer to the proton curve (solid red) whereas the lowest momentum track are inconsistent with the proton curve. The small portion of events that do not follow this trend are consistent with background. Additional requirements on the track selection are $p^{\mathrm{p}} > 1\,\mathrm{GeV}$, $p^{\pi} > 0.3\,\mathrm{GeV}$ and $p^{\mathrm{p}\pi} > 1.3\,\mathrm{GeV}$.

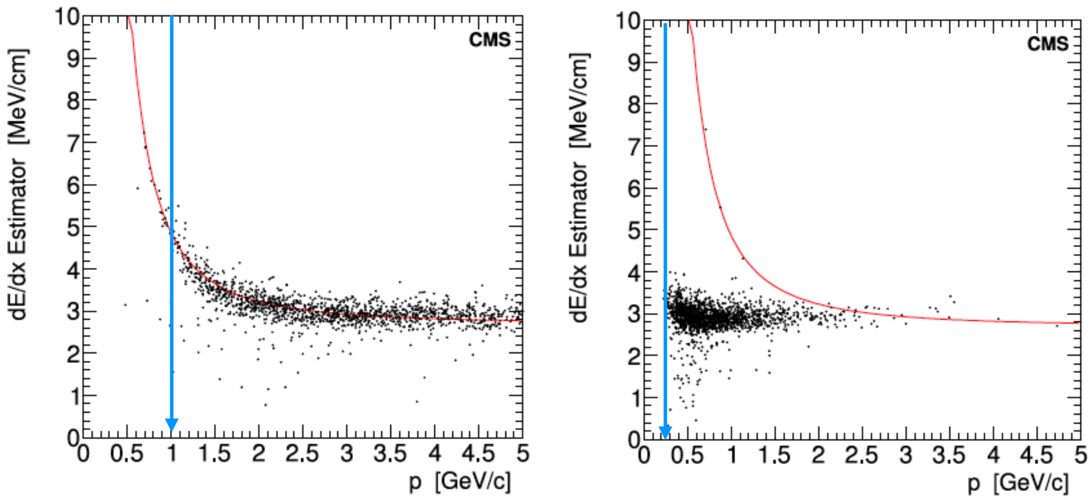

Fig. 5.4 Estimated energy loss as a function of the momentum for the highest (left) and the lowest (right) track from Λ decays. The solid curve represents the proton curve taken from calibration runs [103].

Reflections from $\mathrm{K^0_S} \to \pi^+\pi^-$ decays arises when a pion track is misidentified as a proton. To investigate such reflections, the invariant mass of the ditrack system is reconstructed with the assumption that both tracks are pions, as shown in (Fig. 5.5). A clear $\mathrm{K^0_S}$ peak is observed in the mass distribution, in this case reflections from Λ (where the proton is misidentified as a pion) are distributing on the low mass tail of the $\pi^+\pi^-$ mass distribution. To suppress reflections from $\mathrm{K^0_S}$, events within $\pm 20\,\mathrm{MeV}$ of the $\mathrm{K^0_S}$ mass when the proton candidate is given the pion mass are removed.

The reconstructed $\Lambda \to \mathrm{p}\pi^-$ invariant mass distribution is shown in Fig. 5.6 after all selection cuts are applied. The Λ candidates are selected within the mass range $m_{\mathrm{PDG}} \pm 9\,\mathrm{MeV}$ [99].

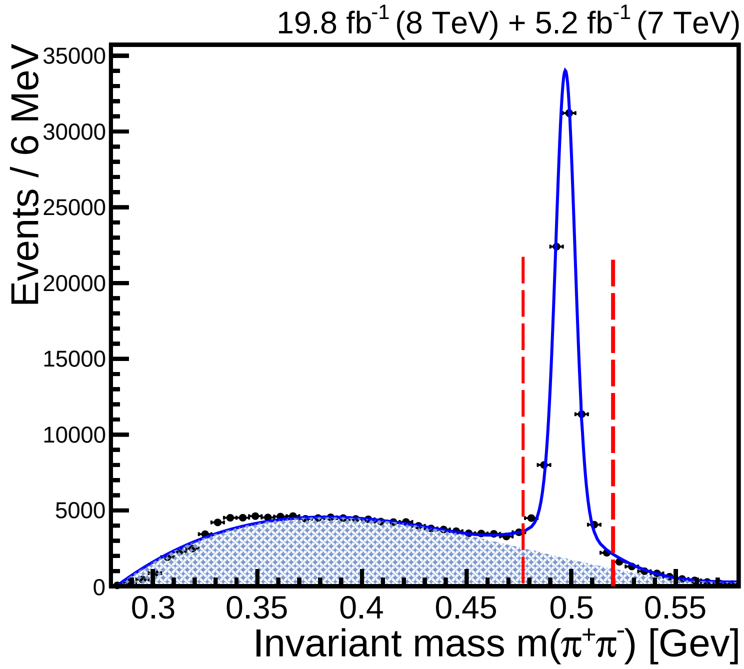

Fig. 5.5 Contamination from $K_S^0 \to \pi^-\pi^+$ candidates when a pion is misidentified as a proton. Events are removed if their invariant mass falls within $\pm 20\,\mathrm{MeV}$ (dashed lines).

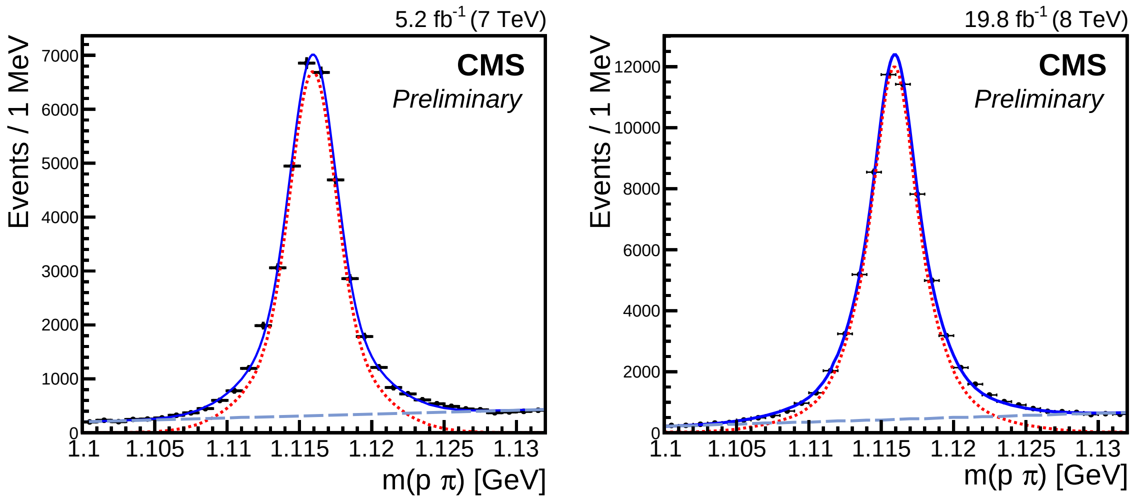

Fig. 5.6 Invariant mass distribution of the Λ candidates after applying the selection criteria to data at center-of-mass of 7 (left) and $\sqrt{s} = 8\,\mathrm{TeV}$. The solid blue line represents the simultaneous fit to $\sqrt{s} = 7$ and $8\,\mathrm{TeV}$ data, and the dotted and dashed line show the signal and background components, respectively.

5.3.3 Λ_b reconstruction and selection

Λ_b candidates are reconstructed combining the J/ψ and Λ candidates into a common vertex and applying mass constraints to the world-average values of the J/ψ and Λ masses [99]; this is done to improve the mass resolution. Further requirements on the p_T and the vertex quality of the Λ_b candidates are applied to reduce the background. Additional cuts include: $p_T^{J/\psi\Lambda} > 10\,\text{GeV}$, and J/$\psi\Lambda$ vertex fit χ^2 probability $> 3\%$. The selected Λ_b and $\overline{\Lambda}_b$ candidates are shown in Figure 5.7 for both $\sqrt{s} = 7$ and 8 TeV data. The Λ_b mass peak is modeled using the sum of two Gaussian functions sharing the same mean, $\mu_{J/\psi\Lambda}$, but with different widths, σ_1 and σ_2:

$$G(m_{J/\psi\Lambda};\mu_{J/\psi\Lambda},\sigma_1,\sigma_2,f) = f\,G_1(m_{J/\psi\Lambda};\mu_{J/\psi\Lambda},\sigma_1) + (1-f)\,G_2(m_{J/\psi\Lambda};\mu_{J/\psi\Lambda},\sigma_2), \quad (5.8)$$

where f is the fraction of the first Gaussian. To describe the background a first-order polynomial, $Q(m_{J/\psi\Lambda};a) = 1 + a\,m_{J/\psi\Lambda}$, is used. The number of signal (N_{sig}) and background (N_{bkg}) events are extracted from an unbinned extended maximum likelihood (ML) fit to the invariant $J/\psi\Lambda$ mass distributions. The fit is performed simultaneously to the four data sets of the Λ_b and $\overline{\Lambda}_b$ candidates at $\sqrt{s} = 7$ and 8 TeV. In this simultaneous fit the only common parameter is $\mu_{J/\psi\Lambda}$, signal and background yields as well as resolutions (widths and fractions) are different for each data sample. The results from the simultaneous fit are presented in Table 5.3. From the fit, the observed Λ_b yields are 981 ± 39 and 2072 ± 55 signal events, and the $\overline{\Lambda}_b$ yields are 916 ± 40 and 1974 ± 53 signal events at $\sqrt{s} = 7$ and 8 TeV, respectively. The deviation of the Λ_b to $\overline{\Lambda}_b$ ratio from 1 is due to the lower efficiency for reconstructing $\overline{\Lambda}_b$ than Λ_b; the $\overline{p}$ are more likely to suffer a nuclear interaction and be lost[104]. DThe definition of both signal and the sideband (SB) background region is based on the common SD given by

$$\text{SD} = \sqrt{f\sigma_1 + (1-f)\,\sigma_2} = 16\,\text{MeV}. \quad (5.9)$$

The signal region is defined as $\mu_{J/\psi\Lambda} \pm 3.5\text{SD}$. The lower SB region is defined as $[5.46, 5.54]$ GeV and the upper SB region as $[5.70, 5.78]$ GeV, which are equivalent to $[\mu_{J/\psi\Lambda} - 10\text{SD}, \mu_{J/\psi\Lambda} - 5\text{SD}]$ and $[\mu_{J/\psi\Lambda} + 5\text{SD}, \mu_{J/\psi\Lambda} + 10\text{SD}]$, respectively. A sketch of the regions are shown in Figure 5.8.

The Λ_b and $\overline{\Lambda}_b$ decays reconstructed are used in an angular analysis to measure the Λ_b polarization, P, and the angular decay parameters α_1, α_2 and γ_0. The measurements are extracted from an 3-dimensional simultaneous fit to the angular variables (observables) $\cos\theta_\Lambda$, $\cos\theta_p$, and $\cos\theta_\mu$ in the four data sets Λ_b, $\overline{\Lambda}_b$ at $\sqrt{s}$=7 and $\sqrt{s}$ =8 TeV.

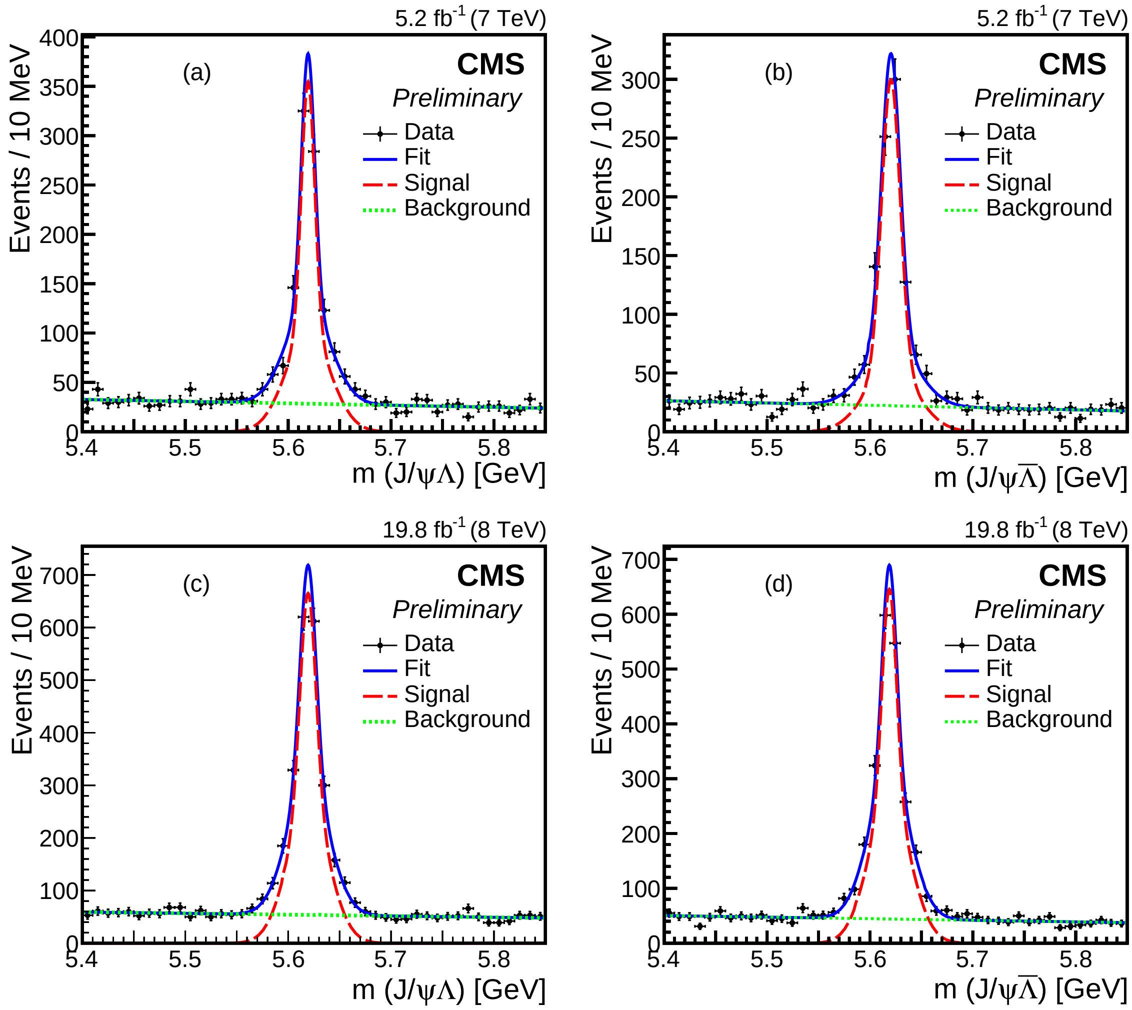

Fig. 5.7 Reconstructed invariant mass for (a) Λ_b, (b) $\overline{\Lambda}_b$ at center-of-mass energy of $\sqrt{s} = 7\,\text{TeV}$, and (c) Λ_b and (d) $\overline{\Lambda}_b$ at $\sqrt{s} = 8\,\text{TeV}$. The solid line indicate the performed fit to the data, where a sum of two Gaussian functions is used to describe the signal (dashed line) and a first-order polynomial to describe the background (dotted line).

Table 5.3 Results of the simultaneous ML fits to $m_{J/\psi\Lambda}$ distributions. Uncertainties are statistical only.

Description	Parameter	Observed values			
		$\sqrt{s} = 7\,\text{TeV}$		$\sqrt{s} = 8\,\text{TeV}$	
		Λ_b	$\overline{\Lambda}_b$	Λ_b	$\overline{\Lambda}_b$
Numb. of bkg candidate	N_{bkg}	945 ± 40	762 ± 38	1832 ± 54	1542 ± 52
Numb. of sig. candidates	N_{sig}	981 ± 39	916 ± 40	2072 ± 55	1974 ± 55
Mean of Gaussian	$\mu\,[\text{GeV}]$	5.6193 ± 0.0002			
Width of Gaussian	$\sigma_1\,[\text{GeV}]$	0.021 ± 0.003	0.024 ± 0.001	0.020 ± 0.001	0.020 ± 0.002
Width of Gaussian	$\sigma_2\,[\text{GeV}]$	0.006 ± 0.001	0.009 ± 0.007	0.007 ± 0.001	0.007 ± 0.001
Double Gaussian fraction	f	0.578 ± 0.076	0.610 ± 0.105	0.625 ± 0.070	0.650 ± 0.073
Bkg. coeff.	a	-0.134 ± 0.056	-0.165 ± 0.063	-0.074 ± 0.040	-0.096 ± 0.044

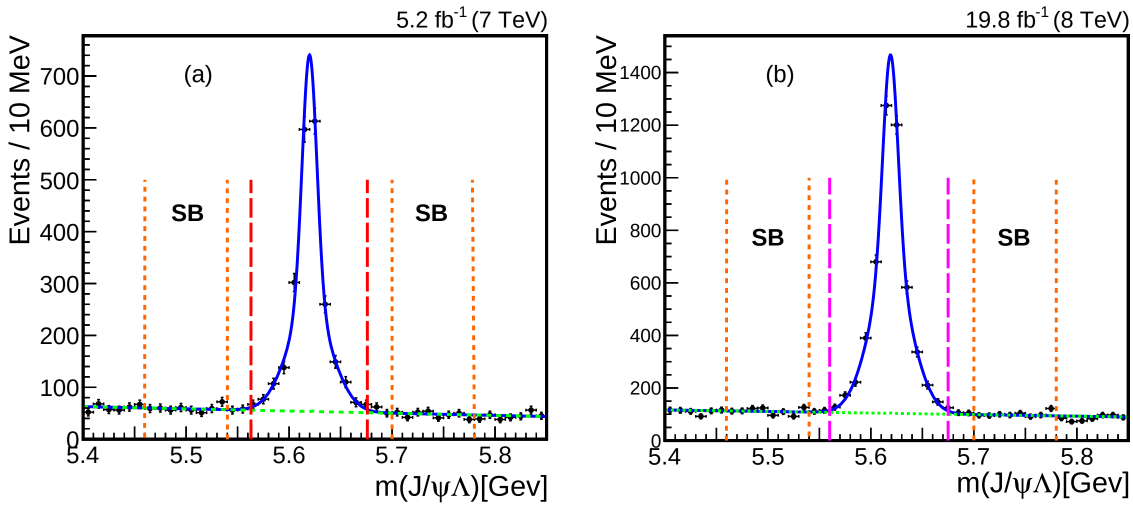

Fig. 5.8 Signal and sidebands (SB) regions of the (a) $m_{J/\psi\Lambda}$ at $\sqrt{s} = 7\,\text{TeV}$ and (b) $m_{J/\psi\Lambda}$ at $\sqrt{s} = 8\,\text{TeV}$.

5.4 Parameter extraction

The extraction of the Λ_b polarization and the angular parameters of the decay are obtained from an extended unbinned maximum likelihood fit [105] to the $J/\psi\Lambda$ invariant mass distribution and the three angular variables $\Theta = (\cos\theta_\Lambda, \cos\theta_p, \cos\theta_\mu)$. The full extended likelihood function used is:

$$L = \exp(-N_{sig} - N_{bkg}) \prod^{N} [N_{sig}\, PDF_{sig} + N_{bkg}\, PDF_{bkg}], \tag{5.10}$$

where N represents the total number of events, N_{sig} and N_{bkg} are the signal and background yields, respectively, and PDF_{sig} and PDF_{bkg} are the probability density functions (PDFs) for the signal and background, respectively. The strategy considers the shape of the distributions and the number of signal and background events.

The signal PDF is a 4D function of the $J/\psi\Lambda$ mass and the three angular variables factorized as:

$$PDF_{sig} = F_{sig}(\Theta)\,\varepsilon(\Theta)\,G(m_{J/\psi\Lambda}), \tag{5.11}$$

where $F_{sig}(\Theta)$ represents the angular distribution at particle level given by Eq. 5.3, $G(m_{J/\psi\Lambda})$ stands for the sum of two Gaussian functions used to model the invariant mass distribution as in Eq. 5.8, and $\varepsilon(\Theta)$ is angular efficiency. The effect of the detector on the angular distribution is taken into account by the factor ε that represents the efficiency as a function of the angles, and its obtained from simulation as discussed in Sec 5.4.1. To model the background events the $\mathrm{PDF_{bkg}}$ is defined as

$$\mathrm{PDF_{bkg}} = \mathrm{F_{bkg}}(\Theta)\, Q(m_{\mathrm{J}/\psi\Lambda}), \tag{5.12}$$

where a first-order polynomial $Q(m_{\mathrm{J}/\psi\Lambda})$ is used to model the invariant mass distribution. The angular background distributions are modeled with the function $F_{\mathrm{bkg}}(\Theta)$, which is obtained using events from SB of the invariant mass distribution as discussed in Sec. 5.4.2.

The full likelihood function in Eq. (5.10) is minimized by fitting simultaneously the four data sets for Λ_b and $\overline{\Lambda}_\mathrm{b}$ at $\sqrt{s} = 7$ and $8\,\mathrm{TeV}$, with P, α_1, α_2, and γ_0 as common parameters. The parameters in the angular background model, efficiency distributions, and the signal and background mass models are obtained from independent fits and fixed in the full ML function

5.4.1 Efficiency shapes

Effects from the detector reconstruction itself and the selection cuts in the angular distributions are introduced in the efficiency term. The efficiency shapes are estimated from MC simulation where $\Lambda_\mathrm{b} \to \mathrm{J}/\psi\,\Lambda$ decays are generated using the EVTGEN phase space (PHSP) decay models to generate uniform angular distributions. The flat distributions are shown in Fig. 5.9. The original flat distributions at generation level (Fig. 5.9) are distorted after full

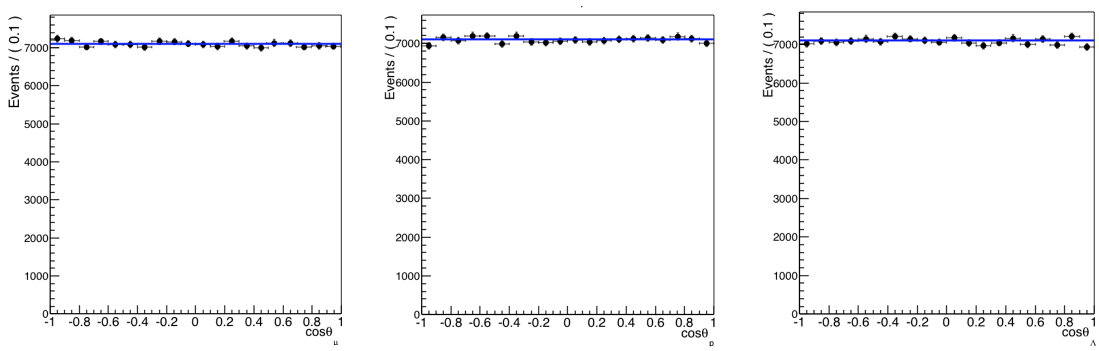

(a) $\cos\theta_\mu$ (b) $\cos\theta_\mathrm{p}$ (c) $\cos\theta_\Lambda$

Fig. 5.9 Angular distributions of the decay $\Lambda_\mathrm{b} \to \mathrm{J}/\psi\,\Lambda$ using the PHSP decay model in EVTGEN.

simulation and selection (Fig. 5.10). After applying the same reconstruction and selection processes to generated MC events, a few combinatorial background may remain affecting the efficiency calculation. The remaining background events are removed by means of the the SB subtraction method, which is based on the assumption that the background below the signal peak has the same form as in the SB region. The signal and SB regions are defined using the $m_{J/\psi\Lambda}$ mass distribution as in Sec. 5.3.3 and used to create two 3D histograms of the angular variables with events in the signal and SB regions, respectively. The ratio of the integrals of those histograms is taken to get the scale factor. Finally the SB histogram is scaled and subtracted from the signal-region histogram. The resulting distributions are an estimate of the pure signal events. The angular shapes after full simulation and background subtraction are shown in Fig. 5.10. From the background-substracted simulation, a comparison of data/simulation is performed to find possible differences between them. To ensure that the simulation reproduces the data a reweighting procedure is performed to background-substracted MC. Then the corrected simulation is used to obtain the efficiency distributions (Fig. 5.10). As mentioned before, reconstruction efficiencies are different for Λ_b and $\overline{\Lambda}_b$ therefore the angular efficiency models are obtained independently for Λ_b and $\overline{\Lambda}_b$. In addition, to account for any possible difference in the conditions of the detector (alignment, calibration, etc..) from the 7 TeV to the 8 TeV data taking, independent efficiency models were used for each year.

To model the efficiency a product of three Chebyshev polynomials is used:

$$\varepsilon(\cos\theta_\Lambda, \cos\theta_p, \cos\theta_\mu) = \prod_{i=\Lambda,p,\mu} \left(\sum_{j}^{N_i} A_{ij} T_j(\cos\theta_i)\right), \tag{5.13}$$

where N_i is the maximal degree of the Chebyshev polynomials to be determinate. The free coefficients A_{ij} are obtained for Λ_b and $\overline{\Lambda}_b$ at $\sqrt{s} = 7$ and $\sqrt{s} = 8\,\text{TeV}$ from separate likelihood fits. The simulated efficiency distributions and the resulting fits are shown in Figure 5.11. It can be seen from Fig. 5.11 that this parametrization describes well the shapes of the distributions. Information of the goodness of fit in terms of χ^2/dof per degree of freedom is presented in Table 5.4.

Table 5.4 Resulting χ^2/dof by fitting the efficiency distributions

Observable	$\sqrt{s} = 7\,\text{TeV}$		$\sqrt{s} = 8\,\text{TeV}$	
	Λ_b	$\overline{\Lambda}_b$	Λ_b	$\overline{\Lambda}_b$
$\cos\theta_\Lambda$	2.4	1.3	1.4	1.2
$\cos\theta_p$	1.4	0.9	0.9	0.9
$\cos\theta_\mu$	1.5	1.9	1.3	1.5

5.4.2 Angular background estimation

The angular background model used in the final fit is obtained from the SB events. The SB angular distributions are modeled using Chebyshev polynomials of the first kind for $\cos\theta_\Lambda$

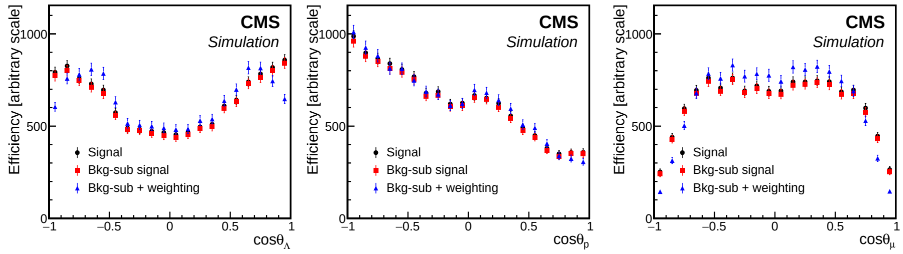

(a)

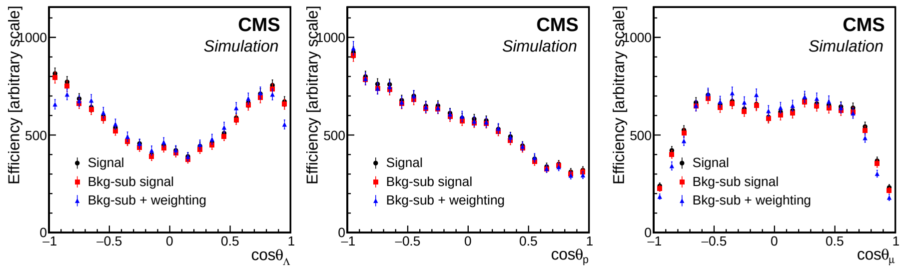

(b)

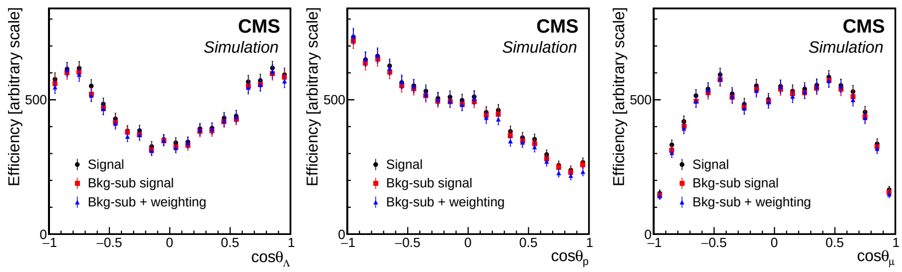

(c)

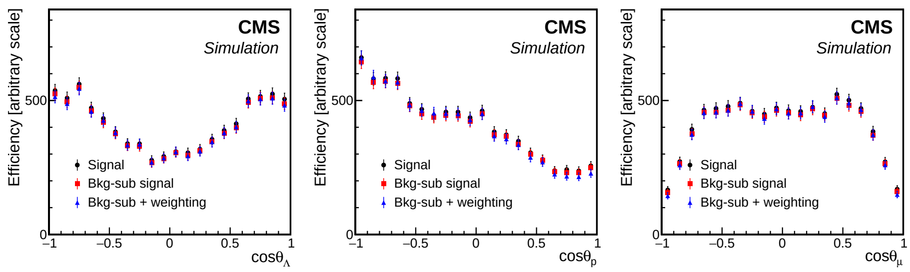

(d)

Fig. 5.10 Efficiency distributions of $\cos\theta_\Lambda$, $\cos\theta_\mathrm{p}$, $\cos\theta_\mu$ (from left to right) from full simulations of (a) $\Lambda_\mathrm{b} \to \mathrm{J}/\psi\,\Lambda$ and (b) $\overline{\Lambda}_\mathrm{b} \to \mathrm{J}/\psi\,\Lambda$ decays at $\sqrt{s} = 7\,\mathrm{TeV}$, and (c) $\Lambda_\mathrm{b} \to \mathrm{J}/\psi\,\Lambda$ and (d) $\overline{\Lambda}_\mathrm{b} \to \mathrm{J}/\psi\,\Lambda$ decays at $\sqrt{s} = 8\,\mathrm{TeV}$. The black dots represent the signal events, the squares represent the background-subtracted signal, and triangles show simulation after background subtraction and weighting process.

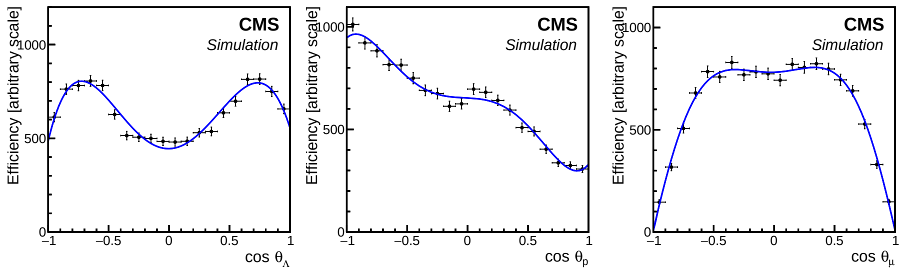

(a)

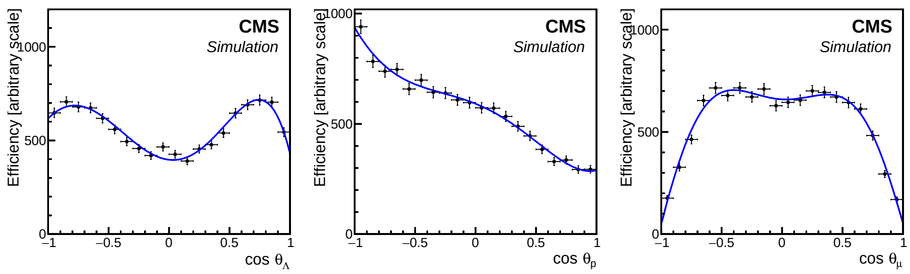

(b)

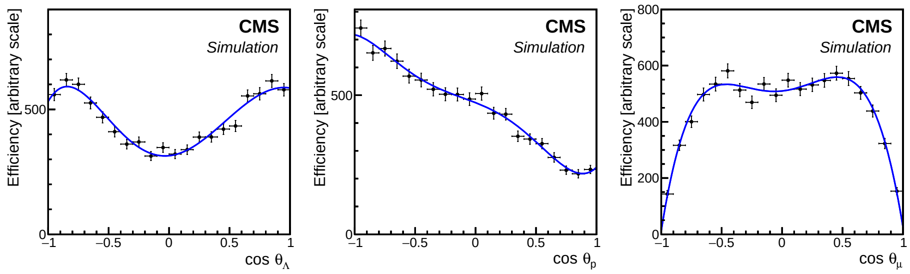

(c)

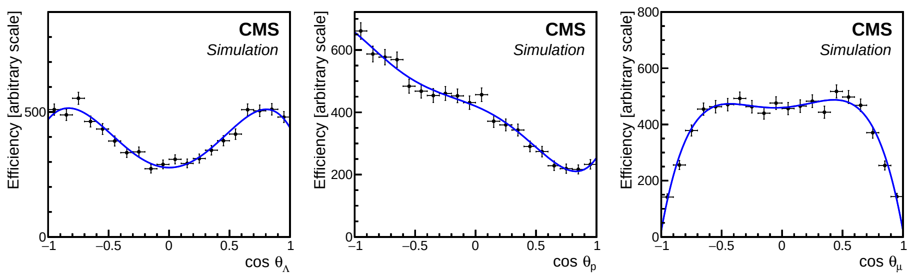

(d)

Fig. 5.11 The efficiencies as a function of $\cos\theta_\Lambda$, $\cos\theta_p$, $\cos\theta_\mu$ (from left to right) obtained from simulated (a) $\Lambda_b \to J/\psi\Lambda$ and (b) $\overline{\Lambda}_b \to J/\psi\Lambda$ decays at $\sqrt{s} = 7\,\text{TeV}$, and (c) $\Lambda_b \to J/\psi\Lambda$ and (d) $\overline{\Lambda}_b \to J/\psi\Lambda$ decays at $\sqrt{s} = 8\,\text{TeV}$. The vertical bars on the points are the statistical uncertainties in the simulated data and the lines show the projections of a 3D fit to the distributions using Chebyshev polynomials.

and $\cos\theta_p$ and error functions are used to describe the distribution in $\cos\theta_\mu$. These functions are combined as follows:

$$F_{bkg}(\Theta) = (\sum_{i=0}^{n_\Lambda} b_i T_i(\cos\theta_\Lambda))(\sum_{j=0}^{n_p} c_j T_j(\cos\theta_p))\,E(\cos\theta_\mu), \tag{5.14}$$

where b_i and c_j are the parameters to be determined, n_Λ and n_p represent the maximal degree of the T_i Chebyshev polynomials, and E is defined as

$$E(\cos\theta_\mu) = (1+\mathrm{erf}(\frac{\cos\theta_\mu - d_1}{d_2}))(1+\mathrm{erf}(\frac{-\cos\theta_\mu - d_3}{d_4})). \tag{5.15}$$

The b, c and d parameters are determined from separated 3D fits to the four data sets Λ_b and $\overline{\Lambda}_b$ in 2011 and 2012 and fixed in the complete likelihood function (Eq. 5.10). The results of the fits are shown in Figure 5.12. The $\cos\theta_p$ distributions are well described by fourth order polynomials, while to model $\cos\theta_\Lambda$ distributions polynomials up to sixth order are used. The χ^2/dof of the resulting angular projections can be found in Table 5.5.

Table 5.5 Resulting χ^2/dof for the unbinned likelihood fit to the sidebands angular distributions

Observable	$\sqrt{s}=7\,\mathrm{TeV}$		$\sqrt{s}=8\,\mathrm{TeV}$	
	Λ_b	$\overline{\Lambda}_b$	Λ_b	$\overline{\Lambda}_b$
$\cos\theta_\Lambda$	1.53	2.06	1.25	0.87
$\cos\theta_p$	0.93	0.91	1.02	1.42
$\cos\theta_\mu$	0.38	0.72	0.84	0.76

5.5 Fit results

The complete likelihood function in Eq. (5.10) is maximized by fitting simultaneously the four data sets for Λ_b and $\overline{\Lambda}_b$ at $\sqrt{s}=7$ and $8\,\mathrm{TeV}$ to extract the 4 common parameters: P, α_1, α_2, and γ_0. The simultaneous fit is performed on the enriched signal mass range: within 3.5 SD's around the mean Λ_b mass. This range contains more than 99.9% of the signal events, and significantly reduces the number of background events making the fit less sensitive to the background modeling. The fit parameters for the angular background and efficiency distributions are fixed to those values found in the previous fits described in Secs. 5.4.1 and 5.4.2. The signal and background mass parameters are obtained from independent separate fits to the mass distribution detailed in Sec. 5.3.3, and the numbers of signal and backgrounds

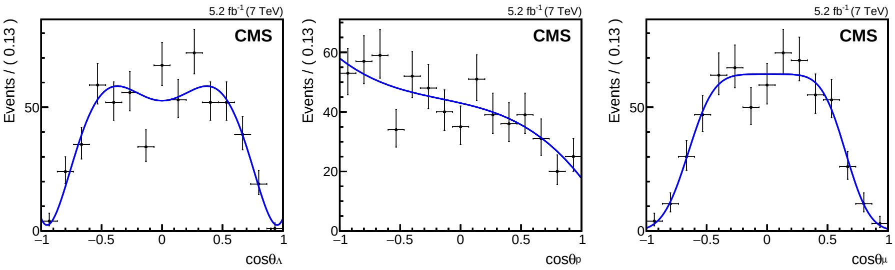

(a)

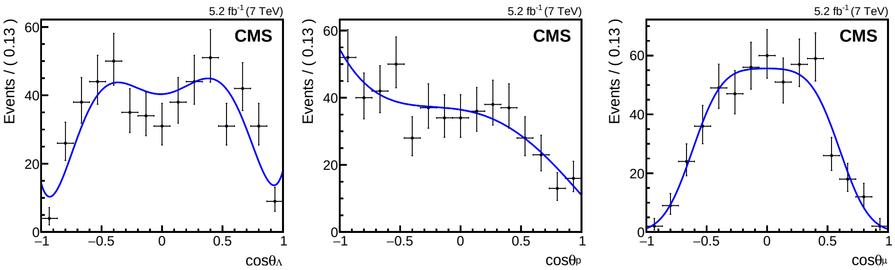

(b)

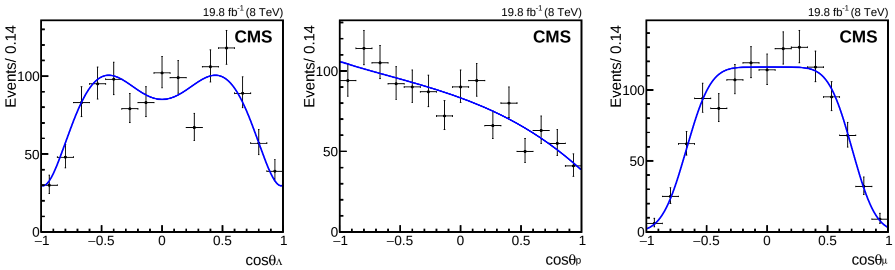

(c)

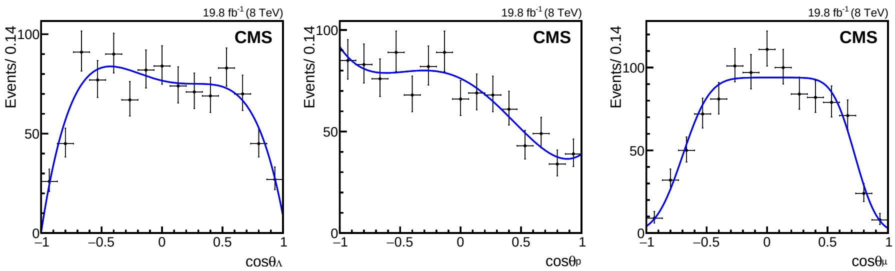

(d)

Fig. 5.12 Angular background of $\cos\theta_\Lambda$, $\cos\theta_\mathrm{p}$, $\cos\theta_\mu$ (from left to right) distributions for (a) Λ_b and (b) $\overline{\Lambda}_\mathrm{b}$ decays at $\sqrt{s} = 7\,\mathrm{TeV}$, and (c) Λ_b and (d) $\overline{\Lambda}_\mathrm{b}$ decays at $\sqrt{s} = 8\,\mathrm{TeV}$. The vertical bars on the points are the statistical uncertainties in SB data and the solid line shows the projections of a 3D fit to the distributions using Chebyshev polynomials and the complementary error functions described in Eq 5.14.

events are fixed to their propagated values in the signal mass region. The resulting fit values of the polarization and the three angular decay parameters are:

$$\begin{aligned} P &= 0.00 \pm 0.06, \\ \alpha_1 &= 0.14 \pm 0.14, \\ \alpha_2 &= -1.11 \pm 0.04, \\ \gamma_0 &= -0.27 \pm 0.08, \end{aligned}$$

where the uncertainties are statistical only. The correlation matrix of the fitted parameters is shown in Table 5.6. No strong correlations are found among these parameters. Translating these values to the squares of the helicity amplitudes given by Eqs. 5.5 and using the correlation factors in Table 5.6, the results are:

$$\begin{aligned} |T_{++}|^2 &= 0.05 \pm 0.04, \\ |T_{+0}|^2 &= -0.10 \pm 0.04, \\ |T_{-0}|^2 &= 0.51 \pm 0.03, \\ |T_{--}|^2 &= 0.52 \pm 0.04, \end{aligned}$$

where the uncertainties are only statistical and are propagated according to the correlation matrix in Table 5.6. The projections of the fit are shown in Figs. 5.13 and 5.14 for Λ_b and $\overline{\Lambda}_b$, respectively, using the combined data at $\sqrt{s} = 7$ and 8 TeV.

Table 5.6 Correlation matrix for the fitted parameters.

Parameter	P	α_1	α_2	γ_0
P	1	−0.039	−0.029	0.116
α_1		1	−0.207	−0.030
α_2			1	0.285
γ_0				1

5.6 Toy Monte Carlo studies

As the ML fit is intrinsically biased. The fit needs to be validated.

The bias of an estimator is the average deviation of the estimate from its true value:

$$b(\iota) = <\hat{\iota} - \iota> = <\hat{\iota}> - \iota.$$

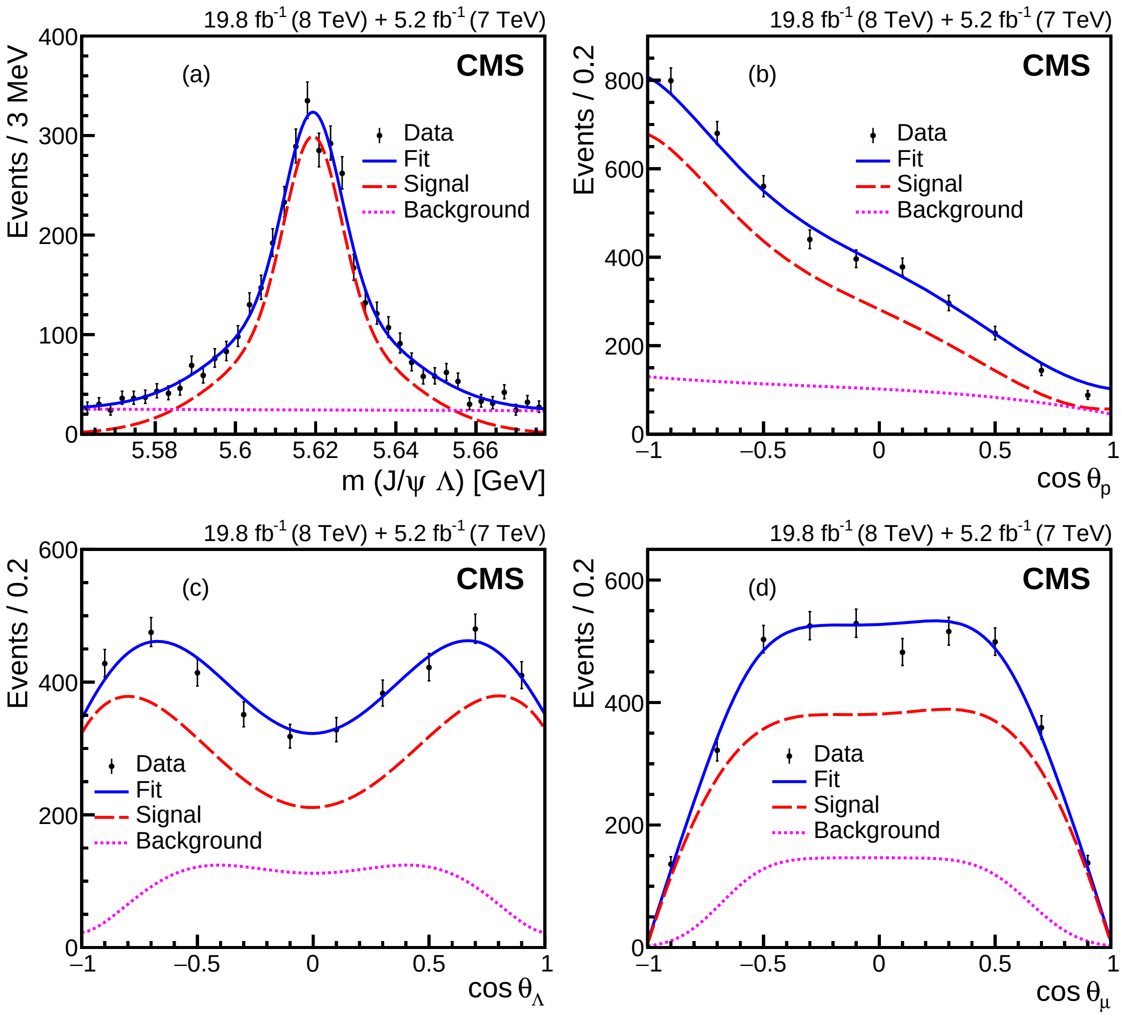

Fig. 5.13 Distributions in (a) $m_{J/\psi\Lambda}$, (b) $\cos\theta_p$, (c) $\cos\theta_\Lambda$, and (d) $\cos\theta_\mu$ for Λ_b candidates in the combined $\sqrt{s} = 7$ and $8\,\text{TeV}$ data. The vertical bars on the points are the statistical uncertainties in the data, the solid line shows the result of the fit, and the dashed and dotted lines represent, respectively, the signal and background contributions from the fit.

A bias due to the fitting procedure is investigated using toy Monte Carlo samples generated according to the total 2011, 2012 PDF's for Λ_b and $\overline{\Lambda}_b$. The samples are generated in the mass region ($[\mu - 10\sigma, \mu + 10\sigma]$) with the number of signal and background events in accordance with the numbers observed in data, then a fit in the reduced region ($[\mu - 3.5\sigma, \mu + 3.5\sigma]$) of the $m(J/\psi\Lambda)$ invariant mass peak is performed. The simultaneous full likelihood fit is then applied to the generated samples to test if the fit is able to recover the input values of the angular decay parameters and the Λ_b polarization used to generate the samples. Results from 1,000 pseudo-experiments were used to study the distributions for the four fitted parameters and their corresponding pull distributions, where the pull of a quantity x in the

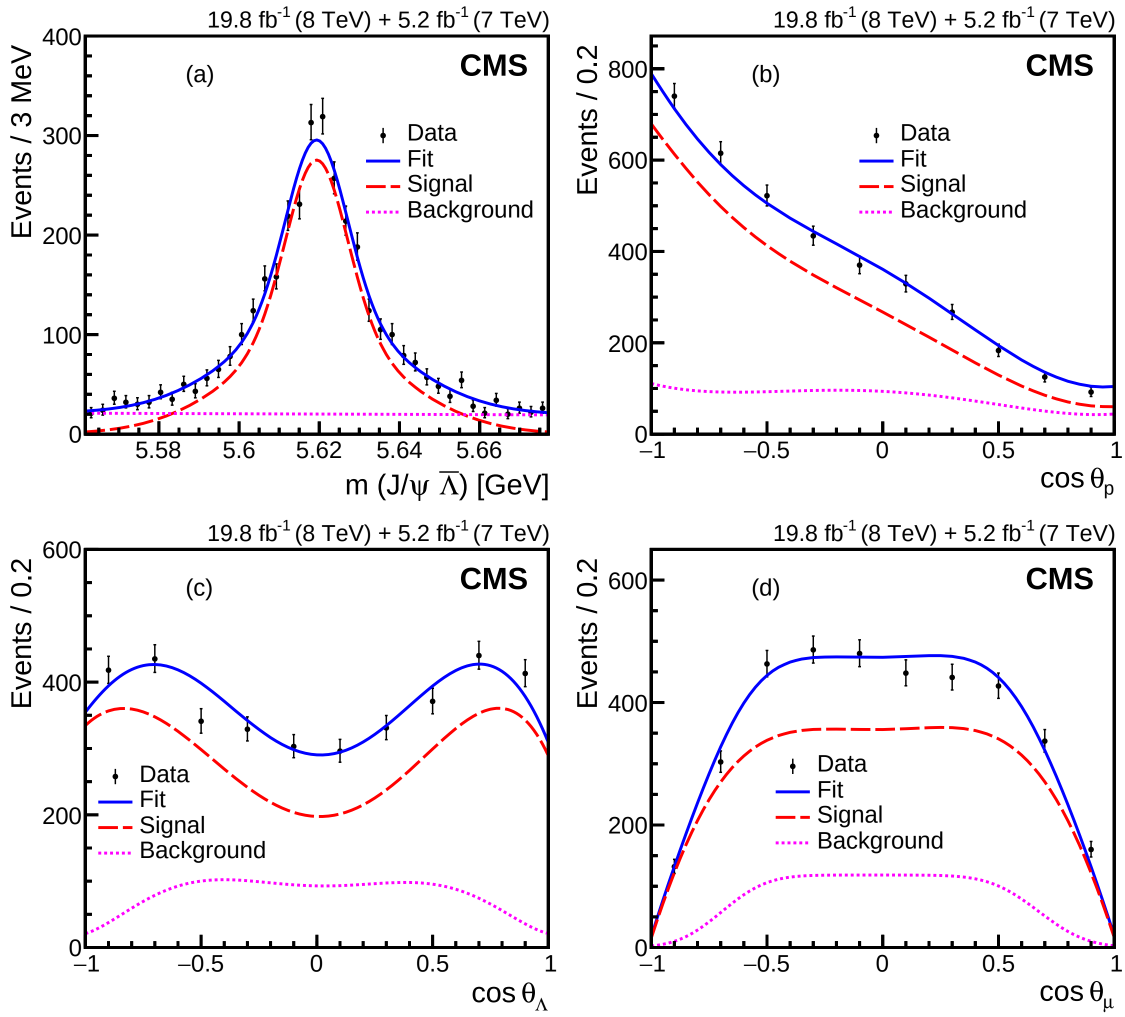

Fig. 5.14 Distributions in (a) $m_{J/\psi\overline{\Lambda}}$, (b) $\cos\theta_{\mathrm{p}}$, (c) $\cos\theta_{\Lambda}$, and (d) $\cos\theta_{\mu}$ for $\overline{\Lambda}_{\mathrm{b}}$ candidates in the combined $\sqrt{s} = 7$ and 8 TeV data. The vertical bars on the points are the statistical uncertainties in the data, the solid line shows the result of the fit, and the dashed and dotted lines represent, respectively, the signal and background contributions from the fit.

i-th pseudo-experiment is defined as

$$pull(x_i) = \frac{x_i^{fit} - x_i^{true}}{\sigma_i^{fit}} \tag{5.16}$$

with x_i^{fit} being the fitted value, x_i^{true} the true (generated) value and σ_i^{fit} is the error on x_i^{fit} computed by the fit. Pulls normally distributed with a mean value at 0 indicates no bias, and width at 1 suggest that the errors are correctly calculated. The distributions of the fitted parameters are shown in Fig. 5.15 with their error distribution in Fig. 5.16, and their corresponding pulls distributions. Fig. 5.17 show that the fit is able to recover the input values. Table 5.7 presents the central values of the fit results and the pull distributions along with the values used to generate the test samples.

Table 5.7 Input values and results from 1,000 toy Monte Carlo pseudo-experiments

Parameter	Input Value	Fit results	pull mean	pull deviation	pull width
P	0.00	0.001 ± 0.002	-0.006 ± 0.034	0.4σ	1.04 ± 0.02
α_1	0.12	0.123 ± 0.004	-0.0192 ± 0.030	0.97σ	1.14 ± 0.02
α_2	-0.93	-0.931 ± 0.04	-0.019 ± 0.030	0.64σ	0.95 ± 0.02
γ_0	-0.45	-0.452 ± 0.002	-0.032 ± 0.031	1.1σ	1.03 ± 0.02

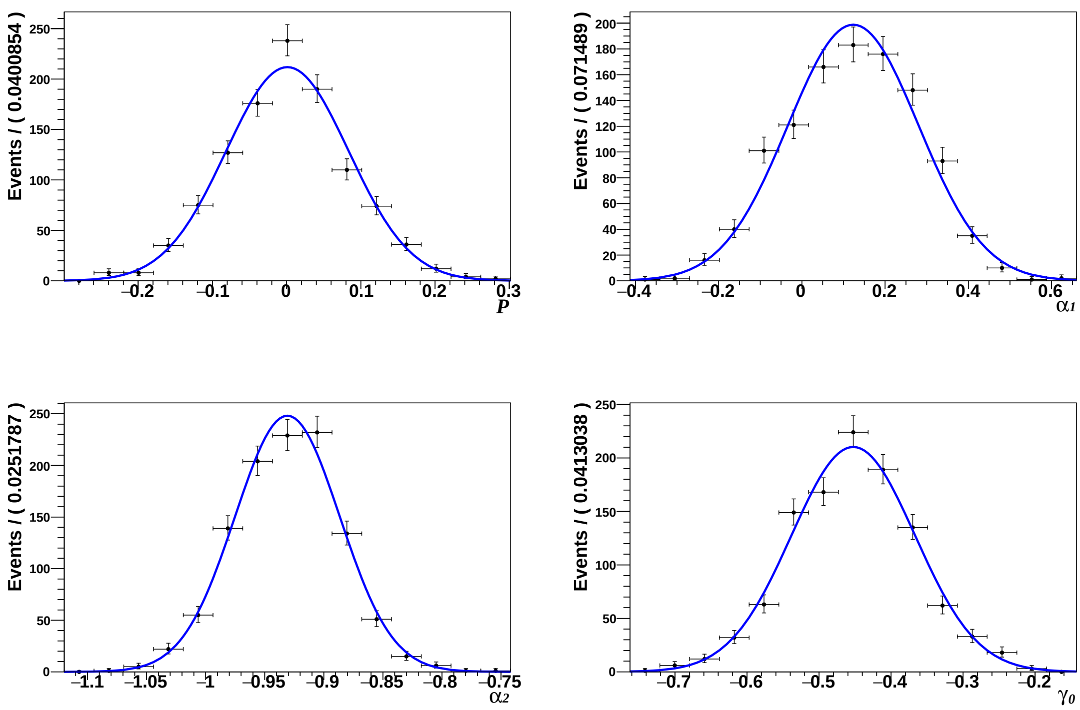

Fig. 5.15 Distributions of the fitted parameters from 1,000 simultaneous likelihood fit to the toy MC test samples.

5.7 Systematic uncertainties

The sources of systematic uncertainties considered are described below.

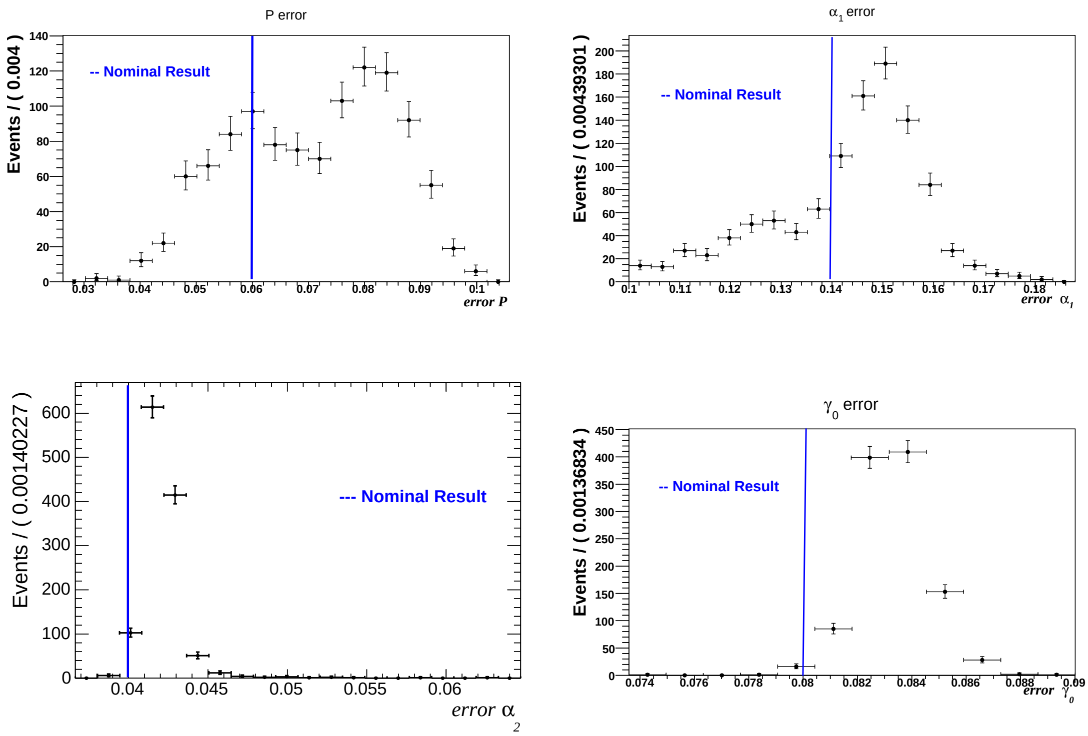

Fig. 5.16 Error distributions from 1,000 simultaneous likelihood fit to the toy MC test samples.

Fit bias The bias introduced by the fitting procedure is studied by generating 1000 pseudo-experiments using the measured parameters as inputs. The difference between the input and the mean of the fitted values is taken as the systematic uncertainty.

Asymmetry parameter α_Λ This parameter is varied up and down by its uncertainty and the maximum deviation in the final result for each parameter is taken as the systematic uncertainty.

Model for the background $m_{J/\psi\Lambda}$ distribution An exponential function is used instead of the first-order polynomial in the likelihood fit. The parameter of the exponential and the background yield are varied by their uncertainties. The fit is redone taking into account this variation on the background model for the mass, and the differences between these results and the nominal fit results are taken as the systematic uncertainty for this source.

Model for the background angular distributions Alternative parametrizations of the background angular distributions are used to estimate the systematic uncertainty. For $\cos\theta_\Lambda$

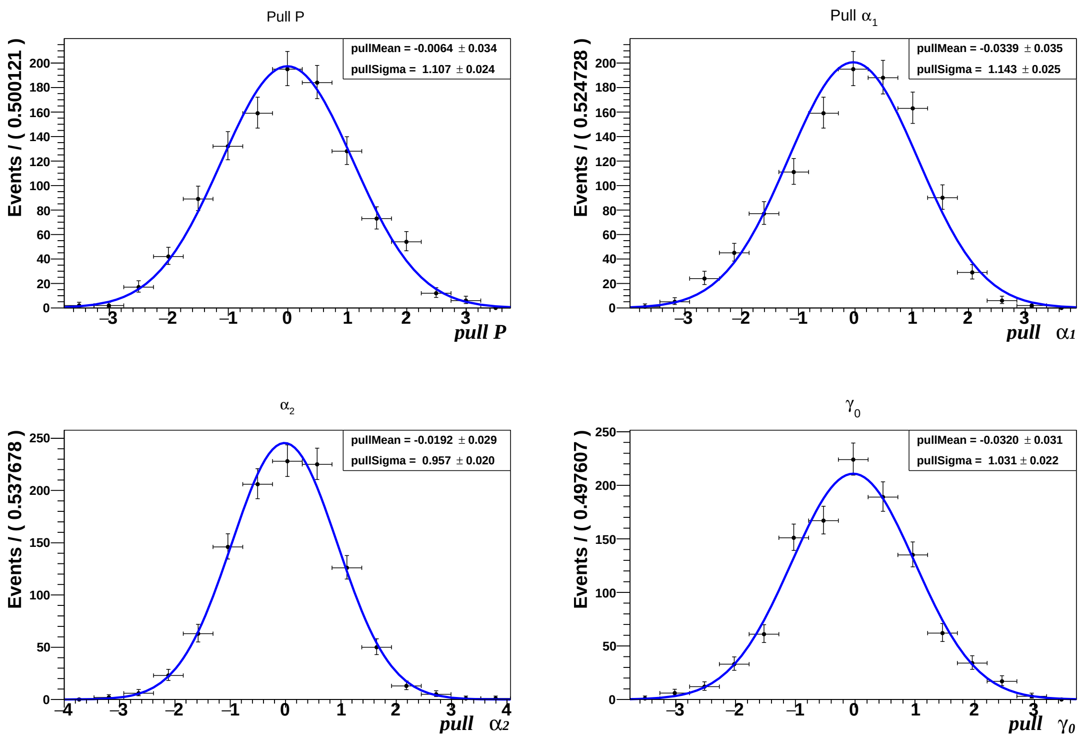

Fig. 5.17 Pull distributions from 1,000 simultaneous likelihood fit to the toy MC test samples.

and $\cos\theta_\mu$ the alternative models comprise a superposition of Gaussian kernels, as implemented in Roofit RooKeysPdf [106], while for $\cos\theta_p$ the alternative model is an error function. The differences relative to the nominal results are taken as the systematic uncertainties from the modeling of the background angular distributions.

Model for the signal $m_{J/\psi\Lambda}$ distribution The uncertainty is estimated varying the parameters within their uncertainties and taking into account their correlations. In each sample, Λ_b and $\overline{\Lambda}_b$ at $\sqrt{s} = 7$ and 8 TeV, the parameters of the signal mass model are added 1 SD to their nominal value if the correlation with the parameter having the largest global correlation is positive or subtracted 1 SD if the correlation is negative. Simultaneously, the parameter with the largest correlation is varied within 1 SD. The difference relative to the nominal result is quoted as a systematic uncertainty.

Angular efficiencies The values of the Chebyshev polynomial coefficients that model the angular dependence of the efficiencies are varied within their uncertainties. The difference relative to the nominal result is taken as the systematic uncertainty.

Angular resolution We study the systematic uncertainty in the angular resolution of the measured observables $\cos\theta_\Lambda$, $\cos\theta_p$, and $\cos\theta_\mu$ by first determining the resolution using simulated events, then taking the difference between the generated (before detector simulation) and reconstructed (fully simulated) distributions of the cosines of the three polar angles, and fitting the resulting distributions to Gaussian functions. Using these models, we generate random numbers that are added to the three polar angles of the events at generation. The difference between the obtained parameters from the likelihood fits using the same events, with and without the added random terms, it is quoted as the systematic uncertainty from the angular resolution.

Azimuthal angle efficiency Uniform azimuthal efficiencies are assumed throughout the analysis. Besides simplifying the measurement from a five- to a three-dimensional angular analysis, this assumption also reduces the number of angular parameters from 6 to 3. The effect of the non uniformity in the φ_p and φ_μ efficiencies is investigated from 500 pseudo-experiments generated using the five-dimensional angular distribution, multiplied by the polar and azimuthal efficiencies obtained from the full simulation, and initializing the 3 extra parameters to values away from the physical boundary. The resulting distributions are then fitted to the nominal three-dimensional angular model. Differences in the mean values of P, α_1, α_2, and γ_0 relative to the input values (set to the nominal results) are taken as the systematic uncertainties coming from the non uniformity of the azimuthal efficiencies.

Weighting procedure To estimate the uncertainty from the weighting procedure, each weight its varied within its uncertainty and used as a different weight to correct the efficiencies, then the fit is performed using the modified efficiency term. The differences between the results of this fit and the nominal values are taken as the systematic uncertainty in each parameter.

Reconstruction bias Possible unaccounted reconstruction biases are also considered. To estimate this systematic uncertainty, we use a simulated event sample with input values of the helicity amplitudes and polarization similar to those observed in data. Then, after reconstruction and selection as in data, we fit the simulated events and take the differences between the input and fit values for every angular parameter and polarization. Since we are using the full reconstruction of the simulated events, we subtract in quadrature the systematic sources involved in the fit from those observed differences, and finally take the square root of this subtraction as the estimate of the systematic uncertainty component due to reconstruction bias. This systematic uncertainty is by far the largest uncertainty however, it is still smaller or comparable to the corresponding statistical uncertainty.

The contributions from the different uncertainty sources are assumed to be independent and the total systematic uncertainty is calculated as the quadrature sum of all uncertainties. The values of the systematic uncertainties in each parameter from the individual sources and their quadrature sum are given in Table 5.8.

Table 5.8 The sources and values of the systematic uncertainties in each parameter and the total uncertainty. Each value in the table should be multiplied by 10^{-2} to obtain the corresponding systematic uncertainty.

Source	$P(\times 10^{-2})$	$\alpha_1(\times 10^{-2})$	$\alpha_2(\times 10^{-2})$	$\gamma_0(\times 10^{-2})$
Fit bias	0.1	0.3	0.1	0.2
Asymmetry parameter α_Λ	0.4	0.7	2.0	0.6
Bkg. $m_{J/\psi\Lambda}$ dist.	0.01	0.5	1.0	0.9
Bkg. angular dist.	0.4	0.5	0.9	5.0
Sig. $m_{J/\psi\Lambda}$ dist.	0.01	0.3	1.0	1.0
Angular efficiencies	0.1	0.3	3.0	1.0
Angular resolution	1.0	0.1	2.6	0.8
Azimuthal efficiency	0.1	1.0	0.3	0.1
Weighting procedure	0.1	1.3	0.4	2.0
Reconstruction bias	5.7	9.8	2.0	9.1
Total (quadrature sum)	5.8	10.0	5.1	11.1

5.8 Summary

The Λ_b polarization, the parity-violating asymmetry parameter in the Λ_b decay α_1, the Λ longitudinal polarization α_2, and the parameter γ_0 were extracted performing an angular analysis of $\Lambda_b \to J/\psi(\mu^+\mu^-)\Lambda(p\pi)$ decays using data from pp collisions at $\sqrt{s} = 7$ and 8 TeV collected by CMS. The measured values are:

$$\begin{aligned} P &= 0.00 \pm 0.06\,(\text{stat}) \pm 0.06\,(\text{syst}), \\ \alpha_1 &= 0.14 \pm 0.14\,(\text{stat}) \pm 0.10\,(\text{syst}), \\ \alpha_2 &= -1.11 \pm 0.04\,(\text{stat}) \pm 0.05\,(\text{syst}), \\ \gamma_0 &= -0.27 \pm 0.08\,(\text{stat}) \pm 0.11\,(\text{syst}). \end{aligned}$$

Translating the angular parameters into the the helicity amplitudes gives

$$\begin{aligned} |T_{++}|^2 &= \quad 0.05 \pm 0.04\,(\text{stat}) \pm 0.04\,(\text{syst}), \\ |T_{+0}|^2 &= -0.10 \pm 0.04\,(\text{stat}) \pm 0.04\,(\text{syst}), \\ |T_{-0}|^2 &= \quad 0.51 \pm 0.03\,(\text{stat}) \pm 0.04\,(\text{syst}), \\ |T_{--}|^2 &= \quad 0.52 \pm 0.04\,(\text{stat}) \pm 0.04\,(\text{syst}). \end{aligned}$$

The Λ_b polarization value obtained is consistent with the LHCb measurement [49] and with theoretical predictions of 0.10 [2] and 0.20 [3]. Theoretical predictions for $-\alpha_1$ are -0.2 to -0.1 from quark model techniques [55–57, 59, 60], -0.17 to -0.14 from perturbative quantum chromodynamics calculations [58], and 0.78 from heavy-quark effective theory [3, 107]. The measured value is consistent at less than one standard deviation with the theoretical predictions except for the the heavy-quark effective theory one, being inconsistent at more than 5 standard deviations. The presented measurement of α_1 is also consistent with the measurements LHCb [49] and ATLAS [108] mearements of $0.05 \pm 0.17\,(\text{stat}) \pm 0.07\,(\text{syst})$ and $0.30 \pm 0.16\,(\text{stat}) \pm 0.06\,(\text{syst})$, respectively, and with no parity violation at the level of one standard deviation. The measurement of α_2, which is compatible with -1, indicates that the positive-helicity states of the Λ coming from the Λ_b decay are suppressed.

The measured values for the helicity amplitudes are consistent with the values reported by LHCb and ATLAS. Table 5.9 shows the polarization and the helicity amplitudes reported by CMS and the measurements from LHCb and ATLAS along with its corresponding deviation from CMS results

Table 5.9 Values of the helicity amplitudes and Λ_b polarization as measured by CMS and the results from LHCb and ATLAS along with its corresponding difference from CMS value in σ units. For the reported values, the first uncertainty is statistical and the second systematic one.

	CMS	LHCb		ATLAS	
		result	diff. SD	result	diff. SD
$\|T_{++}\|^2$	$0.05 \pm 0.04 \pm 0.04$	$-0.10 \pm 0.04 \pm 0.03$	1.98	$0.01^{+0.02}_{-0.01} \pm 0.01$	0.65
$\|T_{+0}\|^2$	$-0.10 \pm 0.04 \pm 0.04$	$0.01 \pm 0.04 \pm 0.03$	1.45	$0.03^{+0.04}_{-0.06} \pm 0.03$	1.48
$\|T_{-0}\|^2$	$0.51 \pm 0.03 \pm 0.04$	$0.57 \pm 0.06 \pm 0.03$	0.72	$0.35^{+0.07}_{-0.08} \pm 0.04$	1.60
$\|T_{--}\|^2$	$0.52 \pm 0.04 \pm 0.04$	$0.51 \pm 0.05 \pm 0.02$	0.13	$0.62^{+0.06}_{-0.08} \pm 0.02$	1.00
P	$0.00 \pm 0.06 \pm 0.06$	$0.06 \pm 0.07 \pm 0.06$	0.47	$--$	$--$
α_b	$-0.14 \pm 0.14 \pm 0.10$	$0.05 \pm 0.17 \pm 0.07$	0.79	$0.30 \pm 0.16 \pm 0.06$	1.8

Chapter 6

Exclusive J/ψ photoproduction in ultra-peripheral p-Pb collisions.

This chapter describes the analysis on the J/ψ photoproduction cross section measurements performed at CMS using data from pPb collisions at $\sqrt{s_{NN}} = 8.16$ TeV.

6.1 Dataset and triggers

The data used for this analysis were recorded by CMS during the LHC 2016 proton-lead running with a center-of-mass energy per nucleon pair of 8.16 TeV. The LHC proton-lead running period consisted in two parts, in the first part, denoted as pPb, the proton beams were in the negative z direction (clockwise) and the Pb lead in the positive z direction. The integrated luminosity during this first period corresponds to 64 nb^{-1}. For the second part of the running, the directions of the beams were inverted. The recorded integrated luminosity for this second period was 115 nb^{-1}.

Events were selected online with a set of dedicated triggers specially designed to record UPC vector mesons ψ's and Υ's, and $\gamma\gamma \rightarrow \mu\mu$ events. The UPC triggers select low p_{T} muons from UPC collisions by requiring almost no activity in the detector. This is achieved by requiring Hadron Forward (HF) activity in one or both sides to be consistent with noise and/or requiring low track multiplicities. The UPC HLT triggers are listed in table 6.1. The UPC triggers are seeded by the L1_SingleMuOpen and extra requirements on the HF are applied at Hardware level and at software level for the tracker multiplicities.

Table 6.1 UPC triggers in 2016

HLT_PADoubleMuOpen_HFOneTowerVeto_v1
HLT_PADoubleMuOpen_HFOneTowerVeto_SingleTrack_v1
HLT_PADoubleMuOpen_HFOTwoTowerVeto_v1
HLT_PADoubleMuOpen_HFOTwoTowerVetoşingleTrack_v1
HLT_PASingleMuOpen_HFOneTowerVeto_v1
HLT_PASingleMuOpen_HFOneTowerVeto_SingleTrack_v1
HLT_PASingleMuOpen_HFTwoTowerVeto_v1
HLT_PASingleMuOpen_HFTwoTowerVeto_SingleTrack_v1
HLT_PASingleMuOpen_PixelTrackGt0_FullTrackLt10_v1
HLT_PASingleMuOpen_PixelTrackGt0_FullTrackLt15_v1
HLT_PASingleMuOpen_PixelTrackGt0_Lt10_v1
HLT_PASingleMuOpen_PixelTrackGt0_Lt15_v1

6.2 Event reconstruction and selection.

The J/ψ candidates are reconstructed in their dimuon decay channel. Muon candidates are reconstructed as tracker muons and are required to pass the soft muon ID selection, as defined by the Muon POG [109]:

- Tracker track matched with at least one muon segment (in any station) in both X and Y coordinates ($< 3\sigma$) (TMOneStationTight) and arbitrated.
- Number of tracker layer with hits > 5. This requirement guarantees a good pT measurement, for which some minimal number of measurement points in the tracker is needed. Also suppresses muons from in-flight decays.
- Number of pixel layers > 0, to further suppress muons from in-flight decays.
- High-purity track flag. This requirement rejects tracks of bad quality.
- Loose transverse and longitudinal impact parameter cuts: dxy < 0.3 cm, dz < 20 cm w.r.t. the primary vertex. This requirement implies (loose) compatibility with the PV (or beam spot).

A pair of oppositely charged muons passing the soft Muon selection is then used to construct the dimuon candidate. The HLT_PASingleMuOpen_HFOneTowerVeto_v1 gives the highest yield and at least one muon is required to be matched to it.
With single interactions, the exclusive signal is characterized by the presence of two muons, no additional tracks, and no activity above the noise threshold in the calorimeters. The selection requires a valid vertex, reconstructed using an adaptive vertex fit to charged-particle

tracks with exactly two muons and no other associated tracks, and vertex fit probability greater than 0.1. The HF cell with the largest energy deposit is required to have an energy below 11 GeV. This requirement, which is determined studying events triggered on non-colliding bunches, ensures that the HF energy is consistent with the presence of photon-induced processes which leave very low signal in both the HF+ and HF- detectors.

HF Exclusivity cut. Events with only two muons should be consistent with noise level energy distributions in the HF calorimeter. To obtain the exclusivity HF cuts, events with not interacting bunches were analyzed. The distribution of the HF leading energy cell, maxCaloTower, per event for both sides HF+ and HF+- was obtained for the next two possible cases: only proton bunches present and only ions present. The analysis was separately performed for the Pbp and pPb beam configurations. The HF thresholds are defined in the way that the cut on the maxCaloTower contains the 99% of the events in this noise distributions. The HF thresholds for both sides of the HF were set to 11 GeV. The distributions of the HF maxCaloTower are shown in Fig. 6.1 for both beam configurations: pPb and Pbp.

Data after selection. The CMS convention is to consider that the proton beam has positive rapidity, so after all selection and exclusivity cuts were applied, the data corresponding to the pPb and Pbp beam configuration were merged with the pPb data flipped in rapidity. The dimuon p_{T} vs. invariant mass and p_{T} vs. rapidity are shown in Fig. 6.2. Structures are clearly observed around the J/ψ and ψ' masses. Most events correspond to low momentum dimuons, p_{T} below 1 GeV. Two-photon produced dimuons in the invariant mass range (4.0 $< M_{\mu^+\mu^-} <$ 8 GeV) have even lower momentum. From the p_{T} vs rapidity distribution is observed that almost all events are concentrated around 2 and -2 in dimuon rapidity.
The dimuon invariant mass distribution is fitted in the range ($2.2 < M_{\mu^+\mu^-} < 4.5$ GeV) using a model composed of a Crystal Ball function to describe the J/ψ mass peak, a single Gaussian for the ψ' mass peak and an exponential to model the non-resonant dimuon continuum. The width of the ψ' Gaussian is constrained to the J/ψ CB width scaled by the ratio between the J/ψ and ψ' BR to muons. The RooFit package was used to construct the mass model and to perform an extended unbinned likelihood fit to the mass distribution. Around 15000 J/ψ and 500 ψ' events are obtained. Table 6.2 summarizes the results from the fit. Based on this fit, the J/ψ mass window was defined as $2.8 < M(\mu^+\mu^-) < 3.3$. The efficiency of this cut is found to be 99.75%.

To further investigate the kinematics of the selected J/ψ the distributions of the dimuon p_{T} and rapidity are shown in Fig. 6.4 for events in the J/ψ mass window with tighter cuts on

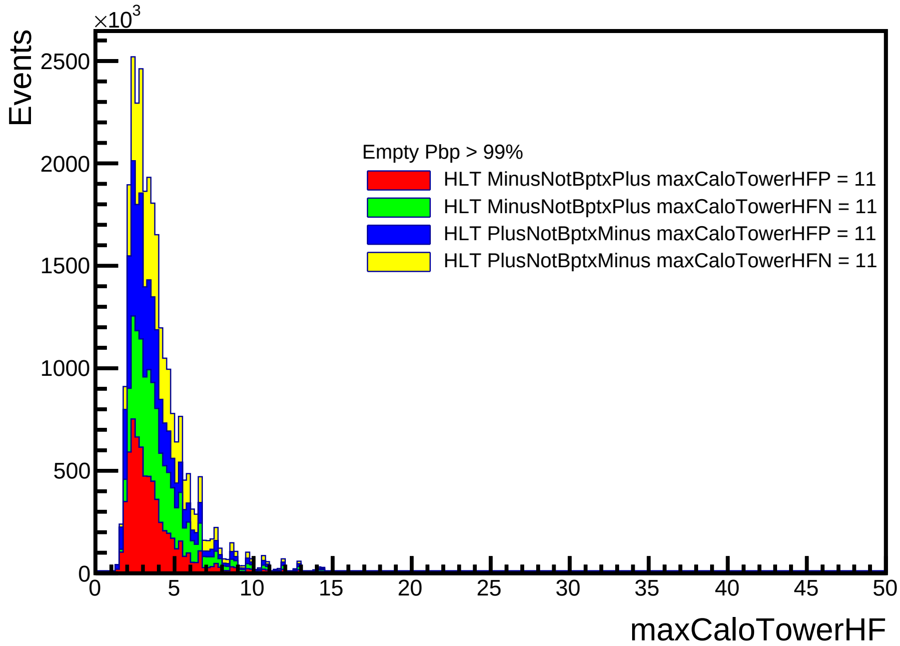

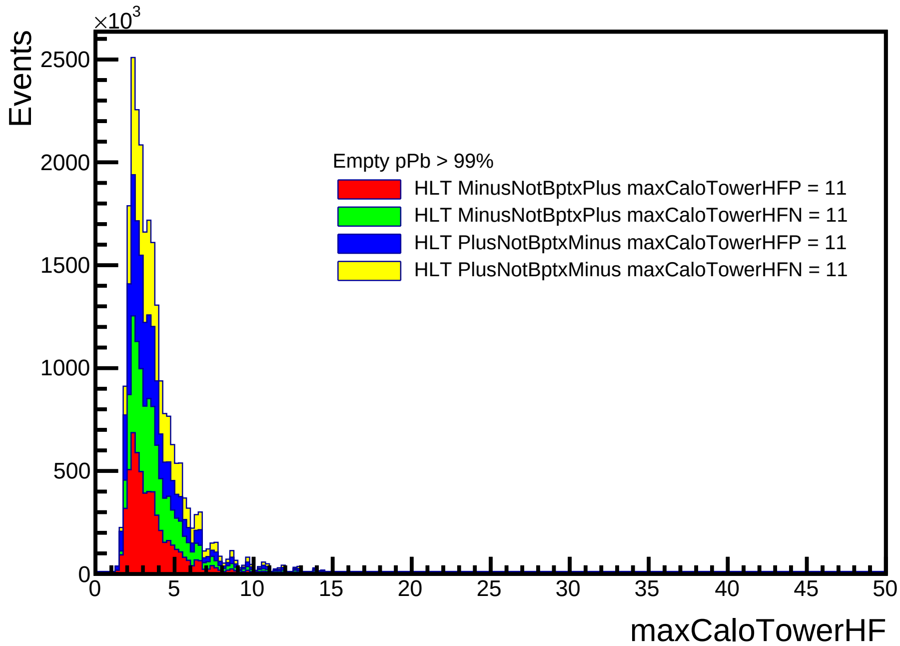

Fig. 6.1 Maximum energy deposits in HF.

the HF max calo tower energies to reduce the contamination from non-exclusive processes, and requiring $p_{\mathrm{T}} > 0.1$ to minimize contributions from the pure qed $\gamma\gamma \to \mu^+\mu^-$ process. Events are concentrated at $p_{\mathrm{T}} = 0.5$ GeV and around |y|∼2. The rapidity distribution is asymmetric with higher number of events in the proton going side since the momentum of the photon emitted by the lead nucleus is usually smaller than that of the parton that the photon interacts with. Fig. 6.5 shows the p_{T} vs η distribution for the muons forming the dimuon system. The muons are forward with $|\eta| > 2.0$.

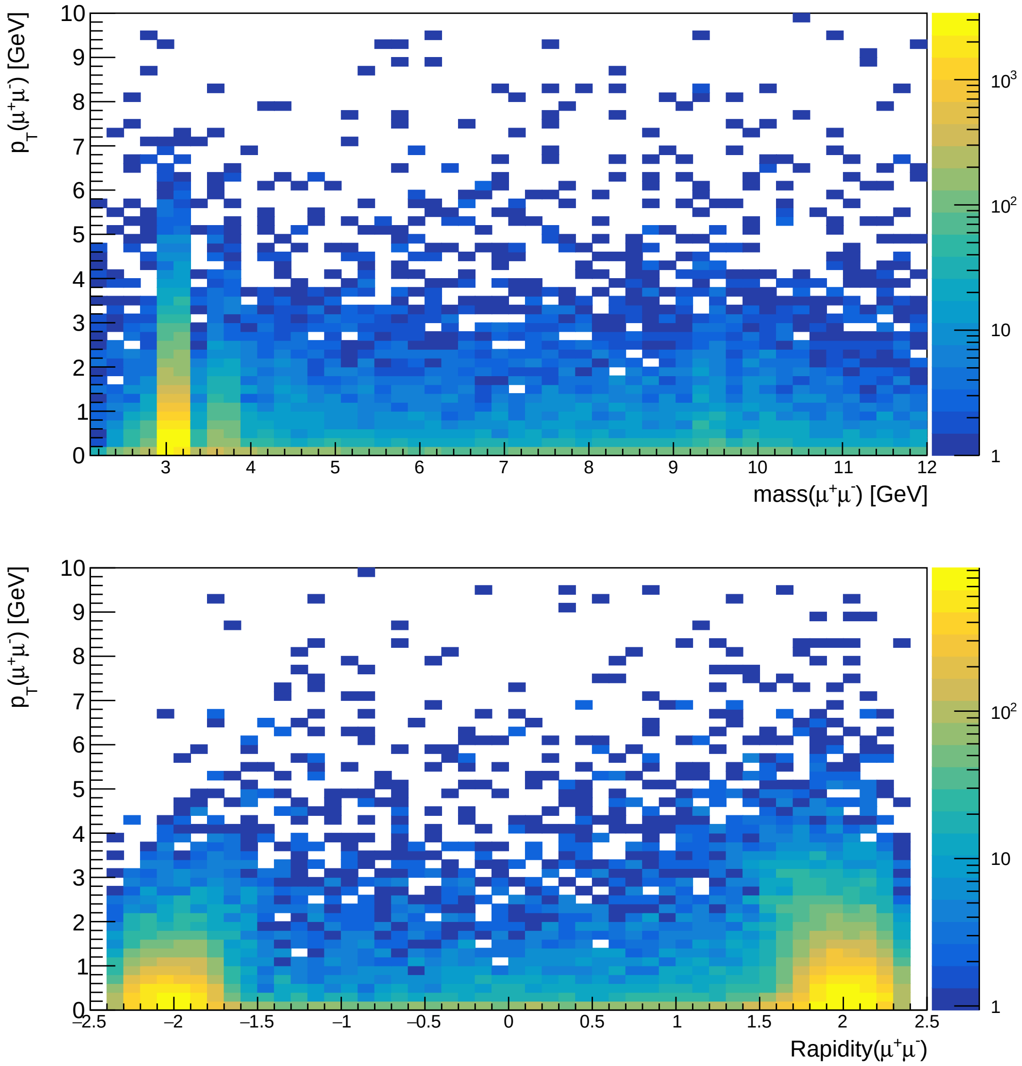

Fig. 6.2 Top:distribution of p_{T} versus invariant mass for dimuon pairs. Bottom: distribution of p_{T} versus laboratory rapidity for dimuon pairs in the invariant mass range ($M(\mu^+\mu^-) <$ 12.0 GeV). All events passing the event selection and exclusivity cuts. The rapidity of the pPb events has been flipped to be consistent with the CMS convention.

Table 6.2 UPC dimuon invariant mass fit results.

paremater	fit result
$N_{J/\psi}$	14993 ± 127
$N_{\psi'}$	518 ± 119
N_{QED}	5722 ± 371
$\mu_{J/\psi}$ (GeV)	3.092 ± 0.001
$\sigma_{J/\psi}$ (GeV)	0.0514 ± 0.0004
α_{CB}	1.49 ± 0.04
n_{CB}	9.4 ± 1.3
$\mu_{\psi'}$ (GeV)	3.678 ± 0.004

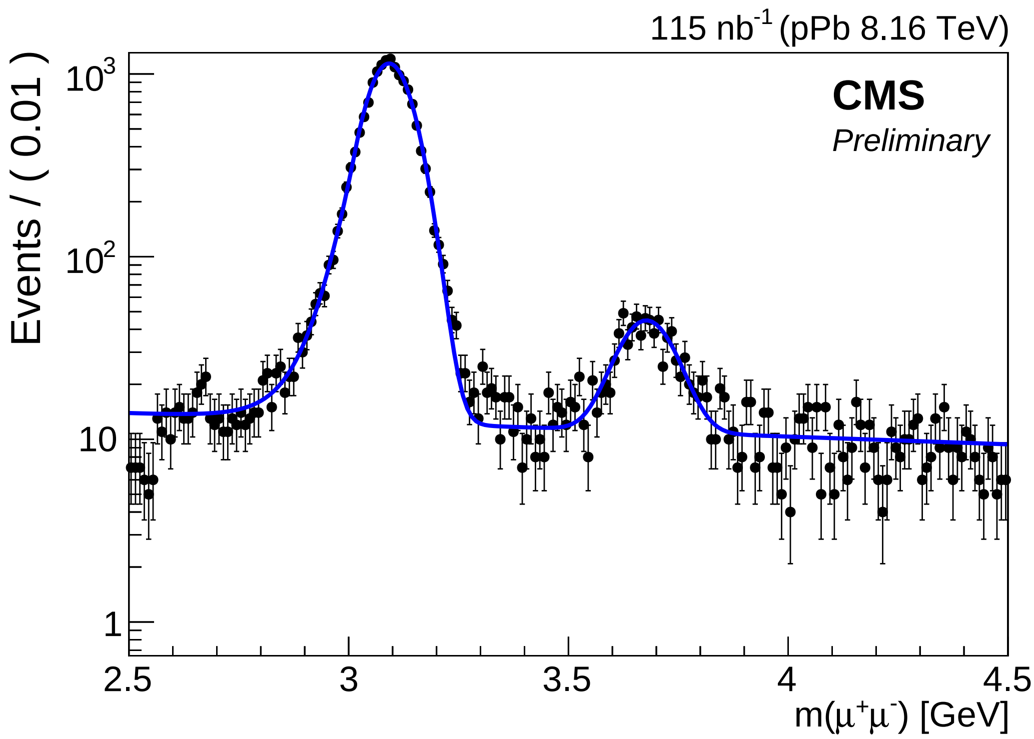

Fig. 6.3 Fit to the dimuon invariant mass fit after applying the selection and exclusivity cuts.

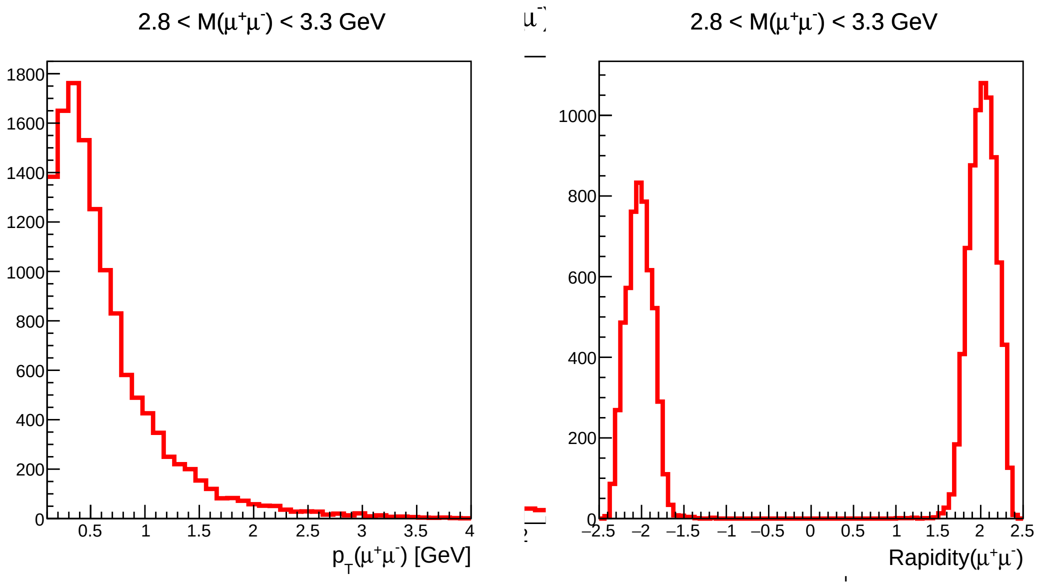

Fig. 6.4 Dimuon p_T (left) and rapidity (right) distributions applying tighter cuts on HF and requiring $p_T > 0.1$

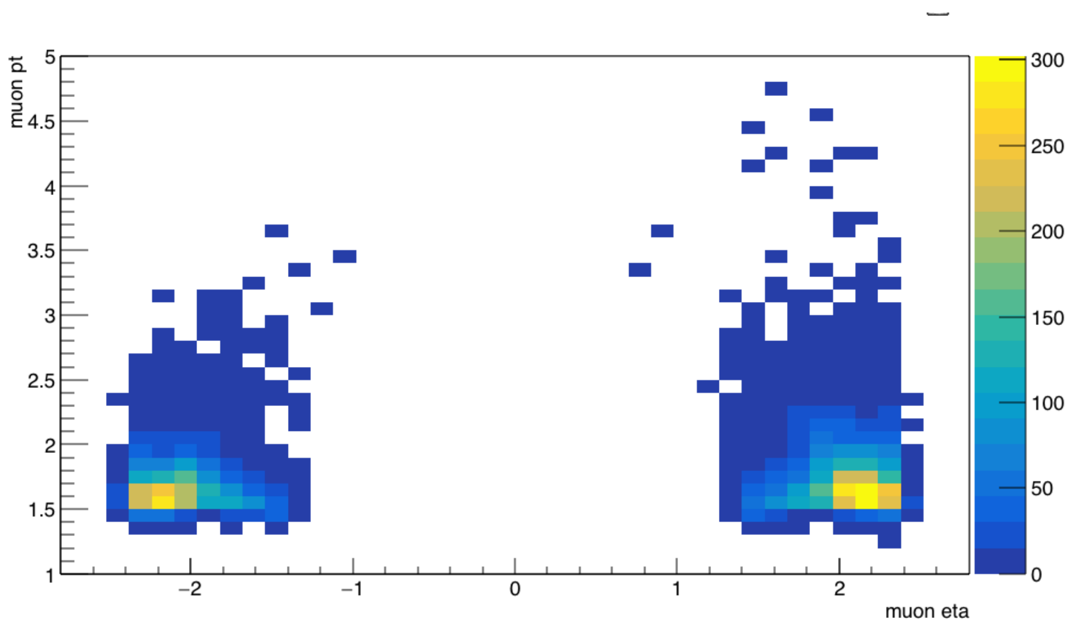

Fig. 6.5 Muon p_T vs rapidity distributions.

6.3 Monte Carlo samples

In order to compute acceptance and efficiency corrections and for the signal extraction procedure, Monte Carlo (MC) samples for exclusive J/ψ and $\gamma\gamma$ events in the dimuon decay channel are generated using the starlight MC event generator [110, 111]. These events are processed with the full CMS simulation and reconstruction software[112].

The STARLIGHT generator models two-photon and photon–hadron interactions at ultra-relativistic energies. STARLIGTH exclusive vector meson cross sections are based on parametrized HERA data for $\gamma p \to Vp$. The ψ and Υ cross sections, $\sigma(\gamma p \to Vp)$, are parametrized as a function of the $W_{\gamma\text{p}}$ center-of-mass energy as:

$$\sigma(\gamma + p \to V + p) = \sigma_p \cdot \left| 1 - \frac{(m_p + m_V)^2}{W_{\gamma p}^2} \right|^2 W_{\gamma p}^{\varepsilon}, \tag{6.1}$$

where σ_P is the Pomeron exchange cross sections. The values for σ_P and ε are obtained from experimental data; for J/ψ, σ_P = 4.06 nb and ε = 0.65. In STARLIGHT the distribution of the transverse momentum p_T of the J/ψ in photon-proton has the functional form

$$\frac{dN}{dp_\text{T}} = A \cdot p_\text{T} \cdot \exp\left\{-b \cdot p_\text{T}^2\right\}. \tag{6.2}$$

In Eq. 6.2 A is a normalization constant and, according to measurements performed at HERA, the exponential parameter b is a function of $W_{\gamma\text{p}}$:

$$b\left(W_{\gamma\text{p}}\right) = b_0 + 4\alpha' ln\left(\frac{W_{\gamma\text{p}}}{W_0}\right), \tag{6.3}$$

where $b_0 = 4.630$ GeV^{-2}, $\alpha' = 0.164$ and W_0 arbitrarily set to 90 GeV [27]. STARLITGHT has $b = 4.0$ Gev^{-2} as default value in Eq. 6.3 which is tuned for low energies, However, at higher $W_{\gamma\text{p}}$ energies, such as those reached at LHC, the exponential parameter should be tuned. For this reason, the J/ψ p_T was generated according to the $W_{\gamma\text{p}}$ of the associated event, i.e as a function of the J/ψ rapidity.

Two million MC events samples for the exclusive processes $\gamma\gamma \to \mu^+\mu^-$, and $\gamma\gamma \to J/\psi p$, in UPC p-Pb collisions at a center-of-mass energy of 8.16 TeV were generated. The events were generated in the dimuon rapidity interval $|y| < 6$ and for the photon-photon sample it was restricted to the dimuon mass interval $2.0 < m(\mu^+\mu^-) < 5.0$ GeV. No additional fliters on the muon's kinematic variables was applied at generation level. Fig. 6.6 shows the Rapidity and p_T distribution at generation level for exclusive J/ψ and elastic $\gamma\gamma \to \mu^+\mu^-$ events.

At the time the analysis started, the STARLIGHT event generator was not implemented in CMSSW and thus samples were produced privately. The production sequence consisted in the following steps. Firstly, the output from the generator was converted to the Les Houches Event (LHE) format, which is the standard format for CMS MC production sequence. These LHE files serve as input for the simulation and digitization steps whereby the generated particles are run through a detailed, Geant4-based simulation of the CMS detector, and detector electronics response is modeled. Finally, the trigger emulation and the standard CMS reconstruction algorithms are run to get samples actually comparable with data. Once the MC production is completed, the samples are passed through the same offline reconstruction and selection algorithm used in real data. The rapidity and p_{T} distribution for the reco-selected MC samples are displayed in Fig 6.7.

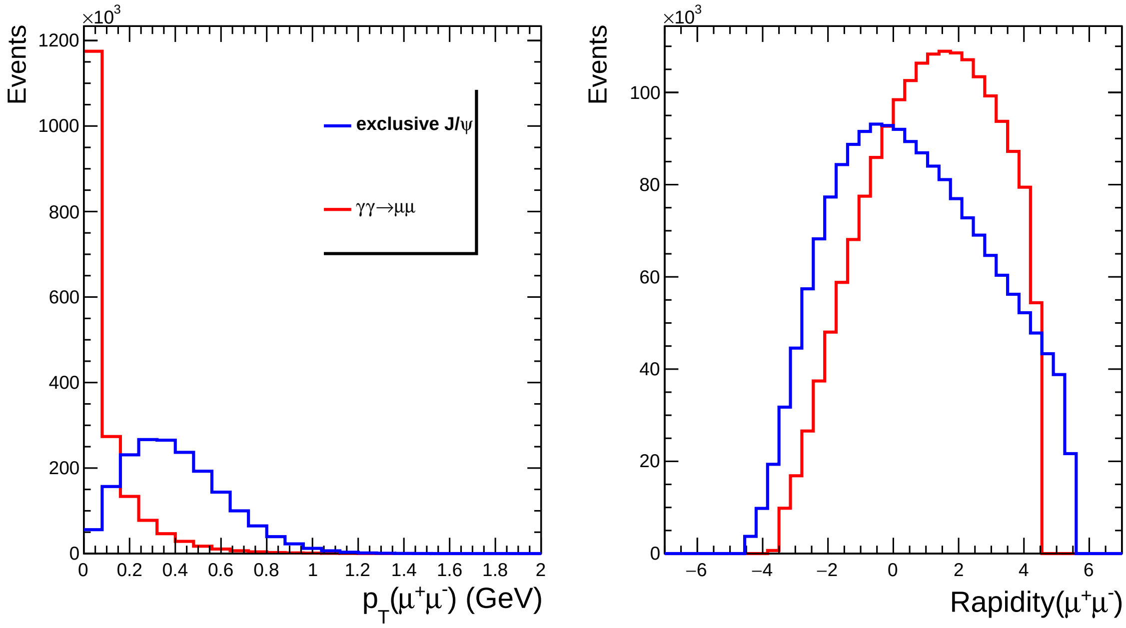

Fig. 6.6 Exclusive J/ψ (blue) and $\gamma\gamma \to \mu^+\mu^-$ (red) MC p_{T} (left) and rapidity (right) distributions at generation level.

6.4 Cross section calculation

The cross-section $\sigma(p+Pb \to p+Pb+J/\psi)$ is measured deferentially in four equally spaced bins of J/ψ rapidity in the ranges $y \in (-2.4,-2.0)$and $y \in (2.0,2.4)$. The selection of the bins is motivated by the trigger efficiency studies described in section 6.6. The measurements are restricted to the fiducial region where both muons have pseudorapidities

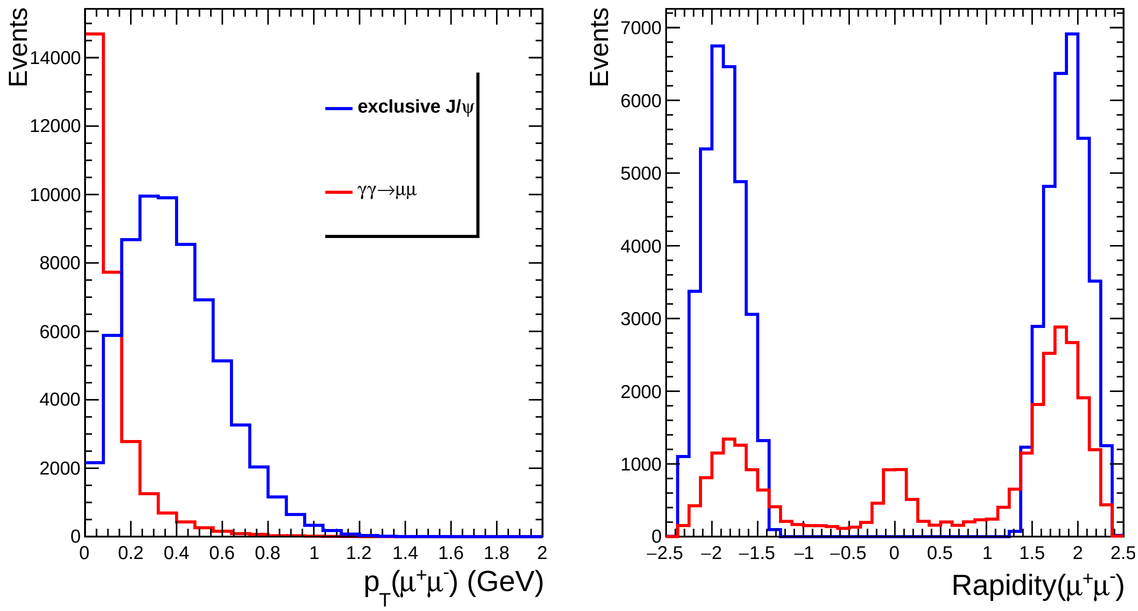

Fig. 6.7 Exclusive J/ψ (blue) and $\gamma\gamma \rightarrow \mu^+\mu^-$ (red) MC p_{T} (left) and rapidity (right) distributions at reconstruction level.

between -2.4 and 2.4, i.e. within the CMS acceptance. The differential cross-section in each bin is given by

$$\frac{d\sigma}{dy} = \frac{N}{BR\,(J/\psi \rightarrow \mu^+\mu^-)\,(A \times \varepsilon) \cdot \varepsilon_{trg}^{\mu^+\mu^-} \cdot \Delta y \cdot \mathscr{L}}, \tag{6.4}$$

In Eq. 6.4, N is the number of extracted exclusive J/ψ's from data. $(A \times \varepsilon)$ denotes the product of the detector acceptance and reconstruction efficiency, obtained from simulations. $\varepsilon_{trg}^{\mu^+\mu^-}$ is the dimuon trigger efficiency. Δy is the width of the rapidity bin, $\mathscr{L}$ the total integrated luminosity, and BR($J/\psi \rightarrow \mu^+\mu^-$) is the Branching ratio of J/ψ decaying to muons, the value is extracted from PDG [113] and corresponds to 5.971%

Details on the extraction of the quantities needed for the cross section calculations, Eq. 6.4 are given below.

6.5 Signal extraction.

The invariant mass distribution of the selected events for a given rapidity bin are shown in Fig. 6.8. Although the selection and exclusivity cuts described in 6.2 aim to obtain the cleanest possible sample of exclusive J/ψ's, other physics processes such as $\gamma\gamma \rightarrow \mu^+\mu^-$ (either elastic or proton dissociative), non-exclusive J/ψ where the proton dissociates but the remnants remain undetected, feed-down of $\psi(2S)$ to J/ψ, and coherent J/ψ from γPb interactions can contribute to the events in the J/ψ mass window. All of the above mentioned processes distributes in different ways to the distribution of transverse momentum of dimuon pairs. The pure QED $\gamma\gamma \to \mu^+\mu^-$ process contributes at low values of p_{T} whereas non-exclusive backgrounds do at higher p_{T} [114]. These differences in p_{T} distributions from the different processes are exploited to determine the number of exclusive J/ψ from data by means of a fit to the data p_{T} distribution with templates from exclusive J/ψ, $\gamma\gamma \to \mu^+\mu^-$ and non-exclusive background. The templates for exclusive J/ψ and exclusive $\gamma\gamma \to \mu^+\mu^-$ are built from the produced MC samples. As mentioned in section 6.3, the MC samples are folded with the detector reconstruction and offline selection effects. The template for the non-exclusive background is obtained from data by inverting the requirement on the HF maxCaloTower energies while keeping all other cuts the same.

A binned maximum likelihood fit to the p_{T} distribution is performed using the templates described above. The relative normalization of the exclusive J/ψ and the non-exclusive background in the template fits are left free, only the contribution from the $\gamma\gamma \to \mu^+\mu^-$ process is constrained to the information obtained from the fit to the invariant mass distributions Fig. 6.8 where the J/ψ is modeled with a Crystall Ball function and the non-resonant dimuon background with an exponential. Upper bounds to the $\gamma\gamma \to \mu^+\mu^-$ background contribution are estimated from the value of the integral of the background PDF in the J/ψ mass window $2.8 < M(\mu^+\mu^-) < 3.3$ GeV. The results from the fits to the p_{T} distributions are shown in Fig 6.9 for the different rapidity bins used in this analysis.

6.6 Acceptance and Efficiency correction.

The number of signal events need to be corrected to account for the geometrical detector acceptance and the offline reconstruction efficiency. The product of acceptance and reconstruction efficiency is obtained using simulated events generated using STARLIGHT, and it is defined as:

$$A \times \varepsilon = \frac{N_{reco}^{J/\psi}(-2.4 < \eta^{\mu} < 2.4)}{N_{gen}^{J/\psi}}, \tag{6.5}$$

where N_{reco} is the number of reconstructed events which pass the kinematic selections described in 6.2 and N_{gen} is the total generated events in a given rapidity range.

In addition, the muon identification and trigger efficiencies are evaluated individually from data using a "tag and probe" technique to muons from J/ψ decays [115]. This technique uses events with strict selection requirements on one muon (the "tag" muon) and with a more relaxed selection on the other muon (the "probe" muon), such that the selection applied to

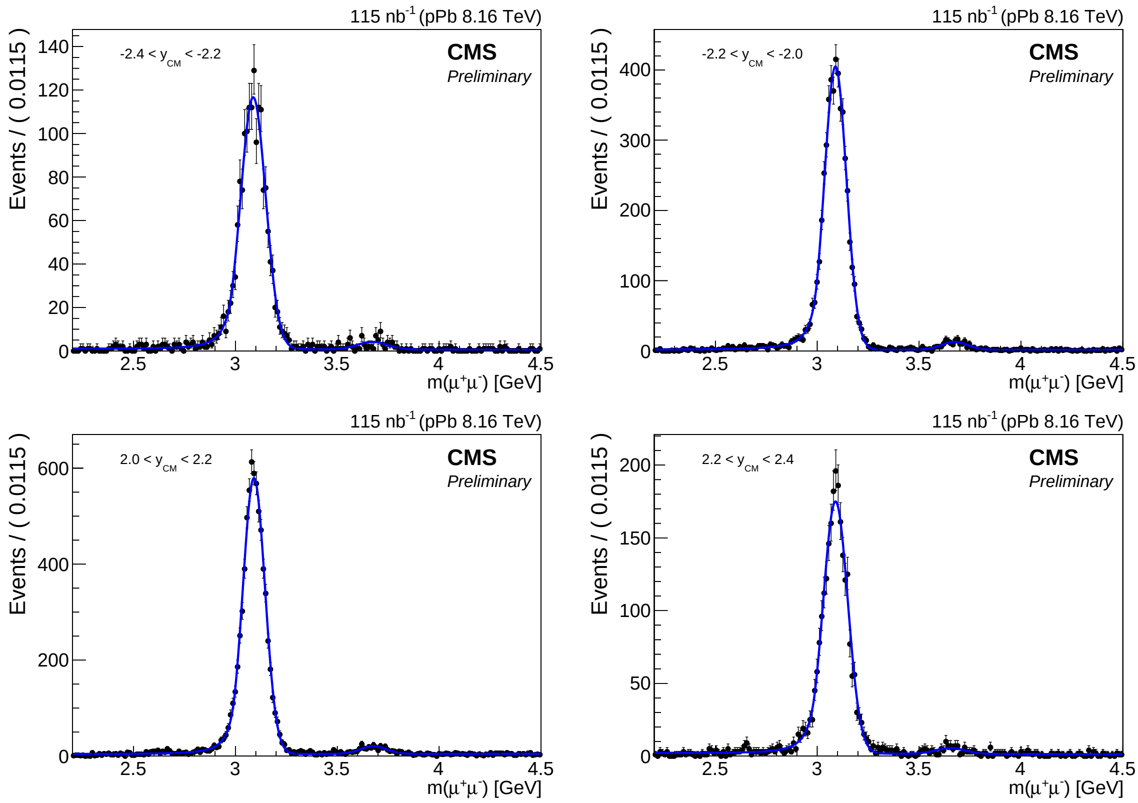

Fig. 6.8 Fit to the dimuon invariant mass distributions for the rapidity bin used in the analysis. The solid line indicates the performed fit to the data, where a CB function is used to describe the J/ψ peak, a single Gaussian for the ψ' peak modelling, and an exponential to describe the dimuon continuum background.

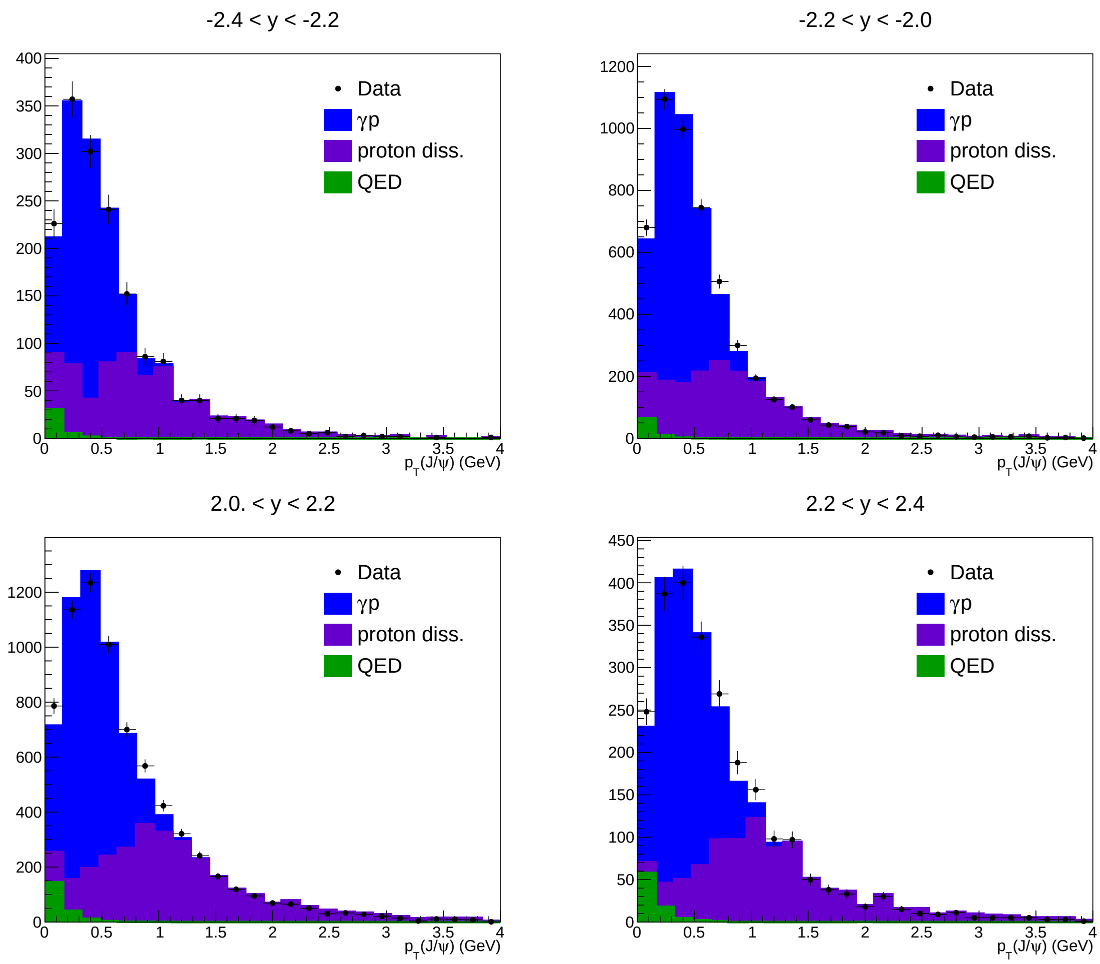

Fig. 6.9 Fit to the J/ψ p_T distributions in different rapidity bins: (top-left) $-2.4 < y < -2.2$, (top-right) $-2.2 < y < -2.0$, (bottom-left) $2.0 < y < 2.2$ and (bottom-right) $2.2 < y < 2.4$.

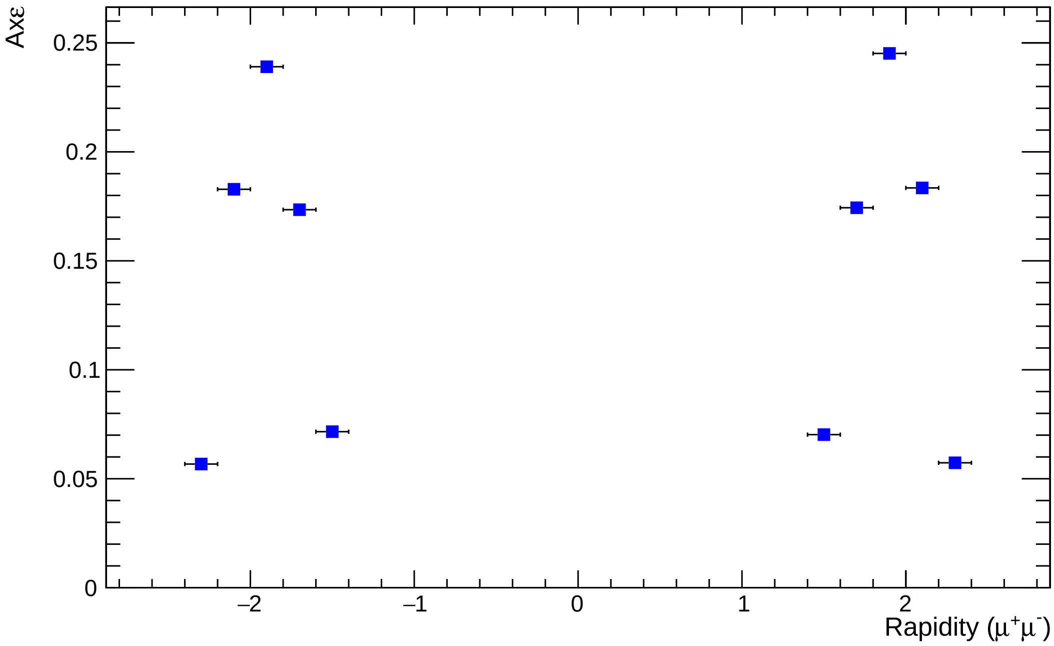

Fig. 6.10 Exclusive J/ψ acceptance as function of rapidity.

the probe muon does not bias the efficiency to be measured. The fraction of probe muons that passes the selection ("passing probes") under study gives an estimate of its efficiency. The dimuon trigger efficiency is obtained from the single muon efficiencies, as discussed later in this section.

Pairs of tag and probe muons are combined to construct a dimuon candidate and a fit to the dimuon invariant mass distribution in the extended invariant mass range from 2.6 GeV to 3.5 GeV is applied. The ratio between the number of "passing" J/ψ's and the total number of J/ψ's gives us the efficiency. The invariant mass model used for the fit uses a Voigtian function (a convolution of a Breit-Wigner with a Gaussian) to describe the J/ψ peak and an exponential to describe the background. The efficiencies were evaluated separately for the pPb and Pbp datasets.

To evaluate the muon identification efficiency, a tag muon is defined as a tracker muon satisfying the soft muon id selection criteria (section 6.2), probes are tracker muons. For the single muon trigger efficiency evaluation, tag muons are defined as soft muons which are matched to the HLT_PA_SingleMuOpen_HFOneTowerVeto_v1, while probes are soft Id tracker muons. The definition of the tag and probe muons used to evaluate the muon identification and single muon trigger efficiencies are summarized in Table 6.3.

Evaluations of the muon identification and single muon trigger efficiencies are shown in Fig. 6.11 and Fig. 6.12, respectively. The efficiencies are shown as a function of muon p_{T} and η and for the two beam configurations. Results are consistent for the two periods of data taking. No strong dependence in the muon p_{T} and η is observed for the muon identification efficiency. The efficiency is 99% for $|\eta_{\mu}| > 1.8$. The individual muon trigger efficiencies are calculated on a grid according to its p_{T} and η.

Table 6.3 Definitions TnP

	muonId	trigger
Tag	softId	softId + HLT matched
Probe	tracker muon	softId
Passing Probe	softId	HLT matched

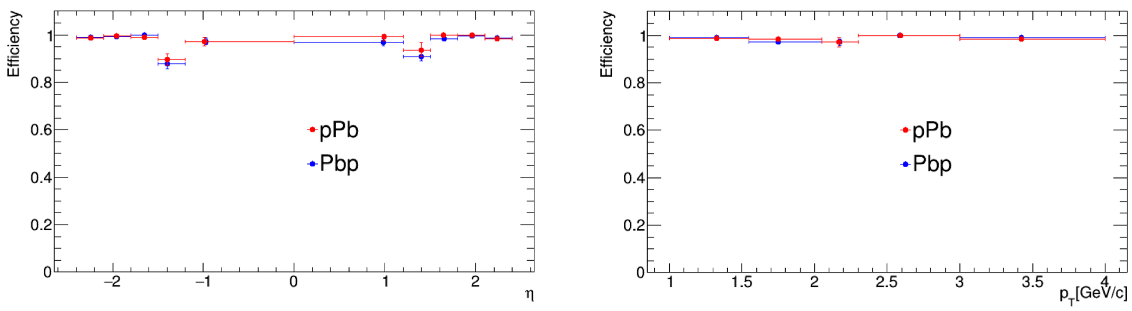

Fig. 6.11 Muon identification efficiency as a function of η and p_{T} for pPb and Pbp beam configuration.

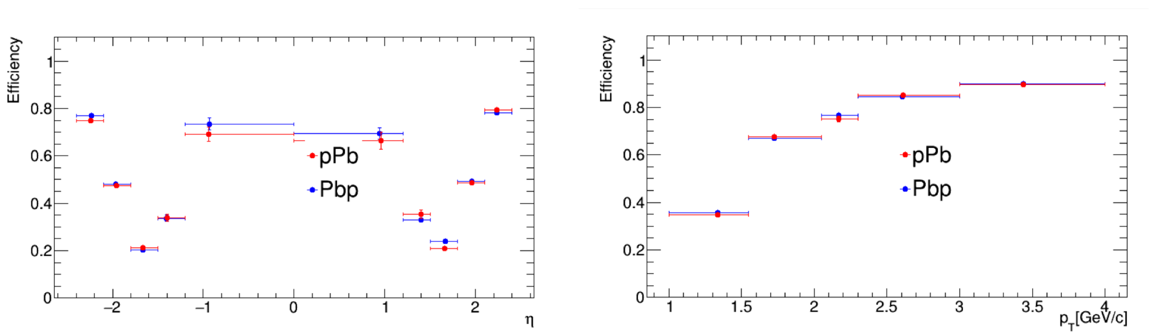

Fig. 6.12 Single muon trigger efficiency as a function of η and p_{T} for pPb (red) and Pbp (blue) beam configuration.

Dimuon trigger efficiency For ultra-peripheral J/ψ events the occupancy of the muon chambers is very low and the two muons are always in different ϕ regions of the muon chambers. In such conditions, trigger efficiencies for each muon are independent and the chance for a J/ψ not to fire the trigger is just the product of the probabilities that muon1 and muon2 both fail the trigger. The dimuon trigger efficiency $\varepsilon_{trg}^{\mu\mu}$ is thus given by:

$$\varepsilon_{trg}^{\mu\mu} = 1 - \left(1 - \varepsilon_{trg}^{\mu_1}(p_{\mathrm{T}}, \eta)\right)\left(1 - \varepsilon_{trg}^{\mu_2}(p_{\mathrm{T}}, \eta)\right), \tag{6.6}$$

where $\varepsilon_{trg}^{\mu_1}$ is the trigger efficiency of μ_1 as function of its p_{T} and η, and $\varepsilon_{trg}^{\mu_2}$ is the second muon trigger efficiency. The dimuon trigger efficiency is calculated on an event-by-event basis. The individual muon efficiencies are calculated on a grid as shown in Fig. The total correction factor for efficiency is obtained by averaging the individual dimuon efficiency over all the events in a particular rapidity range, as shown in Fig 6.13.

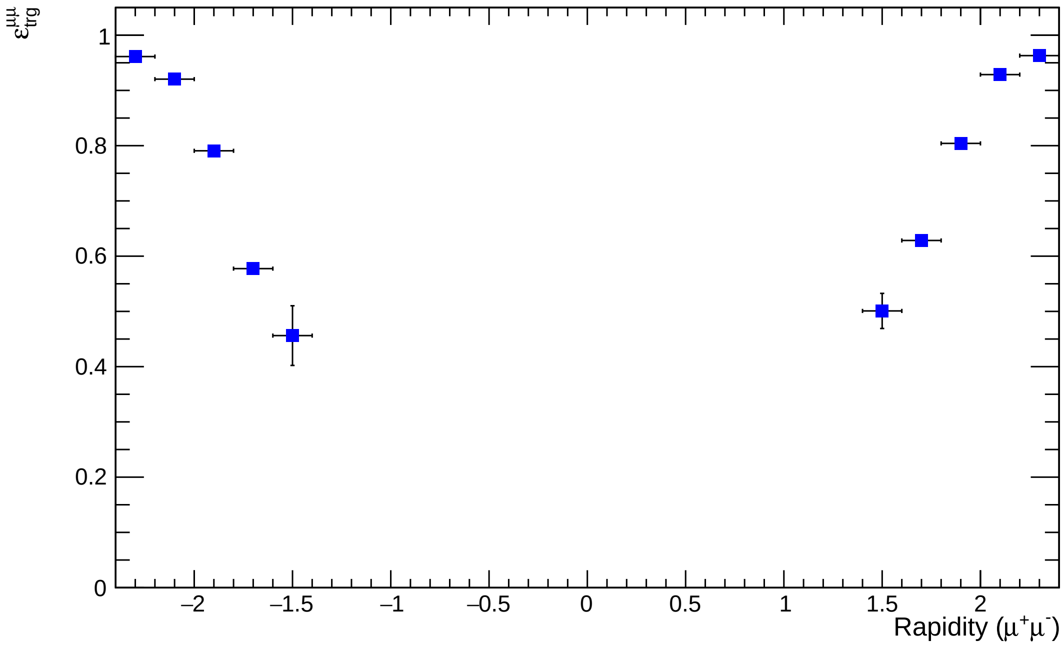

Fig. 6.13 Average dimuon trigger efficiency as a function of rapidity.

6.7 Results

The measured differential cross-sections are given in Table 6.4 as function of the J/ψ meson rapidity bin. The table also displays the numbers of the quantities entering the cross section calculation.

Table 6.4 Differential cross sections

y bin	(2.0, 2.4)	(2.0, 2.2)	(2.2, 2.4)	(-2.2, -2.0)	(-2.4, -2.2)	(-2.4, -2.2)
N	5295	3960	1384	3416	1017	4316
Stat. Uncert. (%)	2.5	2.9	4.7	2.5	4.9	2.3
$(A \times \varepsilon)$	0.121	0.183	0.057	0.183	0.057	0.122
Stat. Uncert. (%)	1.0	1.1	1.7	1.0	1.6	1.0
$\varepsilon_{trg}^{\mu\mu}$	0.94	0.93	0.96	0.92	0.96	0.93
Stat. Uncert. (%)	7.4	7.5	3.1	8.7	4.2	7.5
$\frac{d\sigma}{dy}$ (μb)	10.96	10.86	11.71	9.48	8.71	9.07
Stat. Uncert. (%)	7.7	8.5	6.2	8.7	6.4	7.9
Lumi. Uncert. (%) [116]	3.5	3.5	3.5	3.5	3.5	3.5

Summing these differential results we compute the cross-sections for the negative and positive lab frame rapidities:

$$\sigma_{J/\psi}(2.0 < |y| < 2.4) = 8.2 \pm 0.3 \pm 0.1 \mu b$$

The first uncertainty is statistical, and the second is due to the luminosity determination.

The relation between the differential cross section, $d\sigma/dy$ and the total photoproduction cross section, $\sigma(\gamma + p \to J/\psi + p)$, is given by

$$\frac{d\sigma}{dy} = k\frac{dn}{dk}\sigma(\gamma + p \to J/\psi + p), \tag{6.7}$$

where $k = (1/2)M_{J/\psi}\exp\{-y\}$ is the photon energy in the laboratory frame and $k\frac{dn}{dk}$ the flux of photons with energy k emitted by the lead nucleus. The photon flux is computed using STARLIGHT. The measured photo-production cross sections are given in Table 6.5, along with the value of the centre-of-mass energy of the photon-proton system, $W_{\gamma p}$, which has been computed as the average of $W_{\gamma p}$ over the rapidity interval weighted with the product of the photo-production cross section and photon flux predicted by STARLIGHT.

Table 6.5 J/ψ photo-production cross sections.

y bin	(2.0, 2.4)	(2.0, 2.2)	(2.2, 2.4)	(-2.2, -2.0)	(-2.4, -2.2)	(-2.4, -2.0)
$<W_{\gamma p}>$	67	63	70	573	633	602
$k\frac{dn}{dk}$	175.5	172.4	178.7	42.7	37.1	39.9
$\sigma_{\gamma p \to J/\psi p}$(nb)	62	63	65	222	235	228
Stat. Uncert. (%)	8.1	8.5	6.2	8.7	6.4	7.9
Lumi. Uncert. (%)	3.5	3.5	3.5	3.5	3.5	3.5

The measured photoproduction cross-sections for J/ψ are shown in Fig. 6.14. CMS results are compared with extrapolations from a power law fit to H1 data. H1 parametrizes their data as $\sigma_{\gamma p \to J/\psi p} = a(W/90)^{\delta}$ with a $= 81 \pm 3$ pb and $\delta = 0.67 \pm 0.03$. Fitting CMS data with a power law gives: $\delta = 0.58 \pm 0.04$, still consistent with H1 result.

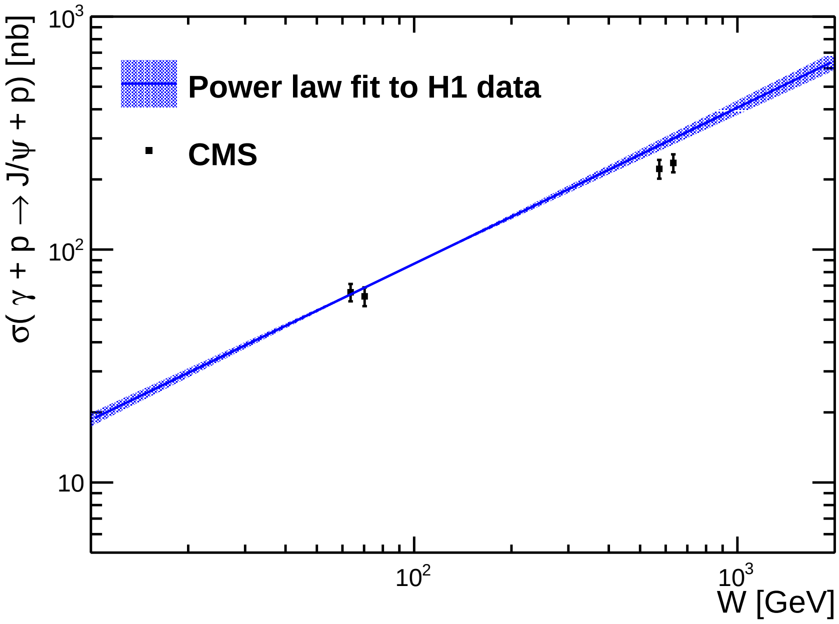

Fig. 6.14 The J/ψ photoproduction cross section measured by CMS is compared to the H1 parametrization.

At LHC, J/ψ photoproduction cross sections have been previously measured by ALICE in pPb collisions at 5.02 TeV, and by LHCb using 7 TeV pp collisions data, reaching $W_{\gamma p}$ energies up to around 700 GeV and 1 TeV, respectively. Recently, LHCb has extended the measurement of J/ψ photoproduction cross section up to $W_{\gamma p}$ energies around 2 TeV analyzing pp collisions at 13 TeV [94]. They report a deviation from a pure power-law

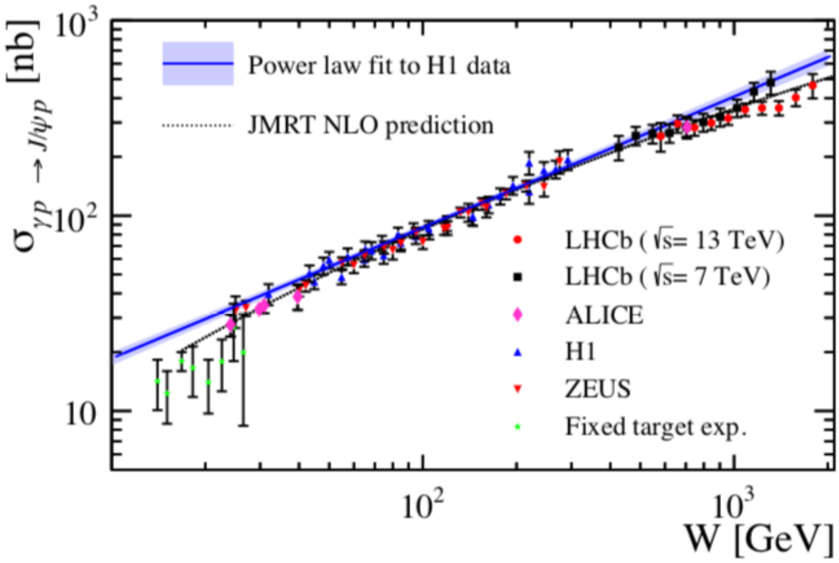

Fig. 6.15 Compilation of photoproduction cross-sections for various experiments, LHCb results are shown.

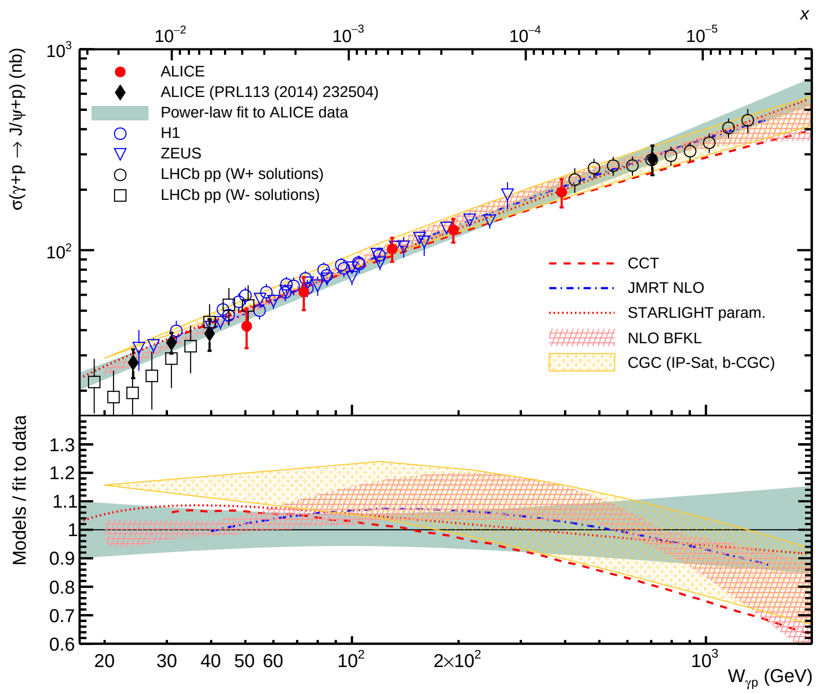

Fig. 6.16 Compilation of photoproduction cross-sections for various experiments, ALICE results are shown.

extrapolation of lower energy data from HERA. However, analyzing data from a symmetric system, LhCb's analysis suffers from the intrinsic possibility of identifying the photon emitter an the target, having then contributions from the low energy and high energy contribution in the their cross sections for a given rapidity bin. To address this issue they fixed the low energy term using the H1 parametrization and subtracted it. In [117], ALICE reported their cross-section measurements corresponding to an energy in the γp centre-of-mass in the interval $40 < \gamma p < 550$ GeV using pPb data at 5.02 TeV, their results are consistent with HERA data. The results reported by LHCb and ALICE are shown in Fig. 6.15, and Fig. 6.16, respectively.

Conclusions

The Λ_b polarization and angular parameters in $\Lambda_b \to J/\psi\Lambda$ decays were measurd using data from pp collisions at $\sqrt{s} = 7$ and 8 TeV collected by the CMS detector at the LHC.

The Λ_b polarization, the parity-violating asymmetry parameter in the Λ_b decay α_1, the Λ longitudinal polarization α_2, and the parameter γ_0 were extracted performing an angular analysis of $\Lambda_b \to J/\psi(\mu^+\mu^-)\Lambda(p\pi)$ decay. The measured values are:

$$
\begin{aligned}
P &= 0.00 \pm 0.06\,(\text{stat}) \pm 0.06\,(\text{syst}),\\
\alpha_1 &= 0.14 \pm 0.14\,(\text{stat}) \pm 0.10\,(\text{syst}),\\
\alpha_2 &= -1.11 \pm 0.04\,(\text{stat}) \pm 0.05\,(\text{syst}),\\
\gamma_0 &= -0.27 \pm 0.08\,(\text{stat}) \pm 0.11\,(\text{syst}).
\end{aligned}
$$

The measured Λ_b polarization is consistent with the LHCb measurement [49] and with theoretical predictions of 0.10 [2] and 0.20 [3]. The presented measurement of α_1 is also consistent with the measurements LHCb [49] and ATLAS [108] measurements, and with no parity violation at the level of one standard deviation. The outcome of this analysis was published in Physical Review D [118]. The measurements can be improved by analyzing the new data collected by CMS from pp collisions at $\sqrt{s} = 13$ TeV during LCH Run2 reducing the statistical uncertainties. The inclusion of the new data will also allow us to perform the full 5D and angular analysis and to extract all 20 parameters describing $\Lambda_b \to J/\psi(\mu^+\mu^-)\Lambda(p\pi)$ decay.

In this thesis, a preliminary measurement of the J/ψ photoproduction cross-section in ultra-peripheral pPb collisions at $\sqrt{s_{NN}}$ = 8.16 TeV was also presented. By measuring this process the gluon density of the proton can be probed at small-x values where the effects of gluon saturation might be visible. Our preliminary results are compatible with extrapolations from a pure power law fit to lower energy data at the level of 2σ.

The most recent LHCb results on the Central exclusive J/ψ production in pp collisions at $\sqrt{s} = 13$ TeV, report a deviation of the photoproduction cross section from a pure power-law extrapolation of lower energy data from HERA. However, results reported by ALICE using data from pPb collisions at 5.02 TeV are found to be compatible with previous HERA measurements. It is important then to have more data and CMS measurement will be providing new information on the J/ψ photoproduction cross section at $W_{\gamma p}$ energies lying in between the ranges already explored by ALICE and LHCb.

Appendix A

Monte Carlo simulation for $\Lambda_b$decays

Simulated events of the signal decay $\Lambda_b \to J/\psi\,\Lambda$ are used to study the effects of detector acceptance and selection on the reconstructed angular distributions. The events are generated using PYTHIA 6.4 [119] for production and hadronization, and EVTGEN [120] is used to describe the b and c hadron decays. The generated events are passed through the full CMS detector simulation based on GEANT4 [121]. The simulated event samples are generated to reproduce $\sqrt{s} = 7$ and 8 TeV data-taking conditions, where additional simulation of pp interactions in the same or nearby beam crossings and the impact of the HLT are included.

The MC events are reconstructed with the same algorithms and requirements as used in data, and the offline selection requirements imposed in data are applied to the MC, as well. The number of signal events and the simulation samples are shown in Table A.1. The invariant mass distributions are shown in Figure A.1. PYTHIA simulates pp collisions. The

Table A.1 Official Monte-Carlo samples used in this analysis. The events were obtained using a double-Gaussian function with the same mean.

Sample	Λ_b (events)	$\overline{\Lambda}_b$(events)
/LambdaBToJPsiLambda_lambdaFilter_7TeV-pythia6evtgen/Summer11LegDR-PU_S13_START53_LV6-v1/AODSIM	15706	14161
/LambdaBToJPsiLambda_lambdaFilter_8TeV-pythia6-evtgen/Summer12DR53X-PU_RD2_START53_V19F-v2/GEN-SIM-RECO	11599	10278

aim of the generator is to provide as accurate as possible a description of what happens in a hadron collision. The software contains theoretical models for a number of physics aspects, such as hard and soft interactions, parton distributions, initial and final state parton showers, multiple interactions, fragmentation and decays.

EVTGEN implements specialized models according to the properties of the hadron, such as models for semileptonic decays, CP-violating decays and spin correlations. For the

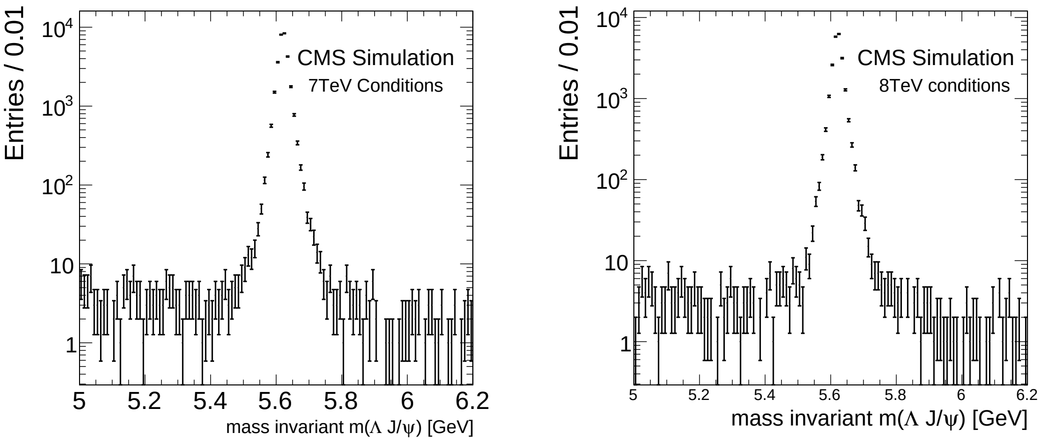

Fig. A.1 Invariant mass distribution of Λ_b candidates in the 7 (left) and 8 TeV (right) MC samples. The plots show a few combinatorial background events remaining after final selection requirements.

$\Lambda_b \to J/\psi\,\Lambda$ and $J/\psi \to \mu^+\mu^-$ we use a phase space decay model, and in particular for $J/\psi \to \mu^+\mu^-$ decays the decay is combined with a routine that allows QED photon radiative corrections for muons (see Ref. [120]). Since Λ is a long lived particle that decay far away the PV, it can not forced to decay to a specific channel.

PYTHIA and EVTGEN work as an input to the full detector simulation as signal collisions and decays. The CMS simulation [112] is based on GEANT4 [121], which provides a rich set of physics process describing electromagnetic and hadronic interactions. Also provides tools for modeling the full CMS detector geometry and interfaces to retrieve information from particle tracking through those detectors and magnetic field. The simulation is implemented in all CMS detectors in both the central and forwards regions, including the field map from the solenoid. The program implements the sensitive detector behavior, track selection mechanism hit collection and digitization. The effect of the L1 and HLT triggers are implemented as in data by L1 seeds and HLT menus. The pile-up effect is simulated separately from the signal collisions by producing simulated hits and then merging the events randomly to the signal events.

Bibliography

[1] W. G. D. Dharmaratna and Gary R. Goldstein. Single quark polarization in quantum chromodynamics subprocesses. *Phys. Rev. D*, 53:1073–1086, Feb 1996.

[2] G. Hiller, M. Knecht, F. Legger, and T. Schietinger. Photon polarization from helicity suppression in radiative decays of polarized Λ_b to spin-3/2 baryons. *Phys. Lett. B*, 649:152, 2007.

[3] Z.J. Ajaltouni, E. Conte, and O. Leitner. Λ_b decays into Λ-vector. *Physics Letters B*, 614(3):165 – 173, 2005.

[4] L.V. Gribov, E.M. Levin, and M.G. Ryskin. Semihard processes in QCD. *Physics Reports*, 100(1):1 – 150, 1983.

[5] A.H. Mueller. Small-x behavior and parton saturation: A QCD model. *Nuclear Physics B*, 335(1):115 – 137, 1990.

[6] Lyndon Evans and Philip Bryant. LHC Machine. *JINST*, 3(08):S08001, 2008.

[7] S. et al. Chatrchyan. The CMS Experiment at the CERN LHC. *JINST*, 3:S08004, 2008.

[8] G. Aad et al. The ATLAS Experiment at the CERN Large Hadron Collider. *JINST*, 3:S08003, 2008.

[9] The ALICE Collaboration. The ALICE experiment at the CERN LHC. *JINST*, 3(08):S08002, 2008.

[10] The LHCb Collaboration . The LHCb Detector at the LHC. *JINST*, 3(08):S08005, 2008.

[11] S. Chatrchyan et al. The CMS experiment at the CERN LHC. *JINST*, 3:S08004, 2008.

[12] G. L. Bayatian et al. *CMS Physics: Technical Design Report Volume 1: Detector performance software*. CERN, 2006.

[13] M Pimi. *Compact Muon Solenoid*. HU-SEFT-1990-03. HU-SEFT-90-03. CERN, 1990.

[14] CMS Collaboration. *The CMS magnet project: Technical Design Report*. Technical Design Report CMS. CERN, Geneva, 1997.

[15] The CMS Collaboration. Description and performance of track and primary-vertex reconstruction with the cms tracker. *JINST*, 9(10):P10009, 2014.

[16] CMS Collaboration. *The CMS electromagnetic calorimeter project: Technical Design Report*. Technical Design Report CMS. CERN, Geneva, 1997.

[17] CMS Collaboration. *The CMS muon project: Technical Design Report*. Technical Design Report CMS. CERN, Geneva, 1997.

[18] Vardan Khachatryan et al. The CMS trigger system. *JINST*, 12:P01020, 2017.

[19] CMS Collaboration. *CMS The TriDAS Project: Technical Design Report, Volume 2: Data Acquisition and High-Level Trigger. CMS trigger and data-acquisition project*. Technical Design Report CMS. CERN, Geneva, 2002.

[20] CMS Collaboration. *CMS. The TriDAS project. Technical design report, vol. 1: The trigger systems*. CERN, 2000.

[21] M Jeitler et al. The Level-1 global trigger for the CMS experiment at LHC. *JINST*, 2(01):P01006, 2007.

[22] Sergio Cittolin, Attila Rácz, and Paris Sphicas. *CMS: The TriDAS project Technical design report, Vol. 2: Data acquisition and high-level trigger*. CERN, 2002.

[23] Christoph et al. Eck. *LHC computing Grid: Technical Design Report*. Technical Design Report LCG. CERN, Geneva, 2005.

[24] M Abbrescia et al. The simulation of resistive plate chambers in avalanche mode: charge spectra and efficiency. *Nucl. Instrum. Meth., A*, 431(3):413 – 427, 1999.

[25] Fridman A. Kennedy L. Kennedy L. Fridman, A. *Plasma Physics and Engineering*. Taylor and Francis group, CRC Press, 2011.

[26] M.C Fouz. The CMS muon system. *Nucl. Instrum. Meth., A*, 446(1):366 – 372, 2000.

[27] M. Abbrescia et al. Effect of the linseed oil treatment on the performance of the resistive plate counters. *CMS-NOTE-1997- 018*, 1997.

[28] Changguo Lu. RPC electrode material study. *Nucl. Instrum. Meth., A*, 602(3):761 – 765, 2009. Proceedings of the 9th International Workshop on Resistive Plate Chambers and Related Detectors.

[29] Abbrescia M. and et. al. Properties of C2H2F4 Based Gas Mixture for Avalanche Mode Operation of Resistive Plate Chambers. Technical Report CMS-NOTE-1997-004, CERN, Geneva, Jan 1997.

[30] P Camarri, R Cardarelli, A.Di Ciaccio, and R Santonico. Streamer suppression with SF6 in RPCs operated in avalanche mode. *Nucl. Instrum. Meth., A*, 414(2):317 – 324, 1998.

[31] G. Apollinari et al. High-Luminosity Large Hadron Collider (HL-LHC), Technical Design Report. Technical Report CERN-2017-007-M, CERN, Geneva, 2017.

[32] G. Apollinari et al. High-Luminosity Large Hadron Collider (HL-LHC): Preliminary Design Report. Technical Report CERN-2015-005, CERN, Geneva, 2015.

[33] M. Abbrescia et al. Study of long-term performance of CMS RPC under irradiation at the CERN GIF. *JINST*, A(533):762–766, 2004.

[34] H. C. Kim et al. Quantitative aging study with intense irradiation tests for the CMS forward RPCs. *Nucl. Instrum. Meth.*, A(602):771, 2009.

[35] D. Pfeiffer et al. The Radiation Field in the Gamma Irradiation Facility (GIF++) at CERN. *Nucl. Instrum. Meth.*, A(866):91, 2017.

[36] CMS Collaboration. Performance of the CMS muon detector and muon reconstruction with proton-proton collisions at $\sqrt{13}$ TeV. *JINST*, 13(06):P06015, 2018.

[37] CMS Collaboration. The Phase-2 Upgrade of the CMS Muon Detectors. Technical Report CERN-LHCC-2017-012, CERN, Geneva, 2017.

[38] S. Constantini et al. Radiation background with the CMS RPCs at the LHC. *JINST*, 10:C05031, 2015.

[39] M. I. Pedraza-Morales et al. First results of CMS RPC performance at 13 TeV. *JINST*, 11:C12002, 2016.

[40] M. Abbrescia et al. Cosmic ray tests of double-gap resistive plate chambers for the CMS experiment. *Nucl. Instrum. Meth. A*, 550:116, 2015.

[41] R. Arnaldi et al. Influence of temperature and humidity on bakelite resistivity. *Nucl. Instrum. Meth. A*, 456:140, 2000.

[42] R.I. Rabadan-Trejo and et al. Long-term performance and longevity studies of the CMS Resistive Plate Chambers. *JINST*, 13(08):P08024, 2018.

[43] Thomas Mannel and Gerhard A. Schuler. Semileptonic decays of bottom baryons at lep. *Phys. Lett. B*, 279:194, 1992.

[44] Adam F. Falk and Michael E. Peskin. Production, decay, and polarization of excited heavy hadrons. *Phys. Rev. D*, 49:3320, 1994.

[45] B. Mele and G. Altarelli. Lepton spectra as a measure of b quark polarization at LEP. *Phys. Lett. B*, 299:345, 1993.

[46] D. et al. Buskulic. Measurement of Λ_b polarization in Z decays. *Phys. Lett. B*, 365:437, 1996.

[47] G. Abbiendi et al. Measurement of the average polarization of b baryons in hadronic Z decays. *Phys. Lett. B*, 444:539, 1998.

[48] P. Abreu et al. Λ_b polarization in Z decays at LEP. *Phys. Lett. B*, 474:205, 2000.

[49] R Aaij et al. Measurements of the $\Lambda_b \to J/\psi\Lambda$ decay amplitudes and the Λ_b polarisation in pp collisions at $\sqrt{s} = 7$ TeV. *Phys. Lett. B*, 724:27, 2013.

[50] T. Aaltonen et al. Evidence for a bottom baryon resonance Λ_b^* in CDF data. *Phys. Rev. D*, 88:071101, 2013.

[51] T. Aaltonen et al. Observation of the heavy baryons Σ_b and Σ_b^*. *Phys. Rev. Lett.*, 99:202001, 2007.

[52] T. Aaltonen et al. Measurement of the masses and widths of the bottom baryons $\Sigma_b^\pm$ and $\Sigma_b^{*\pm}$. *Phys. Rev. D*, 85:092011, 2012.

[53] R Aaij et al. Observation of excited Λ_b baryons. *Phys. Rev. Lett.*, 109:172003, 2012.

[54] Mario Galanti et al. Heavy baryons as polarimeters at colliders. *Journal of High Energy Physics*, 2015(11):67, Nov 2015.

[55] Hai-Yang Cheng. Nonleptonic weak decays of bottom baryons. *Phys. Rev. D*, 56:2799, 1997.

[56] Fayyazuddin and Riazuddin. Two-body nonleptonic Λ_b decays in the quark model with factorization ansatz. *Phys. Rev. D*, 58:014016, 1998.

[57] Rukmani Mohanta, Anjan K. Giri, Mohinder P. Khanna, Muneyuki Ishida, Shin Ishida, and Masuho Oda. Hadronic weak decays of Λ_b baryon in the covariant oscillator quark model. *Prog. Theor. Phys.*, 101:959, 1999.

[58] Hsien-Hung Chou, Chung-Hsien Chouand Shih, Shih-Chang Lee, and Hsiang Li. $\Lambda_b \to \Lambda J/\psi$ decay in perturbative QCD. *Phys. Rev. D*, 65:074030, 2002.

[59] Zheng-Tao Wei, Hong-Wei Ke, and Xue-Qian Li. Evaluating decay rates and asymmetries of Λ_b into light baryons in LFQM. *Phys. Rev. D*, 80:094016, 2009.

[60] Thomas Gutsche, Mikhail A. Ivanov, Jurgen G. Korner, Valery E. Lyubovitskij, and Pietro Santorelli. Polarization effects in the cascade decay $\Lambda_b \to \Lambda(\to p\pi^-) + J/\psi(l^+l^-)$ in the covariant confined quark model. *Phys. Rev. D*, 88:114018, 2013.

[61] V.N. Gribov and L.N. Lipatov. Deep inelastic electron scattering in perturbation theory. *Physics Letters B*, 37(1):78 – 80, 1971.

[62] G. Altarelli and G. Parisi. Asymptotic freedom in parton language. *Nuclear Physics B*, 126(2):298 – 318, 1977.

[63] Yu.L. Dokshitzer. Calculation of structure functions of deep-inelastic scattering and e+e- annihilation by perturbation theory in quantum chromodynamics. *Sov. Phys. JETP*, 46:641, 1977.

[64] Stefano Forte and Graeme Watt. Progress in the determination of the partonic structure of the proton. *Annual Review of Nuclear and Particle Science*, 63(1):291–328, 2013.

[65] Paul R. Newman and Matthew Wing. The hadronic final state at hera. *Rev. Mod. Phys.*, 86:1037–1092, Aug 2014.

[66] H. Abramowicz et al. Combination of measurements of inclusive deep inelastic $e^\pm p$ scattering cross sections and QCD analysis of HERA data. *Eur. Phys. J.*, C75(12):580, 2015.

[67] S. I. Alekhin. Parton distributions from deep-inelastic-scattering data. *Phys. Rev. D*, 68:014002, Jul 2003.

[68] Hung-Liang Lai, Marco Guzzi, Joey Huston, Zhao Li, Pavel M. Nadolsky, Jon Pumplin, and C.-P. Yuan. New parton distributions for collider physics. *Phys. Rev. D*, 82:074024, Oct 2010.

[69] R. D. Ball et al. A Determination of parton distributions with faithful uncertainty estimation. *Nucl. Phys.*, B809:1–63, 2009. [Erratum: Nucl. Phys.B816,293(2009)].

[70] L. A. Harland-Lang, A. D. Martin, P. Motylinski, and R. S. Thorne. Parton distributions in the lhc era: Mmht 2014 pdfs. *The European Physical Journal C*, 75(5):204, May 2015.

[71] M. Glück, P. Jimenez-Delgado, and E. Reya. Dynamical parton distributions of the nucleon and very small-x physics. *The European Physical Journal C*, 53(3):355–366, Feb 2008.

[72] O. Zenaiev, A. Geiser, K. Lipka, J. Blümlein, A. Cooper-Sarkar, M.-V. Garzelli, M. Guzzi, O. Kuprash, S.-O. Moch, P. Nadolsky, R. Placakyte, K. Rabbertz, I. Schienbein, and P. Starovoitov. Impact of heavy-flavour production cross sections measured by the lhcb experiment on parton distribution functions at low x. *The European Physical Journal C*, 75(8):396, Aug 2015.

[73] Rhorry Gauld, Juan Rojo, Luca Rottoli, and Jim Talbert. Charm production in the forward region: constraints on the small-x gluon and backgrounds for neutrino astronomy. *JHEP*, 11:009, 2015.

[74] Matteo Cacciari, Michelangelo L. Mangano, and Paolo Nason. Gluon pdf constraints from the ratio of forward heavy-quark production at the lhc at $\sqrt{s} =$ t and 13 tev. *The European Physical Journal C*, 75(12):610, Dec 2015.

[75] S. P. Jones, A. D. Martin, M. G. Ryskin, and T. Teubner. Probes of the small x gluon via exclusive j/ψ and υ production at hera and the lhc. *Journal of High Energy Physics*, 2013(11):85, Nov 2013.

[76] V. P. Gonçalves, L. A. S. Martins, and W. K. Sauter. Probing the gluon density of the proton in the exclusive photoproduction of vector mesons at the lhc: a phenomenological analysis. *The European Physical Journal C*, 76(2):97, Feb 2016.

[77] C. Adler and et al. Coherent ρ^0 production in ultraperipheral heavy-ion collisions. *Phys. Rev. Lett.*, 89:272302, Dec 2002.

[78] S. Afanasiev and et al. Photoproduction of J/ψ and of high mass e^+e^- in ultra-peripheral Au+Au collisions at $\sqrt{s_{NN} =}$ 200-GeV. *Phys. Lett.*, B679:321–329, 2009.

[79] T. Aaltonen and et. al. Observation of exclusive charmonium production and $\gamma\gamma \to \mu^+\mu^-$ in $p\overline{p}$ collisions at $\sqrt{s} = 1.96$ TeV. *Phys. Rev. Lett.*, 102:242001, Jun 2009.

[80] Betty Abelev and et al. Coherent J/ψ photoproduction in ultra-peripheral Pb-Pb collisions at $\sqrt{s_{NN}} = 2.76$ TeV. *Phys. Lett.*, B718:1273–1283, 2013.

[81] B. Abelev and et.al. Adam. Exclusive j/ψ photoproduction off protons in ultraperipheral p-pb collisions at $\sqrt{s_{\rm NN}} = 5.02$ TeV. *Phys. Rev. Lett.*, 113:232504, Dec 2014.

[82] B. Abbas and et al. Charmonium and e^+e^- pair photoproduction at mid-rapidity in ultra-peripheral pb-pb collisions at $\sqrt{s_{NN}} = 2.76$ tev. *The European Physical Journal C*, 73(11):2617, Nov 2013.

[83] R Aaij and et al. Exclusive j/ψ and $\psi(2s)$ production in pp collisions at $\sqrt{s} = 7$ tev. *Journal of Physics G: Nuclear and Particle Physics*, 40(4):045001, 2013.

[84] R Aaij and et al. Updated measurements of exclusive Jψ and $\psi(2S)$ production cross-sections in pp collisions at $\sqrt{s} = 7$ TeV. *Journal of Physics G: Nuclear and Particle Physics*, 41(5):055002, 2014.

[85] Roel Aaij et al. Measurement of the exclusive Υ production cross-section in pp collisions at $\sqrt{s} = 7$ TeV and 8 TeV. *JHEP*, 09:084, 2015.

[86] The CMS collaboration and S. et al. Chatrchyan. Exclusive $\gamma\gamma \to \mu^+\mu*-$ production in proton-proton collisions at $\sqrt{s} = 7$ tev. *Journal of High Energy Physics*, 2012(1):52, Jan 2012.

[87] The CMS collaboration and S. et others Chatrchyan. Search for exclusive or semi-exclusive $\gamma\gamma$ production and observation of exclusive and semi-exclusive e^+e^- production in pp collisions at $\sqrt{s} = 7$ tev. *Journal of High Energy Physics*, 2012(11):80, Nov 2012.

[88] S. et al. Chatrchyan. Study of exclusive two-photon production of W^+W^- in pp collisions at 7 $\sqrt{s} = 7$ TeV and constraints on anomalous quartic gauge couplings. *Journal of High Energy Physics*, 2013(7):116, Jul 2013.

[89] E. Fermi. Über die theorie des stoßes zwischen atomen und elektrisch geladenen teilchen. *Zeitschrift für Physik*, 29(1):315–327, Dec 1924.

[90] C. F. v. Weizsäcker. Ausstrahlung bei stößen sehr schneller elektronen. *Zeitschrift für Physik*, 88(9):612–625, Sep 1934.

[91] E. J. Williams. Nature of the high energy particles of penetrating radiation and status of ionization and radiation formulae. *Phys. Rev.*, 45:729–730, May 1934.

[92] A. Braman, E. Etim, and M. Greco. A vector meson dominance approach to scale invariance. *Phys. Lett B*, 41(5):609 – 612, 1972.

[93] M. Greco. Deep-inelastic processes. *Nucl. Phys. B*, 63:398 – 412, 1973.

[94] Aaij R and et. al. Central exclusive production of J/ψ and ψ(2S) mesons in pp collisions at $\sqrt{s} = 13$ tev, 2018.

[95] M. Jacob and G.C. Wick. On the general theory of collisions for particles with spin. *Annals of Physics*, 7(4):404 – 428, 1959.

[96] J. D. Richman. An experimenter's guide to the helicity formalism. Technical report, Calif. Inst. Technol., Jun 1984.

[97] R. Aaij et al. Observation of $J\psi$ resonances consistent with pentaquark states in $\Lambda_b \to J/\psi Kp$ decays. *Phys. Rev. Lett.*, 115:072001, 2015.

[98] M. Kramer and H. Simma. Angular correlations in $\Lambda_b \to \Lambda + V$: Polarization measurements, HQET and CP violation. *Nucl. Phys. Proc. Suppl.*, 50:125, 1996.

[99] Particle Data Group, C. Patrignani, et al. Review of particle physics. *Chin. Phys. C*, 40:100001, 2016.

[100] CMS Collaboration. CMS B-Physics and Quarkonia results. https://twiki.cern.ch/twiki/bin/view/CMSPublic/PhysicsResultsBP, 07 2011.

[101] Vardan Khachatryan et al. Strange particle production in pp collisions at $\sqrt{s} = 0.9$ and 7 TeV. *JHEP*, 05:064, 2011.

[102] Claus Grupen and Boris Schwartz. *Particle detectors*. Cambridge, UK: Cambridge Univ. Pr. (2008) 651 p, 2008.

[103] V. Khachatryan, A. M Sirunyan, et al. CMS tracking performance results from early LHC operation. *Eur. Phys. J. C*, 70:1165, 2010.

[104] S. Chatrchyan and et. al. Measurement of the Λ_b cross section and the Λ_b to $\overline{\Lambda}_b$ ratio with $J/\psi\Lambda$ decays in pp collisions at $\sqrt{s} = 7$ TeV. *Physics Letters B*, 714(2):136 – 157, 2012.

[105] Roger Barlow. Extended maximum likelihood. *Nucl. Instrum. Meth. A*, 297(3):496 – 506, 1990.

[106] Wouter Verkerke and David P. Kirkby. The RooFit toolkit for data modeling. *eConf*, C0303241:MOLT007, 2003.

[107] O. Leitner, Z.J. Ajaltouni, and E. Conte. An angular distribution analysis of Λ_b decays. *Nucl. Phys. A*, 755:435, 2005.

[108] Aad G. et al. Measurement of the parity-violating asymmetry parameter α_b and the helicity amplitudes for the decay $\Lambda_b \to J/\psi\Lambda$ with the ATLAS detector. *Phys. Rev. D*, 89:092009, 2014.

[109] CMS Muon Id Guide. https://twiki.cern.ch/twiki/bin/view/CMSPublic/SWGuideMuonId.

[110] Starlight. https://starlight.hepforge.org.

[111] Spencer R. Klein, Joakim Nystrand, Janet Seger, Yuri Gorbunov, and Joey Butterworth. Starlight: A monte carlo simulation program for ultra-peripheral collisions of relativistic ions. *Computer Physics Communications*, 212:258 – 268, 2017.

[112] Banerjee S. CMS simulation software. *Journal of Physics: Conference Series*, 396(2):022003, 2012.

[113] M. Tanabashi and et. al. Review of particle physics. *Phys. Rev. D*, 98:030001, Aug 2018.

[114] The H1 Collaboration. Elastic and proton-dissociative photoproduction of J/ψ mesons at HERA. *The European Physical Journal C*, 73(6):2466, Jun 2013.

[115] The CMS collaboration. Performance of cms muon reconstruction in pp collision events at $\sqrt{s} = 7$ tev. *JINST*, 7(10):P10002, 2012.

[116] CMS Collaboration. CMS luminosity measurement using 2016 proton-nucleus collisions at nucleon-nucleon center-of-mass energy of 8.16 TeV. *CMS-PAS-LUM-17-002*, 2018.

[117] Aaij R and et. al. Energy dependence of exclusive J/ψ photoproduction off protons in ultrapheriperal p-Pb collisions at $\sqrt{s_{NN}} =$ 5.02 TeV, 2018.

[118] A. M. Sirunyan and et al. Measurement of the Λ_{b} polarization and angular parameters in $\Lambda_b \to J/\psi\Lambda$ decays from pp collisions at $\sqrt{s} = 7$ and 8 TeV. *Phys. Rev. D*, 97:072010, Apr 2018.

[119] T. Sjöstrand, S. Mrenna and P. Z. Skands. PYTHIA 6.4 physics and manual. *JHEP*, 05:026, 2006.

[120] D. J. Lange. The EVTGEN particle decay simulation package. *Nucl. Instrum. Meth. A*, 462:152, 2001.

[121] Agostinellia S. et al. GEANT4: a simulation toolkit. *Nucl. Instrum. Meth. A*, 506:250, 2003.